Biophysical models for bacterial FtsZ filaments

Memoria presentada para optar al Grado de Doctor en Ciencias Físicas por

Ines Hörger

Director

Pedro Tarazona Lafarga

Departamento de Física Teórica de la Materia Condensada
Universidad Autónoma de Madrid

Octubre de 2010

Acknowledgements

I am grateful to all of my colleagues, collaborators and friends who have accompanied me during the time period of this Thesis. Especially I want to thank my supervisor Pedro Tarazona.

Resumen

El descubrimiento del citoesqueleto bacteriano es relativamente reciente, se produjo hace aproximadamente 20 años. La proteína MreB, encargada de estabilizar la forma del citoesqueleto, y la proteína FtsZ, relacionada con el proceso de división, son los dos constituyentes principales del citoesqueleto. FtsZ, frecuentemente descrita como la antecesora de la tubulina, juega un papel crucial en el proceso de división de las células procariotas. Presente en todas las células bacterianas, la proteina FtsZ se polimeriza y une al interior de la membrana bacteriana. Una vez en la membrana y como paso previo a la división celular la proteína forma un anillo constrictor, conocido como anillo septal o anillo-Z, que es el encargado de iniciar el proceso de invaginación de la membrana.

La polimerización de FtsZ requiere del nucleótido GTP que sirve como "pegamento" entre dos monómeros. Seguidamente se suele hidrolizar en GDP para a continuación intercambiarse con otro nucleótido GTP de forma que el enlace entre monómeros de FtsZ se mantenga estable. Este proceso junto con el intercambio entre dos monómeros de FtsZ (algo bastante frecuente) contribuye a la naturaleza dinámica de los polímeros de FtsZ dando como resultado una gran variedad de estructuras que dependen de las condiciones físico-químicas del entorno. Filamentos simples o dobles, rectos o curvados, anillos, espirales y estructuras de tipo lazo han sido observadas *in vitro* mediante imágenes de microscospía electrónica (EM). En los últimos años el estudio de filamentos de FtsZ adsorbidos en superficies sólidas mediante técnicas de microscopía de fuerzas atómicas (AFM) ha abierto una nueva y potente línea de investigación experimental. Las estructuras formadas por la proteína pueden ahora ser observadas bajo condiciones de equilibrio dinámico, algo que no era posible usando EM. Además nuevos experimentos en sistemas biosintetizados han demostrado los efectos constrictores de FtsZ en liposomas artificiales.

Inmerso en este escenario de información experimental que evoluciona rápidamente este trabajo de Tesis se ha centrado en el desarrollo de modelos teóricos que han sido directamente contrastados con información experimental. Hemos estudiado los dos procesos complementarios que tienen lugar en el proceso de constricción. Por un lado los filamentos de FtsZ junto con el mecanismo que produce el anillo-Z y la consiguiente generación de una fuerza constrictiva. Por otro lado se ha analizado la reacción de la membrana bacteriana a la aplicación de dicha fuerza.

En la primera parte de la Tesis los filamentos de FtsZ se han modelado como cuentas en una cadena que interaccionan unas con otras. Basándonos en el análisis de una serie de imágenes de AFM hemos podido modelar el filamento con el mínimo número de interacciones entre monómeros que se necesitan para reproducir de forma satisfactoria las tendencias encontradas en los experimentos: enlaces fuertes entre proteínas adyacentes, una curvatura de enlace espontánea, cierta flexibilidad del filamento y, aparentemente, una atracción lateral entre cadenas. Los parámetros del modelo han sido determinados analizando resultados experimentales obtenidos bajo diferentes condiciones como por ejemplo cambios en la concentración de proteínas, el valor del

pH o el tipo de nucleótido encargado del enlace entre diferentes monómeros. Hemos conseguido reproducir las diferentes estructuras que forman los filamentos de FtsZ mediante simulaciones de dinámica de Langevin y hemos explorado la forma y dinámica de los filamentos sobre la superficie de un cilindro (modelo útil para reproducir la forma de las bacterias). También hemos estimado la magnitud de la fuerza radial constrictiva generada por un anillo-Z que optimiza los contactos laterales.

En la segunda parte de la Tesis hemos estudiado la deformación de una membrana como consecuencia de la fuerza constrictiva mencionada anteriormente. La pared de una célula bacteriana está constituida por diferentes capas cuyo rol en la división celular no está todavía completamente esclarecido. Nuestro análisis se ha limitado a la parte interna de la membrana celular bacteriana, donde se une el anillo-Z y comienza la invaginación. Hemos minimizado el Hamiltoniano de Helfrich para membranas líquidas en geometría cilíndrica junto con un anillo de fuerza perpendicular al eje del cilindro bajo diferentes condiciones de contorno. Hemos comenzado el estudio con la deformación de un liposoma tubular libre, donde ha sido posible la comparación con experimentos recientes realizados *in vitro*. También se ha analizado cuáles son los efectos de la diferencia entre las presiones osmóticas en el interior y el exterior de la célula así como la ligadura impuesta por una pared bacteriana rígida.

Summary

The discovery of a bacterial cytoskeleton only dates around 20 years ago. The best-known representatives are the shape stabilizing protein MreB and the division protein FtsZ. FtsZ, often described as tubulin ancestor, plays a crucial role in the procaryotic cell division process. Being present in all bacterial cells, the protein polymerizes and attaches to the inner bacterial membrane at mid-cell. There it forms, prior to cell division, the so called septal or Z-ring that initiates the invagination of the membrane.

Polymerization of FtsZ requires the nucleotide GTP that serves as a "glue" between two monomers and is almost immediately hydrolyzed to GDP followed by GDP-GTP exchange in order to maintain the bond. Together with a frequent subunit turnover this contributes to the dynamic nature of FtsZ polymers that are able to adopt a great variety of structures depending on the environmental conditions. *In vitro*, single and double-stranded, straight and curved filaments, rings, spirals and ribbon-like higher structures have been observed in electron microscopy (EM) images. In the last few years the application of Atomic Force Microscopy (AFM) techniques to FtsZ filaments adsorbed on solid surfaces has opened a new and powerful line of experimental advance. The structures formed by the protein may be observed under dynamical equilibrium conditions, rather than in the frozen EM images. Also, new experiments in bio-synthetic systems have proved the effects of FtsZ anchored on artificial liposomes.

In this rapidly evolving scenario of experimental information, the work of this PhD Thesis has being focused to the development of theoretical models, directly contrastable with the experimental information. We have modeled the two complementary parts of this constriction process, the filaments formed by FtsZ and the mechanisms that lead to the formation of the Z-ring and the generation of a constriction force on the one hand and the reaction of the bacterial membrane upon the application of a radial force on the other hand. In the first part of the thesis, we modeled the FtsZ filaments as beads in chain interacting with each other. Based on a series of AFM images of FtsZ filaments on mica, we introduced a minimum number of monomer-monomer interactions with associated parameters that account for the most obvious experimental tendencies: strong bonds between adjacent proteins, a spontaneous bond curvature, a certain filament flexibility and an apparent lateral attraction between chains. We determined the model parameters analyzing AFM images of FtsZ filaments formed under different experimental conditions like protein concentration, pH value and type of nucleotide. We reproduced the observed shapes in Langevin dynamics simulations and explored shape and dynamics of the filaments in the bacterial cylindrical geometry. We estimated the radial constriction force generated by a Z-ring that optimizes its lateral contacts.

In the second part of this thesis, we studied the deformation of a membrane caused by this radial constriction force. The bacterial cell wall is constituted by several layers and their role along the division process is complicated and not yet clear. Our analysis was limited to the inner

bacterial cell membrane where the Z-ring attaches and initiates the invagination. We minimized the Helfrich Hamiltonian for liquid membranes in cylindrical geometry together with a force ring perpendicular to the cylindrical axis applying different boundary conditions. We started with the deformation of a free tubular liposome where we could compare our results to recent *in vitro* experiments. We calculated the shape of the deformation and the required force. We further explored the effects of the osmotic pressure difference between the bacterial interior and the surrounding medium and the deformation constraint imposed by the rigid bacterial cell wall.

Contents

1. Introduction

During my PhD time, I was often asked about my work. My typical answer on questions like 'What are you working on', raised by my family and friends has been: 'We work on bacterial cell division, mainly on a protein, that builds filaments and constricts the membrane during the division process.' The typical reaction was then: 'That rather sounds like biology.' Indeed we have been working with biologists and our analysis was based on their experimental results. Our contribution as physicists was the interpretation of the experimental data in terms of a theoretical model of the interactions between the individual building blocks (monomers of the protein FtsZ) of the filaments that lead to the formation of the observable variety of shapes. In computer simulations we could adjust the model so that the filaments behaved like in the experiments and then we could change the 'experimental conditions' and simulate experimentally not (yet) accessible scenarios. In that way a direct interplay between experiment and theoretical analysis could be established. What is our work good for? The clearest answer to this question is that the detailed understanding of the mechanism of bacterial cell division is essential for its frustration. In the best case one day new antibiotics can be designed and our work might have contributed in a certain way. Altogether, I am in the fortunate situation that I have been working in a fascinating field at the frontier between physics and biology, following concrete (although not immediate) intentions.

In the introduction, I will give an overview of what I will present in the subsequent chapters and I will start with some general ideas about the work that we have done. In the last decades, two fields of science, at first sight opposite in the treated issues have been approaching each other. On the one hand, biology, describing the living world, on the other hand physics, traditionally the science of the non-living world. Observation techniques have allowed deeper insights into living matter since their discovery, beginning with the light microscopy in the early 17th century. The resolution of a light microscope does not go beyond typical cell sizes and the limit of theoretical physics is reached at a much lower level, the interaction of two atoms - a huge gap had to be overcome. Of course, imaging techniques have made much progress and today the atomic structures of a big number of the biomolecules found inside the cells are known. These structures have been determined by the use of electron microscopy of isolated molecules and they are used in molecular dynamics simulations of cell processes like for example the transport of water or small molecules through aquaporins, specific membrane channels. These simulations are done at atomic level, using force fields, empirical potentials that describe pair interactions between atoms. With this technique, the interplay of a reduced number of biomolecules can be simulated. Actually biological systems are much more complex. One biological macromolecule consists of hundreds or thousands of atoms and many of them give rise to higher structures like molecular machines or filaments. All atom simulations for these complex systems are very complicated

or even impossible due to computational limits. At this point, one solution is 'coarse graining'. In order to determine the tertiary structure of a protein (its typical conformation in cellular environment) or the quaternary structure of a protein complex, all atoms have to be taken into account. If we are further interested in how these proteins interact with other proteins (of same or different type) the details of their internal structure become less important and global properties come to the fore. These include the shape (globular, cylindrical, oblate, ...), the total charge or the polarizability. In that way, we can build up a model system, and consider each protein as one monomer that interacts with its neighbours in a certain manner. Therefore, we can use the known size and shape of the specific protein, but how do we have to choose the interactions between monomer pairs? At this point, additional experimental information is essential. Typically this information has some of the following characteristics:

- many 'stationary snapshots' of the interplay between monomers
- low resolution, maybe single monomers cannot be identified
- different behaviour on different experimental conditions

The first point calls for using the tools of statistical physics. A high enough number of samples allows for the calculation of averages and typical behaviours. The second point raises the question of how we can determine interactions between particles, that cannot even be identified. Here, we have to ask for the kind of interactions between monomers, that lead to the global, observable structures. For filament forming monomers this might be the appearance of a non-vanishing global (mean) curvature due to a preferential bond angle between individual proteins. Finally, different experimental conditions may give insight into the different types and strengths of these interactions which should all fit within the established model. Once, the types of interactions and its parameters have been determined, the model can be used to explore scenarios, which are not directly observable in experiments like specific geometries or *in vivo* comportments. We can also make testable predictions that inspire new experimental setups which can be used to check the validity of the model. Membranes are another example of structures that consist of many individual building blocks, the main part of them phospholipids. The lipids self-assemble to form bilayers which in turn appear as flat sheets or liposomes enclosing a volume. The mechanical properties of these bilayers can often be described by treating them as continuous, elastic surfaces.

We have studied essentially two aspects of the bacterial cell division process:

1. **FtsZ protein filaments**
   FtsZ is the major cytoskeletal protein in bacterial cytokinesis. We have developed a model of the filaments formed by FtsZ. By means of analytical calculations and simulations we have applied this model for the analysis of different experimental data sets and we have made predictions of the behaviour of these filaments in environments of difficult experimental accessibility. The study of FtsZ filaments was motivated by experimental results, atomic force microscopy (AFM) images of FtsZ polymers formed under a variety of experimental conditions along the time period of this thesis. In the first part of this work, we will give

an overview of experimental data of FtsZ polymers in general and the AFM images in particular. Then we go on by introducing the chain model that we have used to describe the filaments in 2D and by explaining how, we have used the experimental data to estimate the type and strength of the interactions between monomers, among others by means of Langevin dynamics simulations. We will then present the extrapolation of the model to cylindrical geometry, the analysis of the different shapes and the estimation of the radial force produced by a filament ring. We will return to two dimensional AFM videos of ring conformations. Here we estimated the relation between the chain rigidity and different experimental conditions, we calibrated the time scale in the simulations and we studied the formation of ring and loop configurations. Finally, we will present the last analysis based on the most recent experimental study of short individual filaments absorbed on mica, where we introduced a possible effect of the interaction between the protein and the substrate. We will present this first part of the thesis in an (almost) chronological way, trying to transmit the refinement in both, experimental data and theoretical analysis along the evolution of the work as well as the caution we should act with as we try to quantify and interpret the experiments.

2. **Membrane deformation**
   In order to understand the mechanism of bacterial cell division, we have to understand its two complementary parts. In the first part, we address the question of the generation of force that is necessary to constrict the cell membrane. The second part is dedicated to the answer of the membrane on the application of this force. We will start by introducing the model that we used for the description of the inner bacterial membrane. We expressed its free energy in terms of the Helfrich Hamiltonian for liquid membranes and minimized the free energy of the system composed of the membrane and a force ring. The result is an equation for the membrane shape that we have solved for different boundary conditions. For the case of a free tubular liposome we compared our results to a recent experimental study and we have set in context the required force for the deformation and the estimate of the force produced by the FtsZ-ring. We finally studied the peculiarities of the deformation of the inner bacterial cell wall.

We will now start by giving a short overview of the general topic of this work, the mechanism of bacterial cell division.

2. The mechanism of bacterial cell division

In bacteria, cell division occurs as a binary fission. It begins with DNA replication, continues by cell elongation and ends up in the separation of the original cell into two, usually equally sized, daughter cells. Here, we are interested in this last step, the final partition. The crucial role in this process plays the bacterial cytoskeleton.

2.1. The prokaryotic cytoskeleton

The major components of the eukaryotic cytoskeleton, actin and tubulin, are not found in bacteria and until very recently, 'people more or less thought the bacterial cell was a swimming pool ...' ([1]) or in other words, that prokaryotes lacked a cytoskeleton. Since the 1990s this idea has been completely reversed as more and more evidence was found for that the origin of the cytoskeleton lies in bacteria. The filamenting temperature-sensitive mutant Z (FtsZ) protein and MreB (Fig. (2.1)) have been identified as homologues of actin and tubulin, although their roles in the cell cycle are different.

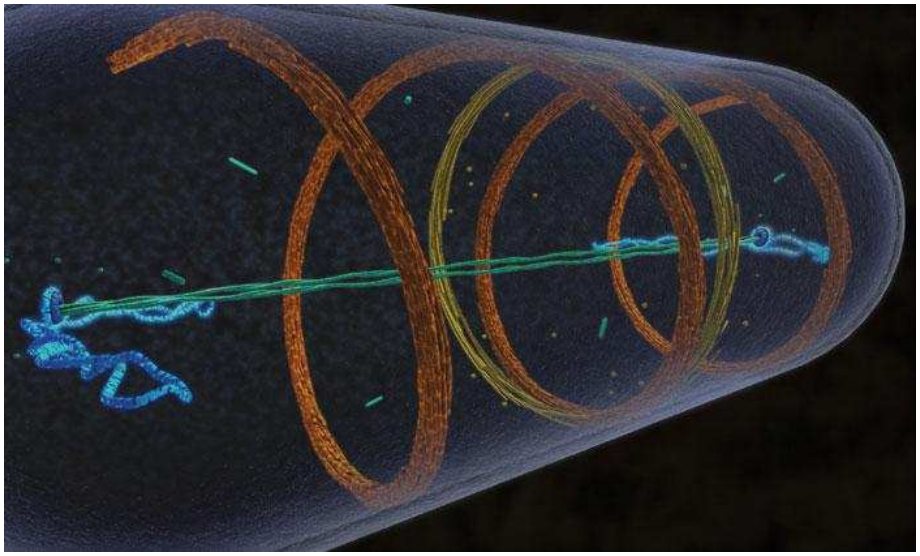

Figure 2.1.: Internal structures in bacteria: MreB (orange) and FtsZ (yellow) [1]

For a long time, this affinity had not been clear as tubulin and FtsZ share low sequence identity at the amino-acid level. Evidence came up in 1998, when the crystal structure of FtsZ was solved [2] and found to be similar to that of eukaryotic tubulin. The same is true for the three dimensional

structures of MreB and actin. In rod shaped bacteria, MreB helically winds around the cell and guaranties its elongation during growth. Actually, without MreB the shell grows spherically [1]. On the other hand, FtsZ is crucial for the partition of the cell. It assembles into a ring, called the Z-ring, attached to the inner cell membrane at the site of division and initiates the invagination of the membrane. In the present picture, FtsZ is thought to have two functions: The Z-ring produces at least part of the constriction force on the cell membrane and it serves as a scaffold to localize wall remodeling enzymes. [3].

2.2. Different stages of the cell cycle

We will continue with a short overview of the different stages of the cell cycle of rod-shaped bacteria, focusing on the role of FtsZ. Fig. (2.2) is a schematic representation of the different steps illustrating first of all how FtsZ acts throughout the division process.

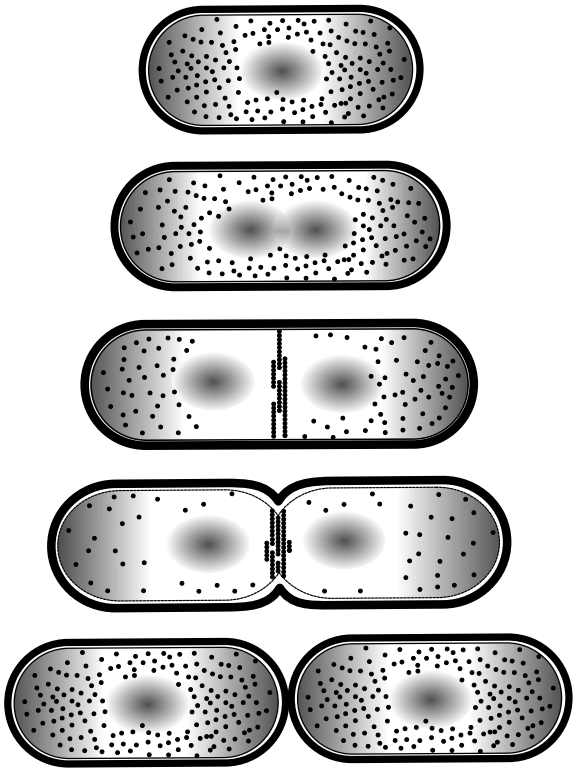

Figure 2.2.: Schematic illustration of the bacterial cell division process. FtsZ monomers are represented as black points.

The concentration of FtsZ monomers in a bacterial cell remains almost constant along the cell cycle and its measured number is found to lie between 3000 and 20000 monomers per cell [4]. The intracellular concentration of FtsZ (3-10 μM) greatly exceeds that of the critical concentration for assembly (0.5-1 μM) [5]. In a simplified picture, there are two mechanisms that inhibit the polymerization of FtsZ in a newborn cell. The Min system acts to prevent Z-ring assembly at

the cell poles and nucleoid occlusion prevents polymerization close to the nucleoid. In Fig. (2.2) these regions are drawn in grey. The first step in a newborn cell is the duplication of its DNA while the FtsZ monomers remain unpolymerized. This is followed by the separation of the two DNA strands and the elongation of the cell. In the center of the cell arises an inhibitor free zone where the FtsZ monomers start to assemble into the Z-ring. In the present picture, this Z-ring is constructed from short protofilaments with an average length of about 30 subunits (125 nm) [3]. FtsZ polymers do not directly attach to the membrane. In E. Coli, its anchoring is mediated by two proteins, FtsA and ZipA [5]. Now, the invagination of the inner cell membrane is initiated at the site of the Z-ring which is supposed to produce (at least part of) the necessary constriction force. The mechanism of this force generation is not yet clear even though recently several models have been proposed. These fall into two categories that we will summarize below. To complete the cell cycle, the mother cell now splits up into two daughter cells and the Z-ring depolymerizes. We have come back to the point of departure and the next round of the cell cycle can be initiated. Before coming to the force generating mechanism, we will briefly describe the bacterial envelope.

2.3. The bacterial envelope

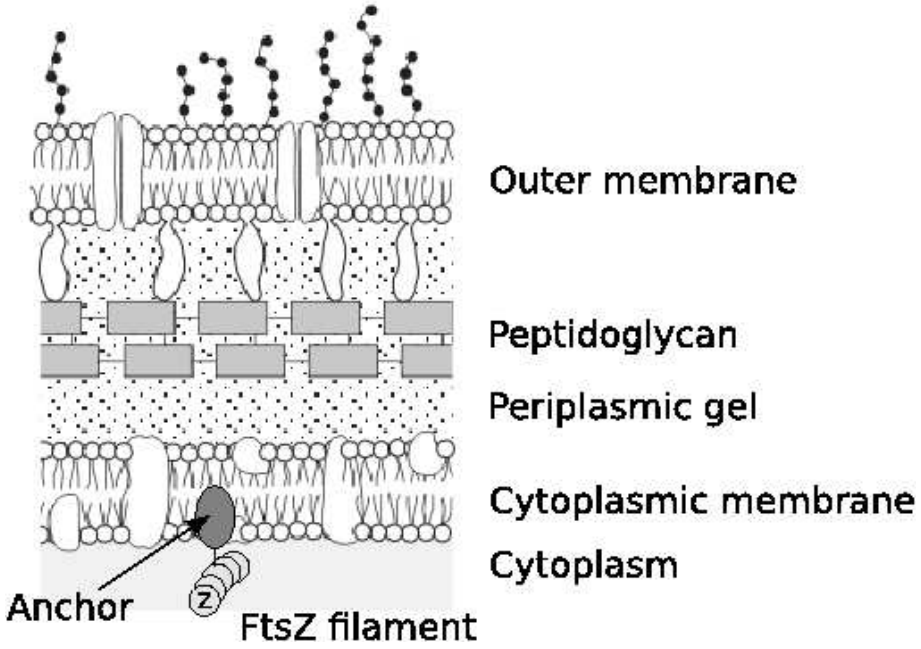

Figure 2.3.: Schematic view of the bacterial envelope of gram-negative bacteria. An FtsZ filament is anchored to the cytoplasmic membrane.

Bacterial envelopes can be divided in two classes. In both cases the cytoplasmic membrane is surrounded by a periplasmic gel and a peptidoglycan network. In the case of gram-negative bacteria this layer is very thin (about 2nm) and surrounded by an outer membrane (Fig. (2.3)). Gram-positive bacteria are surrounded by a thick peptidoglycan network (20-28 nm) and do not

have an outer cell membrane. The most famous and mostly studied bacteria, *Escherichia Coli* (*E. Coli*) belong to the group of gram-negative bacteria on which we will concentrate here. Fig. (2.3) shows a schematic view of the envelope of gram-negative bacteria. The inner cytoplasm is surrounded by the cytoplasmic membrane, consisting of a lipid bilayer and membrane proteins embedded in this layer. In the case of *E. Coli* one of these membrane proteins is ZipA (or FtsA) that serves as an anchor for the Z-ring. In other organisms equivalents of ZipA may exist. The inner and the outer membrane are separated by the periplasmic gel. In this gel, a network of peptidoglycan is responsible for sustaining the osmotic pressure difference between the bacterial cytoplasm and the surrounding medium. The peptidoglycan macromolecule (or murein) consists of sugar polymers that are covalently linked by oligopeptides and build up a very rough and stable network. Finally the periplasmic gel is surrounded by the outer cell membrane. In the second part of this thesis, we will study the deformation of the cell membrane by applying a radial constriction force. The exploration will be limited to the deformation of the cytoplasmic membrane, where the constriction is supposed to be initiated. Once the division process has started, the cell shape is remodelled and new wall material must be synthesized to build up the nascent cell poles. The influence of the peptidoglycan network and the outer cell wall on the deformation of the cytoplasmic membrane and the required constriction force are not yet clear. We will conclude this introductory chapter presenting the main mechanisms that are thought to generate the constriction force.

2.4. Two mechanisms of force generation

It is widely accepted, that FtsZ filaments generate part of the constriction force needed for cell division but the mechanism of this force generation is not yet clear. Currently two essentially different models are discussed. The first one assumes that the force is generated by filament bending, the second one is based on lateral bonding. Until present, the detailed structure of the Z-ring has not been visualized but images of FtsZ protofilaments *in vitro* together with *in vivo* measurements indicate its possible composition [3]. The number of FtsZ monomers inside the cell varies for different types of bacteria. Its order of magnitude is about 10000 (15000 for E. Coli [6], 5000 for Bacillus subtilis [7]). *In vitro*, FtsZ assembles into protofilaments with average length of 30 monomers [8, 9]. Only 30% of the total amount of FtsZ present in the cell is recruited to form the Z-ring [10, 11], so that in a typical E. Coli cell with a radius of 500 nm, the ring has a thickness of 3-5 protofilaments. Fig. (2.4) represents schematically the Z-ring and the two different force generating mechanisms.

2.4.1. Bending

Polymerization of FtsZ requires the presence of GTP (*Guanosine triphosphate*), which is bound between monomers and hydrolyzed to GDP (*Guanosine diphosphate*). The preferential curvature of the filament may depend on whether GTP or GDP is bound. The preferential angles between monomers are reported to be 0° for GTP bonds and 22° for GDP bonds [12, 13], although the mean curvature of experimentally observed filaments is not always the one we would expect as a result of the GTP-GDP ratio. In general the chains are straighter ([3]. Still, force might be

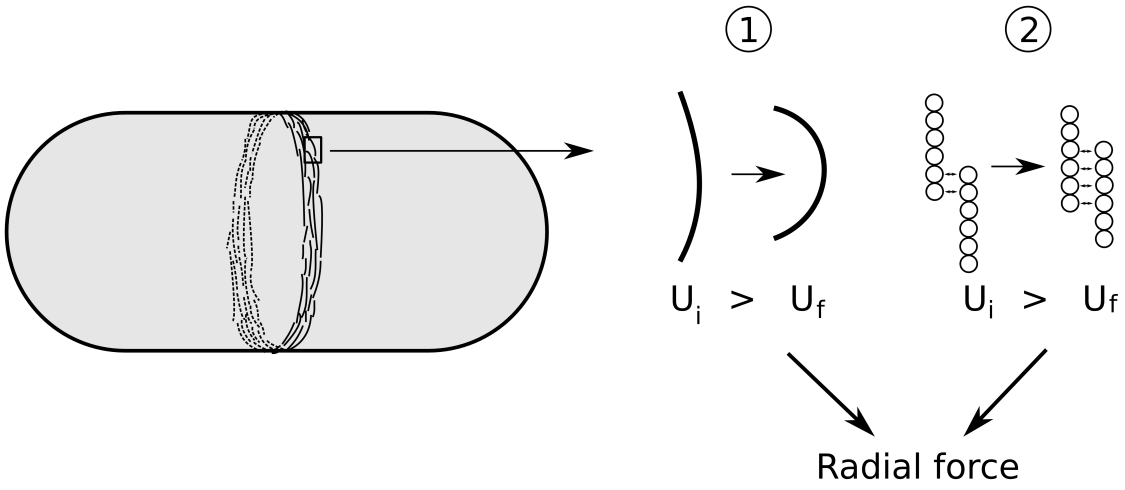

Figure 2.4.: Illustration of two possible force generating mechanisms. 1) Bending and 2) Lateral bonding.

generated due to the tendency of the filaments to augment their curvature (Fig. 2.4)) as GTP is hydrolyzed to GDP. The strength of the force generated by bending depends on the flexibility of the filaments and on their mean spontaneous curvature relative to the membrane radius.

2.4.2. Lateral bonding

FtsZ monomers are bound to their neighbours along the filament by strong covalent bonds, but experimental data show, that an additional lateral attraction between chains exists. The most obvious effect of this attraction is the condensation of filaments in compact structures like the Z-ring. Fig. (2.4) illustrates how this lateral bonding may contribute to force generation. Keeping the amount of proteins in the ring fixed, a smaller ring radius makes the ring thicker and increases the number of monomers with lateral contacts. The two mechanisms are not mutually exclusive, both may play an important role during the division process. The assumption, that FtsZ generates the constriction force is supported by recent experimental information from a simple bio-synthetic system [14] where FtsZ alone induces significant indentations in a lipid membrane. In this thesis, we have estimated the strength of the force generated by lateral bonding.

Part I.

FtsZ protein filaments

3. Experimental data and theoretical description

In the introductory chapter, we have seen in how far FtsZ protein filaments interact in the cell cycle, first of all in the process of cell division. The first part of this thesis is dedicated to the protein FtsZ and the mechanical aspects of its filaments. Therefore we have created an interaction model of the filaments based on AFM images. Langevin dynamics simulations and analytical considerations have contributed to estimate model parameters and predict filament behaviour in experimentally not yet accessible conditions. During the time period of this work, theoretical description and data analysis tools evolved in parallel with the experimental data. We will start this chapter summarizing the most important characteristics of the protein FtsZ and the filaments it forms.

3.1. FtsZ filaments - Experimental data

Before presenting the experimental AFM data on which our model is based, we will see some general information about FtsZ and its filaments.

3.1.1. General data

FtsZ is a 40 kDa globular protein, often described as a tubulin homologue. Tubulin plays an important role in the eukaryotic cytoskeleton forming microtubules which are essential for cell division. Although FtsZ and tubulin share less than 20% sequence homology, they have similar protein folds. The mostly conserved domains are the GTP binding residues, including the T7 loop (Fig. 3.1). Besides the structural homology, FtsZ and tubulin resemble in their polymerization mechanism. They polymerize in the presence of GTP which is immediately hydrolyzed to GDP. GDP containing bonds rapidly disassemble. Tubulin, which has been studied for much longer time is known to be a dimer consisting of two highly homologous subunits α and β that form microtubules comprised of 13 protofilaments [16]. *In vitro* experiments [17, 18] have shown the spontaneous self-assembly of the microtubules in bulk solutions of protein with GTP. In microtubules, nucleotide hydrolysis is coupled to complicated non-equilibrium behaviours like dynamic instability and treadmilling that have been described in simple physical models [19, 20]. In FtsZ polymers until now no evidence has been found for similar behaviours. *In vitro*, the shape of FtsZ filaments is highly dependent on experimental conditions as pH, temperature, concentration of GTP, GDP and several ions. Straight single-stranded filaments [9], tubules [21], double stranded filaments [22] as well as curved and circular forms [12, 23] have been described. Ribbon-like higher order structures have been observed in conditions that resemble the crowded intracel-

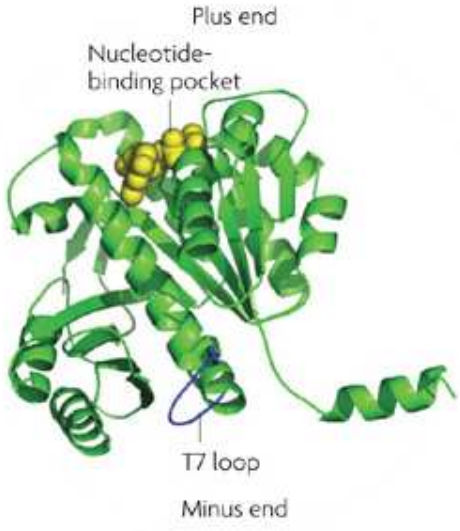

Figure 3.1.: Crystal structure of FtsZ [15] with bound GDP (circles) and the tubulin-like T7 loop

lular environment [24]. The angle between adjacent monomers in FtsZ filaments, the strength of their association and the flexibility of the bond depend on whether GTP or GDP is bound, but at present, little quantitative experimental information is available [25]. The process of nucleotide hydrolysis and exchange is not understood in detail and it is not clear, in which manner it affects structure and dynamics of FtsZ filaments. For tubulin and actin that form significantly larger filaments, the flexural rigidity of the polymers has been measured from optical microscopy images [26, 27, 28] that are not available for FtsZ. Recent atomic force microscopy experiments have allowed the observation of the dynamic behaviour of FtsZ filaments in different environmental conditions [23, 29, 30]. Our model of FtsZ filaments and the parameter estimations are based on these images.

3.1.2. AFM images of FtsZ filaments on mica

Atomic force microscopy is a powerful tool for visualizing shapes, growth, shrinkage and dynamics of FtsZ protein filaments. I will give a short description of how the filaments that we have analyzed were formed and imaged. Along the time period of this thesis, we have analyzed three main groups of experiments that differ in the experimental conditions and the type of observed structures. The theoretical interpretation has been carried out "realtime", evolving in parallel with the experiments. The first AFM images showed individual, single filaments at low density and compact spirals at higher densities [23]. The second group of experiments contained ring structures [30] and the most recent data [29] resemble the first group but different experimental conditions allowed higher resolutions and caused an additional anchorage between filaments and mica.

FtsZ - GDP-AlF_3: Open chain structures

In these experiments, FtsZ polymers were formed in solution upon addition of GTP to a FtsZ protein solution. A drop of this solution was then incubated over a mica surface. After a few minutes, the protein solution was removed and the samples were washed extensively. Then, after further few minutes, a buffer solution containing NaF and $AlCl_3$ was added. From that point on the evolution of the filament growth on the mica surface is followed for more than 1 hour. In the nucleotide exchange process, GDP was then replaced by GDP-AlF_3 instead of GTP. GDP-AlF_3 is an analog of GTP that inhibits the GTPase activity of FtsZ [31] and provides stable polymers with no time dependent monomer-monomer interactions in the time scale of our modeling. Fig. 3.2 shows an example of the shape evolution of the filaments during the growth process.

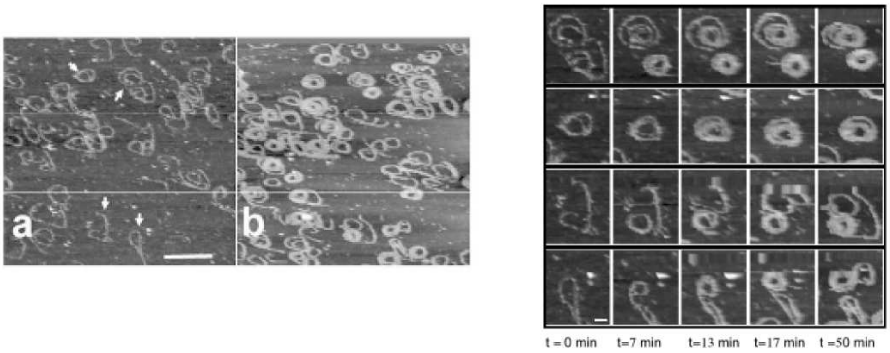

Figure 3.2.: AFM images of FtsZ filaments formed in presence of GDP-AlF_3. Left: (a) Image of filaments formed shortly after incorporation of the nucleotide. (b) Same filaments imaged 50 min later showing the shape evolution due to filament growth. The scale bar is 600 nm. Right: Filament evolution of the filaments indicated by an arrow in Fig. (a). Time zero is the first image taken after addition of GDP-AlF_3. Scale bar is 100 nm.

At low protein coverage, short, individual filaments with no lateral contacts between them can be observed. At higher densities the polymers form compact spirals establishing lateral contacts along the chain.

FtsZ - Ring structures

Ring structures were obtained in experiments with significantly lower protein concentration, below the critical concentration for polymerization in bulk. Polymerization took place on the mica surface. Another difference to the above described experiments was, that images were taken during the depolymerization process instead of the polymerization process. A drop of buffer solution, containing FtsZ (below the critical concentration for polymerization) and nucleotides was incubated over a mica surface during $\approx 30s$. The samples were then extensively washed to remove excessive protein. The buffer was interchanged, eventually modifying the pH-value, maintaining the nucleotide. In most cases, only stable ring structures (Fig. 3.3) remained on the surface and they were imaged every $\approx 60s$ until their depolymerization. The samples differ in the used nucleotides and pH-values:

nucleotide	GTP	GTP	GTP	GMPCPP
pH value	7.4	6.5	5.0	7.4

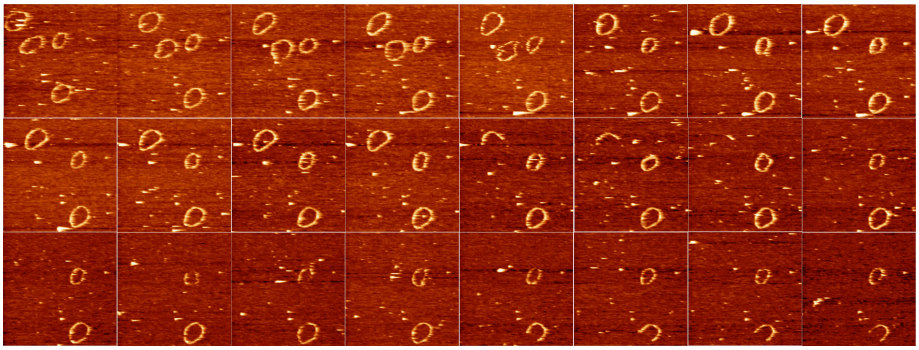

Figure 3.3.: Series of subsequent AFM images of FtsZ polymer rings in presence of GTP at pH=6.5. The time step between images is approximately one minute.

Anchorage filament - mica

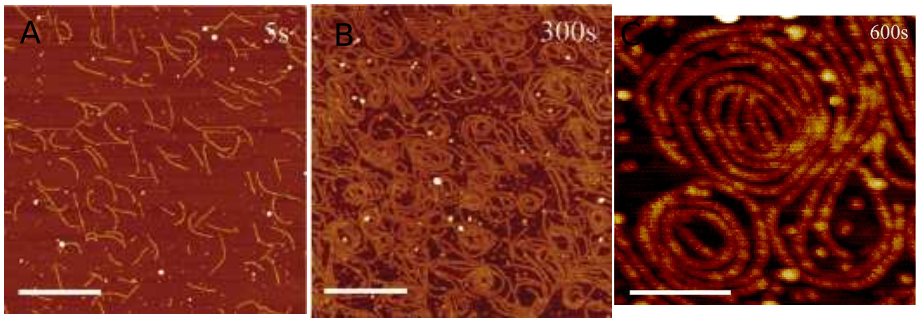

Figure 3.4.: Mica incubated with 80 nM FtsZ in polymerization buffer. The scale bar is 500 nm for A) and B). In Fig. C, the scale bar is 100 nm. Here individual monomers can be distinguished.

In the most recent experiments [29], mica was incubated with FtsZ in a polymerization buffer containing GTP for time spans between 5 and 600 seconds. Then mica was dried while the FtsZ structures that had been formed remained fixed. Compared to the AFM images taken in solution, the resolution of the now stable filaments could be increased significantly up to almost distinguishing individual monomers (Fig. 3.4C). The bulk concentration of FtsZ was kept below its critical concentration for polymerization so that the filaments were formed on the mica surface which strongly promotes polymerization. For the lowest incubation time of 5s a distribution of individual polymers (Fig. 3.4A) could be obtained. For longer incubation times the protein coverage on the surface considerably increased and the typical roll structures where found (Fig. 3.4C).

The first AFM images, showing open chain structures, were the basis of the developed chain

model that we will introduce in the next section.

3.2. Chain model of FtsZ-protein filaments

Biological macromolecules consist of hundreds or thousands of atoms. Many of these macromolecules give rise to higher structures, like molecular machines or filaments. A description of these systems at atomic level is too complex and depending on the process to be studied unnecessary. Here we want to analyse different aspects of filaments formed by FtsZ protein monomers. For this purpose, we do not need a detailed description of the inner structure of these monomers. It is much more important, to find a simple model with a very reduced number of parameters, able to describe the experimentally observed phenomenology of the filaments. In order to assure the flexibility of this model, it should be based on the simplified description of the monomers and its pairwise interactions. Experimental data should be used to determine the adequate interaction potentials which will include a set of parameters that may depend on the experimental conditions. An adequate model for FtsZ protein filaments should be able to describe essentially four experimentally observed characteristics:

- FtsZ monomers are approximately globular proteins with a size of $\simeq 4.5nm$.
- Monomers are organized in a linear chain, connected to their direct neighbours by strong bonds.
- Filaments show up a certain bending rigidity.
- In some experiments a spontaneous curvature of the filaments is observed.
- High density of filaments leads to lateral attraction between them.

Along this work, we will treat four kinds of chains (Fig. 3.5):

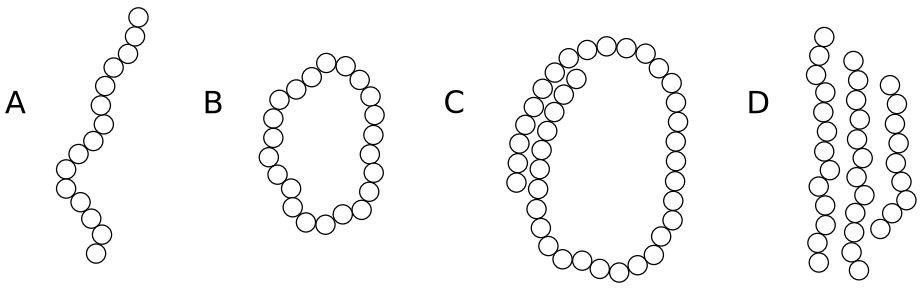

Figure 3.5.: A) Short, individual filament B) Circular filament C) Long filament with lateral contacts D) Set of interacting filaments

- Short, individual chains without lateral contacts
- Individual filaments with a bond connecting its extremes (circular shapes)
- Long filaments with lateral contacts between different parts of the chain

- Sets of filaments hold together by lateral bonds between them

We represent the FtsZ monomers as beads in a chain. Fig. 3.2 schematically shows the "internal structure" of these beads, the interaction between direct neighbours. We characterize this interaction by two springs, fixing the optimal distance and angle between monomers and their ability to fluctuate around these values. Therefore we have to use four parameters, shown in Table (3.1).

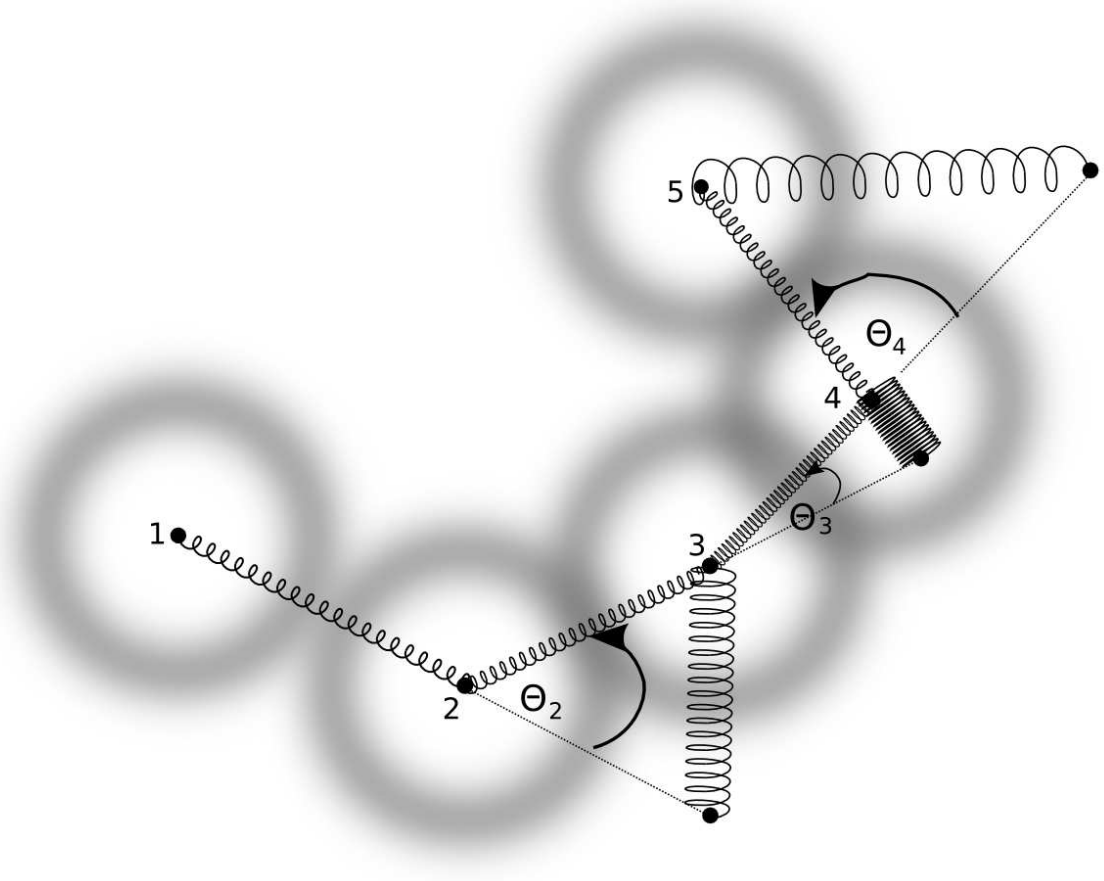

Figure 3.6.: Zoom into the "inner structure" of a chain of FtsZ monomers. Two types of springs are represented. The thin springs control the distance between monomers, the thicker springs their angle. Monomers 2-3 and 4-5 are separated by their optimal distance, d. The spring is stretched between monomers 1-2 and compressed between monomers 3-4. θ_2 is the spontaneous curvature, at θ_3 the angle spring is compressed, at θ_4 it is stretched. For better illustration angles and spring deformations are exaggerated.

A third interaction has to be added for volume (area) exclusion and lateral contacts between the monomers of one or more chains (Fig. 3.5 C and D). Here we use a Van-der-Waals type potential, determined by an equilibrium distance and the depth of the potential. Table (3.1) contains the corresponding parameters compatible with the experimental results. Including all terms, the potential energy of a FtsZ polymer chain is

covalent bond		curvature		lateral interaction	
bond equil. distance	d	spontaneous curvature	θ_o	lateral equil. distance	σ
spring constant	κ_b	bending rigidity	κ_c	potential depth	ϵ

Table 3.1.: Model parameters for monomer-monomer interactions in FtsZ filaments

$$U = \sum_{i=2}^{N} \frac{\kappa}{2}(R_i - d)^2 + \sum_{i=2}^{N-1} \frac{\kappa_c}{2}(\theta_i - \theta_0)^2 + \sum_{i>j} 4\epsilon \left[\left(\frac{\sigma}{|\mathbf{r}_i - \mathbf{r}_j|} \right)^{12} - \left(\frac{\sigma}{|\mathbf{r}_i - \mathbf{r}_j|} \right)^{6} \right]. \quad (3.1)$$

$\mathbf{r}_i$ is the position of the ith monomer. To ease notation we have introduced the following variables:

$$\mathbf{R}_i = \mathbf{r}_i - \mathbf{r}_{i-1}, \qquad R_i = |\mathbf{R}_i| \quad (3.2)$$

Before we will start the theoretical analysis and the simulations of the polymer chains we will have a look of each of the three contributions to the potential energy, justify the choice of the potentials and find reasonable ranges for the parameters.

The bond potential

FtsZ monomers are connected by strong, covalent bonds. For these covalent bonds we assume a harmonic potential. As long, as we handle chains with a fixed number of monomers the exact strength of this potential is not relevant. In the simulation two aspects are important. κ_b must be large enough to allow only very small displacements from equilibrium bond length and to make it impossible to break up the bond by thermal processes. On the other hand, κ_b has to be chosen low enough to allow an efficient sampling along the simulation. The bond length is comparable to the diameter of FtsZ, $d \simeq 4.5nm$, and we have set $\kappa = 200kT$. In fact, the strength of this bond depends strongly on whether GTP or GDP is bound to the protein (GTP favouring a strong bond) and slightly on the chemical environment. The use of a nonhydrolyzable analogue of GTP as in our experimental AFM data will also change the strength of the bond. All in all, in our chain model, the covalent bond between monomers has the following characteristics:

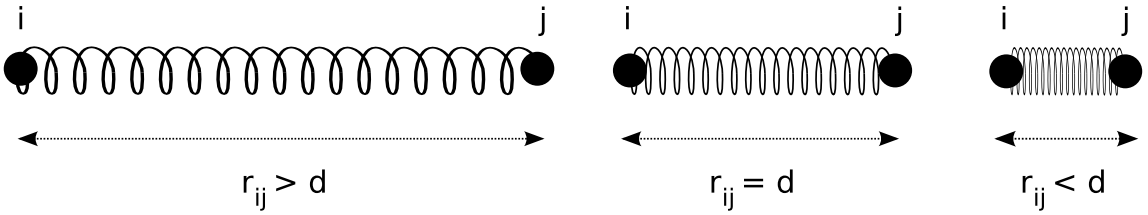

U_b	d	κ_b
$\sum_{i=2}^{N} \frac{\kappa}{2}(R_i - d)^2$	$4.5nm$	$200kT$

The curvature potential

Experimental data show that FtsZ forms flexible filaments about half way between a perfectly stiff chain and a random coil. Further, in some experiments we observe a clear tendency to form curved polymers. We use again a harmonic potential to describe these phenomena. The preferential curvature, θ_o, and the bending rigidity ,κ_c, will depend on the experimental conditions and in this work we have estimated in which way they do so. θ_o determines the equilibrium radius of a circular structure to d/θ_o. For $\theta_o = 0$, straight lines are formed. We expect to find values of θ_o between 0 for straight filaments and $\theta_o \simeq 2\pi/40$ for the shortest observed circles made of ≈ 40 monomers. Of course, this is only a very rough estimation and the preferential curvature is not the only parameter that determines the size of the circular shapes. An estimation of the expected bending rigidities can be found across the polymer persistence length, $l_p = \kappa_c/kT$, which seems to be of the order of magnitude of the typical filament length, $N \approx 100$, so that we may set as an upper and lower limit $10 < \kappa_c/kT < 1000$. The following illustration and table summarize our model of the curvature potential.

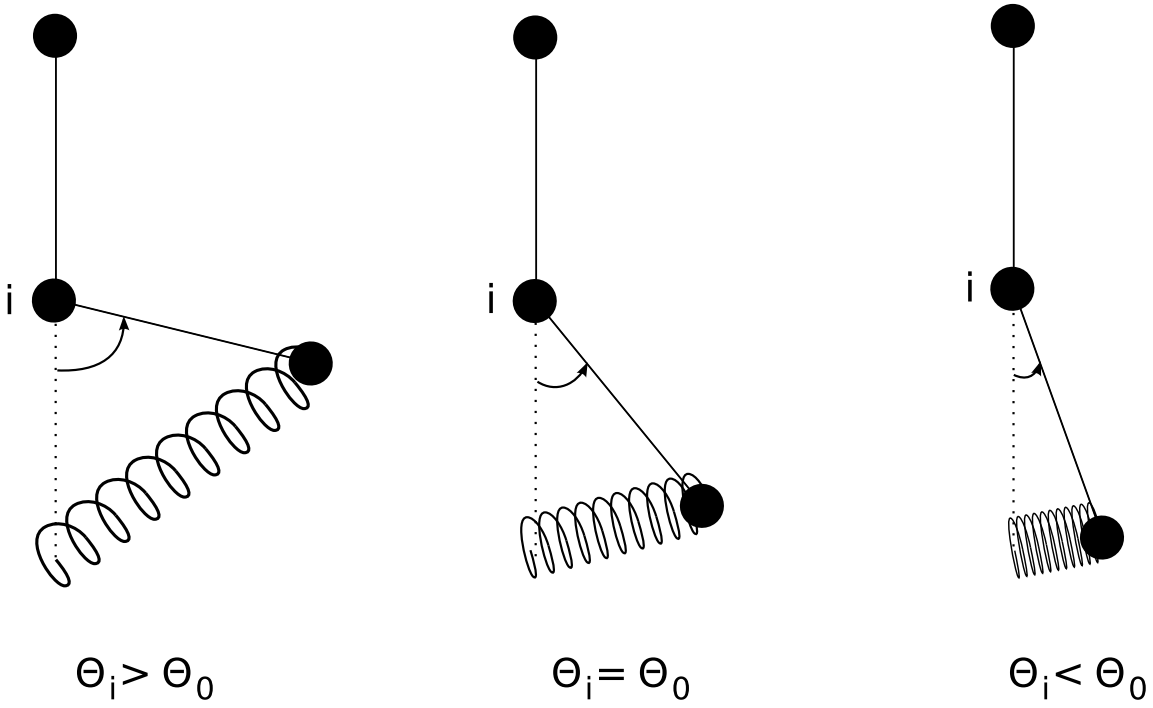

U_b	θ_o	κ_c
$\sum_{i=2}^{N-1} \frac{\kappa_c}{2}(\theta_i - \theta_o)^2$	$0 - 2\pi/40$	$30 - 1000kT$

Lateral interaction potential

In the case, that two non-neighbouring monomers along the chain or monomers from different chains get close enough, an interaction between these monomers - we will call it a lateral interaction - takes place. The experimentally observable result of this interaction in two dimensions

is the condensation of the filaments into loops or parallel strands. Although the particular shape of the potential that gives rise to this phenomenon is not accessible experimentally, we state two clear tendencies: slight attraction at long ranges and strong repulsion at short ranges. We assume the potential to be of Van-der-Waals type, arising from an induced polarisation of the monomers getting close to each other. In concrete we chose a Lennard-Jones potential between monomer pairs. Its attractive $1/r^6$ dependency (the dipole-dipole interaction) and the repulsive $\sim 1/r^{12}$ term take into account the two observable tendencies of long-range attraction and short-range repulsion. Again, we have to determine two parameters, the equilibrium bond length, $2^{1/6}\sigma$, and the corresponding depth of the potential, ϵ. σ depends strongly on the experimental conditions. As a lower limit we can set the monomer diameter, d. ϵ, also depending on the experimental conditions, should be of the order of kT, allowing the formation and breaking of bonds as a thermal process. After a short summary of the lateral interaction potential we will continue with the next section, the simulation of FtsZ protein filaments.

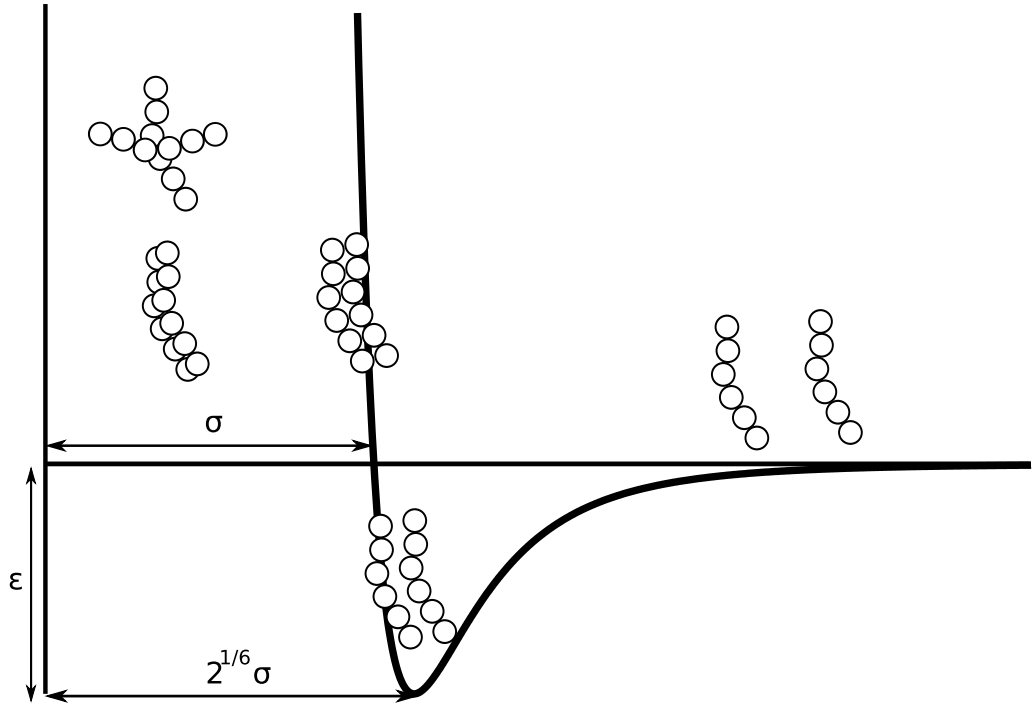

U_{lat}	σ	ϵ
$\sum_{i>j} 4\epsilon \left[\left(\frac{\sigma}{\lvert \mathbf{r}_i - \mathbf{r}_j \rvert} \right)^{12} - \left(\frac{\sigma}{\lvert \mathbf{r}_i - \mathbf{r}_j \rvert} \right)^{6} \right]$	$> d$	$0 - 10kT$

3.3. Filaments in Langevin Dynamics simulations

Along this work, we have used different theoretical and simulation techniques to analyse the shape and dynamics of FtsZ protein filaments. Langevin dynamics (LD) simulations allowed us to reproduce experimental AFM results and estimate the model parameters. In principle, LD

simulations are molecular dynamics (MD) simulations where two additional force terms are added to Newtons equations of motion. A frictional force and a random force. Both of them account for the presence of solvent molecules that are not explicitly treated in LD simulations. We will start with a short introduction to MD simulations.

3.3.1. Molecular dynamics

MD is the main theoretical tool of analysis of the collective properties of biological (and other) molecules. Being a classical dynamics, deterministic technique, MD describes the evolution in time and space of a molecular system following the trajectories of each of its components based on solving Newton's equations of motion, first of all $F_i = m_i a_i$. In principle, the trajectories of all particles are determined for any point in time for a specific set of initial conditions (coordinates and momenta of all particles). Anyhow, due to the limited accuracy of all numerical techniques it is not possible to determine exact trajectories. The calculated trajectories are not even close to the real ones as small fluctuations in the initial conditions cause exponential divergence, a phenomenon known as Lyapunov instability. However, it is not necessary to worry about this fact as the purpose of MD, more than to predict exact trajectories, is to obtain statistical properties of the system. We can distinguish different types of MD simulations, depending on their spatial and temporal resolutions.

- Atomistic MD simulations use the exact positions of each atom of a molecular system and force fields that contain the interaction between each pair of atoms. The resolution is high and the method is suitable to study processes at time scales of nanoseconds and system sizes of a few thousand atoms. One example of a very high-effort simulation was realized in 2006 [32], when the complete satellite tobacco mosaic virus was simulated during 50 ns. The size of this system is about 1 million atoms and the simulation would have taken about 35 years on a single desktop computer. In general, for large systems and/or timescales atomistic MD simulations are not possible with standard equipment. A frequent solution in these cases is a coarse-grained simulation.

- In coarse-grained simulations a group of atoms is represented by a "pseudo-atom". In that way, larger systems can be simulated during longer times, paying the price of a reduced resolution. In this work, we will use extremely coarse-grained simulations, representing the whole FtsZ-protein as one monomer. In that way, we can simulate filaments of typically about 50-200 monomers during simulation times that are longer than the required equilibration time of the systems. Further, we have to include the effect of the solvent molecules in our simulation. We can not do that explicitly, as the number of solvent molecules in such a large system is enormous. An implicit form to account for the solvent molecules is used in Langevin dynamics (LD) simulations.

3.3.2. Langevin dynamics

LD simulations offer the possibility to introduce additional degrees of freedom in form of a heat bath. In systems like proteins in solutions, it is often not necessary (apart from computationally

impossible) to treat each solvent molecule like an individual particle in a MD simulation. It is much more important to know, how the collectivity of the solution takes influence on the proteins. This influence will have statistical character and it is introduced in Newton's equations in form of a stochastic force that has two effects. On the one hand, the interaction with the solvent molecules causes the particles to loose their directional acceleration but at the same time the particles experience a non-directional, random force which has to be added to the external force in order to give the total force acting on a particle:

$$m\frac{d^2\mathbf{r}}{dt^2} = \mathbf{F} + \xi - \frac{\mathbf{v}}{\mu}, \tag{3.3}$$

where F is the external force on each particle, $\mathbf{r}$ and $\mathbf{v}$ its position and velocity, μ the mobility coefficient and ξ the random force. Here, we are interested in the overdamped limit of Eq. (3.3) where the inertial term can be neglected. This approximation is valid in the situation where the mass ratio between solvent and solved molecules is high, so that the displacement of a particle until reaching a Maxwellian velocity distribution is negligible compared to its size [33]. Eq. (3.3) then reduces to

$$\mathbf{v} = \mu\mathbf{F} + \xi. \tag{3.4}$$

Langevin dynamics in this limit is referred to as Brownian dynamics. The random forces, ξ, describe the Brownian diffusion process of the particles with zero mean displacement and root mean square displacement corresponding to the diffusion laws for each direction x_i,

$$< x_i(t) - x_i(t+\Delta t) > \;=\; 0, \tag{3.5}$$

$$< (x_i(t) - x_i(t+\Delta t))^2 > \;=\; 2D\Delta t. \tag{3.6}$$

The friction and the diffusion of the particles have the same origin and are linked to each other by the Einstein relation, $\mu D = kT$. The forces that generate this displacement are not time correlated and can be expressed like

$$< \xi_i(t)\xi_i(t') >= \frac{2kT}{\mu\Delta t}\delta(t-t'), \tag{3.7}$$

where $\delta(t-t')$ is the Dirac distribution. We will continue with a brief summary of how we realized the simulations and how we generated the random forces for discrete time steps.

3.3.3. How is the simulation done?

In the first instance, we have realized simulations of one (or several) filaments of FtsZ with fixed length. Our starting conditions where the positions of each of the monomers in the chain. One time step consisted in:

- Calculation of the forces that act on each monomer caused by:

1. Pair interactions with all other particles in the chain
2. Random force

The velocity of each monomer at time t is then given by Eq. (3.4).

- Update of the position of each monomer,

$$\mathbf{r}(t+\Delta t) = \mathbf{r}(t) + \mathbf{v}(t)\Delta t. \tag{3.8}$$

In the simulations we generated the thermal Brownian forces ξ_i by a producer of Gaussian distributed random numbers with mean squared amplitude equal to $\frac{2kT}{\mu\Delta t}$,

$$\Pi(\xi_i) = \sqrt{\frac{\mu\Delta t}{4\pi kT}} \exp\left(-\frac{\xi_i^2 \mu\Delta t}{4kT}\right). \tag{3.9}$$

$\Pi(\xi)$ is the probability distribution for the ith component of the random force ξ_i. The dependence on the time step, Δt, can be understood calculating the mean square displacement of the particles due to the random forces,

$$< (x_i(t) - x_i(t+\Delta t))^2 >= v_x \Delta t = \frac{2kT}{\mu\Delta t}\Delta t, \tag{3.10}$$

equal to Eq. (3.6). So, although ξ_i increases for decreasing time step, the corresponding particle displacement grows linearly with Δt following the laws of a Brownian diffusion process. In the next section, we will briefly deduce the forces that act on the monomers due to the pair interactions with the other monomers along the chain.

3.3.4. Interaction forces

In this purely technical section, we calculate the forces, acting on each monomer as the derivatives of the interaction potential with respect to the monomer position. We will start with the forces resulting from the bond potential. We will use the following notation:

$$R_{ij} = (\mathbf{R}_i)_j, \qquad r_i = |\mathbf{r}_i|, \qquad x_{ij} = (\mathbf{r}_i)_j \tag{3.11}$$

Bond forces

Let F_{kl}^b be the lth component of the bond force vector on the kth monomer,

$$F_{kl}^b = -\frac{\partial U_b}{\partial x_{kl}} = -\kappa \sum_{i=1}^{N-1} .(R_i - d)\frac{\partial R_i}{\partial x_{kl}}$$

Keeps calculating the remaining derivative,

$$\frac{\partial R_i}{\partial x_{kl}} = \frac{\partial}{\partial x_{kl}}\left[\sum_{j=1}^{2}(x_{ij} - x_{i-1,j})^2\right]^{1/2} = \frac{1}{R_i}\sum_{j=1}^{2} R_{ij}\left(\frac{\partial x_{ij}}{\partial x_{kl}} - \frac{\partial x_{i-1,j}}{\partial x_{kl}}\right) = \frac{R_{il}}{R_i}\left(\delta_{ik} - \delta_{i-1,k}\right).$$

δ_{ik} is the Kronecker delta. We finally get for the bond force

$$F^s_{kl} = -\kappa(R_k - d)\frac{R_{kl}}{R_k} + \kappa(R_{k+1} - d)\frac{R_{k+1,l}}{R_{k+1}}. \tag{3.12}$$

Curvature forces

For F^c_{kl} being the lth component of the curvature force acting on particle k, we get

$$F^c_{kl} = -\frac{\partial U_c}{\partial x_{kl}} = -\kappa_a \sum_{i=2}^{N-1}(\theta_i - \theta_o)\frac{\partial \theta_i}{\partial x_{kl}}.$$

In terms of monomer positions, the bond angle θ_i can be written like

$$\theta_i = \arccos\left[\frac{\mathbf{R}_i\mathbf{R}_{i+1}}{R_i R_{i+1}}\right]. \tag{3.13}$$

Now we calculate the remaining derivative:

$$\begin{aligned}
\frac{\partial \theta_i}{\partial x_{kl}} &= -\frac{1}{\sqrt{1-\cos\theta_i{}^2}}\frac{1}{R_i^2 R_{i+1}^2}\left[R_i R_{i+1}\left(\frac{\partial}{\partial x_{kl}}\sum_{j=1}^{2} R_{ij}R_{i+1,j}\right) - \right. \\
&\quad \left. \mathbf{R}_i\mathbf{R}_{i+1}\left(R_i\frac{\partial R_{i+1}}{\partial x_{kl}} + R_{i+1}\frac{\partial R_i}{\partial x_{kl}}\right)\right] \\
&= -\frac{1}{\sqrt{1-\cos\theta_i{}^2}}\frac{1}{R_i R_{i+1}}\left[(\delta_{ik} - \delta_{i-1,k})R_{i+1,l} + (\delta_{i+1,k} - \delta_{ik})R_{il} - \right. \\
&\quad \left. \cos(\theta_i)\left(\frac{R_i R_{i+1,l}}{R_{i+1}}(\delta_{i+1,k} - \delta_{ik}) + \frac{R_{i+1}R_{il}}{R_i}(\delta_{ik} - \delta_{i-1,k})\right)\right].
\end{aligned}$$

And the curvature force becomes

$$\begin{aligned}
F^c_{kl} &= \frac{\kappa_c(\theta_{k-1} - \theta_o)}{\sqrt{1-\cos(\theta_{k-1})^2}}\left[\frac{R_{k-1,l}}{R_{k-1}R_k} - \frac{R_{kl}}{R_k^2}\cos(\theta_{k-1})\right] \\
&+ \frac{\kappa_c(\theta_k - \theta_o)}{\sqrt{1-\cos(\theta_k)^2}}\left[\frac{R_{k+1,l} - R_{kl}}{R_k R_{k+1}} + \left(\frac{R_{k+1,l}}{R_{k+1}^2} - \frac{R_{kl}}{R_k^2}\right)\cos(\theta_k)\right] \\
&+ \frac{\kappa_c(\theta_{k+1} - \theta_o)}{\sqrt{1-\cos(\theta_{k+1})^2}}\left[-\frac{R_{k+2,l}}{R_{k+1}R_{k+2}} + \frac{R_{k+1,l}}{R_{k+1}^2}\cos(\theta_{k+1})\right].
\end{aligned} \tag{3.14}$$

Lateral interaction force

Finally, we will derive the lateral forces resulting from the Lennard-Jones potential,

$$F^{LJ}_{kl} = -\frac{\partial U_{lat}}{\partial x_{kl}} = 48\frac{\epsilon}{\sigma}\sum_{i>j}\left[\left(\frac{\sigma}{|\mathbf{r}_i - \mathbf{r}_j|}\right)^{13} - \frac{1}{2}\left(\frac{\sigma}{|\mathbf{r}_i - \mathbf{r}_j|}\right)^{7}\right]\frac{\partial|\mathbf{r}_i - \mathbf{r}_j|}{\partial x_{kl}}, \tag{3.15}$$

with

$$\begin{aligned}\frac{\partial|\mathbf{r}_i-\mathbf{r}_j|}{\partial x_{kl}} &= \frac{\partial}{\partial x_{kl}}\left[\sum_{m=1}^{2}(x_{im}-x_{jm})^2\right]^{1/2} \\ &= \frac{1}{|\mathbf{r}_i-\mathbf{r}_j|}\sum_{m=1}^{2}(x_{im}-x_{jm})\left(\frac{\partial x_{im}}{\partial x_{kl}}-\frac{\partial x_{jm}}{\partial x_{kl}}\right)=\frac{x_{il}-x_{jl}}{|\mathbf{r}_i-\mathbf{r}_j|}\left(\delta_{ik}-\delta_{jk}\right).\end{aligned}$$

The lateral interaction forces caused some technical problems in the simulations. Actually, they are supposed to account for the interaction between monomers with no direct bonding that get in contact with each other because two different chains get close or because one large chain forms a loop. Later on, we will show, that the equilibrium distance of the lateral interaction is about 2 and a half times the diameter of the monomers. For individual filaments, we started by calculating the corresponding forces for monomer pairs separated by at least 10 longitudinal bonds to avoid unphysical repulsion between adjacent monomers. Like this, from time to time the monomers in between were pressed together due to the attraction between monomers i and $i+10$ which was not compensated by a repulsion (other than the repulsion resulting from the spring bond potential). We therefore introduced a Lennard Jones potential between a monomer and its first nine neighbours along the chain with the same potential depth but an equilibrium distance equal to the monomer diameter. In that way, we achieved the necessary repulsion without changing too much the bond interaction between one monomer and its direct neighbour for distances close to the equilibrium distance. We should further mention here that we calculated the Lennard Jones forces for monomers separated by a distance less than the cutoff distance of 2.5σ. To conclude this chapter I will give a short overview of the units used in the simulations.

3.3.5. Units

We have realised all simulations in reduced units, setting kT, σ and μ (the mobility coefficient) equal 1. In the following table we will give an overview of relevant magnitudes and their units:

energy	length	velocity	force	time
kT	σ	$\frac{\mu kT}{\sigma}$	$\frac{kT}{\sigma}$	$\frac{\sigma^2}{\mu kT}$

To compare simulation times with experimental times, we will give a rough estimation of the order of magnitude for a time unit. If we consider the monomers as spheres moving in an aqueous environment (this means of course a strong simplification that does not take into account the viscous properties of the substrate), the mobility coefficient can be determined by Stoke's friction law,

$$\mu=\frac{1}{6\pi\eta R}\approx 2\cdot 10^{10}\frac{m}{Ns}, \tag{3.16}$$

using the radius of a monomer $R=2.25nm$ and the viscosity of water at room temperature $\eta=1.0mPas$. The final estimation of the time unit includes $\sigma=12nm$ and $kT=4\cdot 10^{-21}J$,

$$[t] = \frac{\sigma^2}{\mu kT} = 2 \cdot 10^{-6} s. \tag{3.17}$$

The estimation for the mobility coefficient can only provide an upper limit. In reality, μ will be some orders of magnitude smaller due to the viscous effects of the substrate. We used typical, undimensional simulation times of order 10^2 to 10^3, which would then correspond to experimental times in the order of milliseconds to seconds, reasonable compared to the actual time scales of the experiments. Later on, for simulations of closed ring structures we will use an alternative calibration of the time scale, allowing for a more precise estimation.

4. Open chain structures in 2D

The experimental AFM data can be roughly divided into two types. In this chapter, we will treat what we call "open" chain structures. That means that the first and the last monomer of the filament are not connected by a bond. We still find different configurations. Single filaments without lateral contacts, loop forming chains and sets of laterally interacting parallel filaments. The samples that we analyzed here, were the first AFM images of FtsZ polymers obtained by the collaborating experimental group and our model of monomer-monomer interactions is based on these images. Their analysis marks the beginning of a continuous evolution of and interaction between experiments and theoretical interpretation. The basic monomer-monomer interaction model resulted to be robust and could be maintained throughout the time period of this work, but the estimation of the model parameters and the extraction of information from experimental data have been corrected and improved continuously. At first, we concentrated on single filaments and the relation between the different shapes and the interaction parameters κ_c and ϵ. We will start by an analytical interpretation, using a continuous version of our chain model, and continue by LD simulations of the above presented discrete chain model.

4.1. Analytical interpretation of filament configurations - continuous Model

For an analytical interpretation of filament conformations we introduce a simplified chain model. We pass to a continuous description and use polar coordinates so that the monomer positions are determined by their radius, $R(\varphi)$, and angle, φ, with respect to a chosen origin. We cancel the bond energy that is important only for an efficient sampling in the simulations and reduce the contributions to the chain energy to curvature and lateral interactions. The energetic minimum depends here on the ratio $\frac{\epsilon}{\kappa_c}$, the spontaneous curvature, θ_0, and on the chain length and gives a first idea about the different configurations we may expect. Entropic effects are not included in this analytical model so that all loop configurations are perfect spirals.

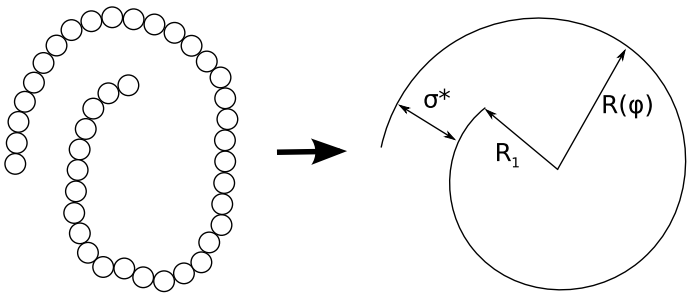

Figure 4.1: Illustration of the transition between a discrete model of spiral shapes and a continuous description of perfect spirals without entropic effects.

Within this description, the simplest parametrization of a chain with spiral shape is as follows:

$$R(\varphi) = R_1 + \frac{\sigma^*}{2\pi}\varphi, \qquad 0 < \varphi < \varphi_N, \tag{4.1}$$

where σ^* is the loop pitch and R_1 the inner radius. We imagine, that one monomer occupies a filament segment of length $f\sigma^*$. If the total length of the string is L, the number of monomers, N is:

$$N = \frac{L}{f\sigma^*} = \frac{1}{f\sigma^*}\int_0^{\varphi_N} R(\varphi)d\varphi = \frac{\varphi_N R_1}{f\sigma^*} + \frac{\varphi_N^2}{f4\pi}. \tag{4.2}$$

φ_N is the angle coordinate of the last monomer. The curvature of the filament with an initial curvature $\theta_1 = \frac{f\sigma^*}{R_1}$ is

$$\theta(\varphi) = \frac{f\sigma^*}{R(\varphi)} = \frac{1}{\frac{1}{\theta_1} + \frac{\varphi}{2\pi f}}. \tag{4.3}$$

Before we start to calculate the curvature and the lateral interaction energy terms, we will replace the sum over monomers by an integral over the curvature. Therefore we will replace $R(\varphi)$ in Eq. (4.2) by $\theta(\varphi)$:

$$N = \int_0^{\varphi_N} \frac{d\varphi}{\theta(\varphi)} = 2\pi f \int_{\theta_N}^{\theta_1} \frac{d\theta}{\theta^3} \tag{4.4}$$

Integration of Eq. (4.4) gives the curvature at the end of the filament, $\theta_N = \frac{\theta_1}{\sqrt{1+\frac{N\theta_1^2}{\pi f}}}$. We will now first calculate the curvature potential and then continue with the lateral interaction potential.

Curvature potential

In the curvature potential introduced in Chp. (3), we replace the sum over all monomers by the integral over the curvature, Eq. (4.4):

$$\begin{aligned} U_c &= \kappa_c \pi f \int_{\theta_N}^{\theta_1} d\theta \frac{(\theta - \theta_o)^2}{\theta^3} \\ &= \kappa_c \pi f \left[\ln \sqrt{1 + N\frac{\theta_1^2}{\pi f}} - \frac{2\theta_0}{\theta_1}\left(\sqrt{1 + N\frac{\theta_1^2}{\pi f}} - 1 \right) + \frac{\theta_0^2 N}{2\pi f} \right]. \end{aligned} \tag{4.5}$$

Lateral interaction potential

For the analytical estimations we will make some approximations about the lateral interaction potential, assuming that one monomer with lateral neighbours on both sides contributes an amount of $-\epsilon^*$ to the lateral interaction energy and monomers with only one neighbour strand (this is the case for the first and the for the last turn of the loop) give a contribution of $-\frac{\epsilon^*}{2}$:

$$U_{lat} = -\frac{\epsilon^*}{2}\left[N + \pi f \left(\frac{1}{\theta_i^2} - \frac{1}{\theta_f^2} \right) \right].$$

θ_i is the curvature of the chain at the beginning of the second turn and θ_f is the curvature at the beginning of the last turn. Leaving out some calculation steps, we finally get:

$$U_{lat} = -\epsilon^* \left[N - \frac{\pi}{\theta_1} \left(\sqrt{1 + \frac{N\theta_1^2}{\pi f}} + 1 \right) \right] \tag{4.6}$$

The condition for having more than one turn and hence lateral interaction is that the initial curvature θ_1 exceeds $\frac{2\pi}{N}$. ϵ^* might be seen as an effective potential depth, including the interaction of one monomer with all its lateral neighbours. It can be estimated by building an average over all possible positions of a monomer with respect to the neighbour chain. The equilibrium chain conformation is a balance between the optimization of the curvature cost and the lateral interaction gain. For high spontaneous curvatures and strong lateral interaction we expect closed packed loops, whereas for vanishing spontaneous curvatures and stiff chains linear shapes will be preferred. Minimization of the total chain energy allows for setting up a phase diagram of the qualitatively different shapes that we expect to find.

Phase diagram of filament shapes

We can express the total chain energy, U_{tot} like

$$\begin{aligned} \frac{U_{tot}}{f\pi\kappa_c} &= \frac{U_c + U_{lat}}{f\pi\kappa_c} \\ &= \frac{1}{2}\ln(1+x^2) - \frac{2x_0}{x}(\sqrt{1+x^2} - 1) + \frac{\xi}{fx}\left(\sqrt{1+x^2} + 1\right) + const, \end{aligned} \tag{4.7}$$

with

$$x \equiv \theta_1 \sqrt{\frac{N}{f\pi}}, \qquad x_0 \equiv \theta_0 \sqrt{\frac{N}{f\pi}}, \qquad \xi \equiv \frac{\epsilon^*}{\kappa_c}\sqrt{\frac{N}{f\pi}}. \tag{4.8}$$

As in this simplified model the distance between monomers as well as the loop pitch are fixed, the shape of the filament is completely determined by the initial curvature, θ_1 (or x using the reduced variables). We find the energetic minimum by setting $\frac{dU_{tot}}{dx} = 0$,

$$\frac{x}{1+x^2} + \frac{2x_0}{x^2}(\sqrt{1+x^2} - 1) - \frac{2x_0}{\sqrt{1+x^2}} + \frac{\xi}{f}\left(\frac{1}{\sqrt{1+x^2}} - \frac{\sqrt{1+x^2}+1}{x^2}\right) = 0. \tag{4.9}$$

As mentioned above, the shape of the filament is determined by θ_0 and $\frac{\epsilon^*}{\kappa_c}$. We can distinguish three qualitatively different conformations. The first one is an open chain form, where lateral interactions play no role. As we have seen above it is characterized by $\theta_1 > \frac{2\pi}{N}$. The second one closes the chain to a spiral but leaves a "hole" in the centre distinguishing it from the last conformation, the closed packed form, where $\theta_1 \approx 1$ ($f\sigma^* \approx R_1$). As we cannot find a closed analytical solution of Eq. (4.9) we we will consider the two extremes $\theta_0 = 0$ and $\epsilon^* = 0$ which will give us two boundary values of the shape diagram.

$\underline{\theta_0 \to 0}$

Eq. (4.9) reduces to $fx^3 = 2(\xi + \xi x^2)$. The shape transitions take place for $\theta_1 \simeq \frac{2\pi}{N}$ ($x \ll 1$) at $\frac{\epsilon^*}{\kappa_c} \simeq \frac{4\pi^2}{fN^2}$ and for $\theta_1 \approx 1$ ($x \gg 1$) at $\frac{\epsilon^*}{\kappa_c} \simeq \sqrt{\frac{fN}{\pi}}$.

$\underline{\epsilon^* \to 0}$

Here Eq. (4.9) reduces to $\frac{x}{1+x^2} + \frac{2x_0}{x^2}(\sqrt{1+x^2} - 1) - \frac{2x_0}{\sqrt{1+x^2}} = 0$. The shape transitions take place for $\theta_1 \approx 1$ at $\theta_0 \simeq \frac{1}{2}\sqrt{\frac{N}{f\pi}}$ and for $\theta_1 \simeq \frac{2\pi}{N}$ at $\theta_0 \simeq \frac{2\pi}{N}$.

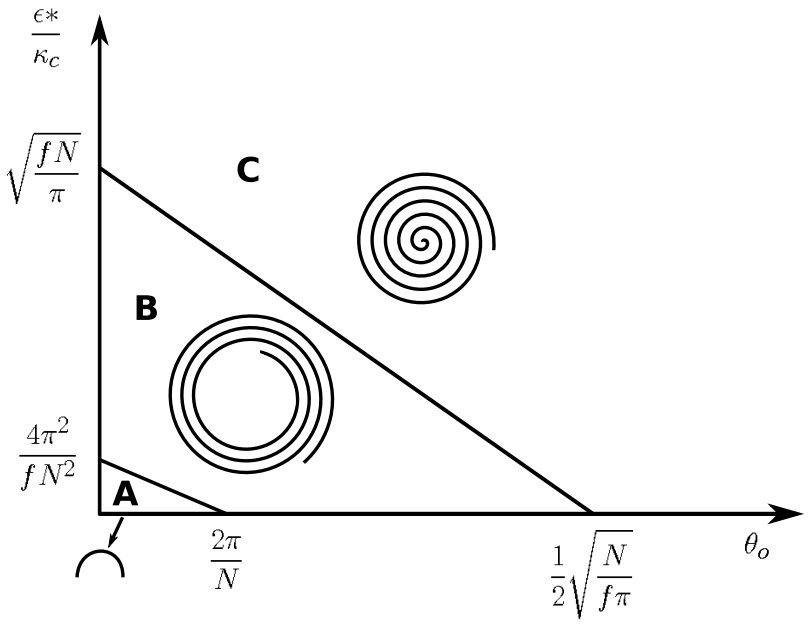

Figure 4.2.: Shape diagram of qualitatively different filament shapes. A) Shapes without lateral contacts. B) "Open" loops. C) Closed packed loops. The transition from A to B is first order-like as the mean curvature of the filament, θ_m, jumps from the value of the spontaneous curvature, θ_o, to a much higher value in the spiral shape. The transition from B to C is of second order with discontinuity in the derivative of θ_m with respect to $\frac{\epsilon^*}{\kappa_c}$.

The different aspects of the chain are represented in Fig. 4.2. The transition from the open chain (A) to a closed spiral (B) brings about a jump in the average curvature of the filament from $\theta_m = \theta_o$ to a much higher value in the spiral. For fixed filament length, this transition occurs for increasing strength of the lateral contacts as shown in Fig. 4.3 or increasing θ_o. The further transition between shapes (B) and (C) changes only the derivative of θ_m and leads to the completely closed spiral. For fixed $\frac{\epsilon^*}{\kappa_c}$ and θ_o a growing filament starts with an open chain configuration, (A). At a certain length, the shape changes to the, for the specific parameters, closest packed spiral, (B) or (C) Fig. 4.3. For further increasing filament length, the spiral opens up and the decreasing value of θ_m is not only due to the growing spiral but also to the decreasing initial curvature, θ_1. The shape diagram for $T = 0$ gives an idea about the parameter ranges of the different configurations. For a real comparison with AFM images, thermal fluctuations have to be added. We have incorporated

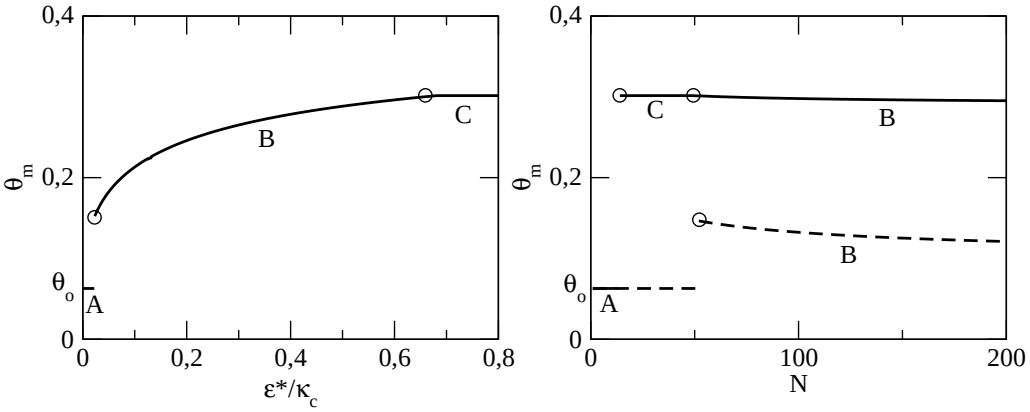

Figure 4.3.: Phase diagram of filament shapes. For fixed spontaneous curvature, $\theta_o = 2\Pi/100$, the mean angle between monomers along the filament is represented as a function of $\frac{\epsilon^*}{\kappa_c}$ and fixed chain length, $N = 50$, and B) (Left) and as a function of N and $\frac{\epsilon^*}{\kappa_c} = 0.68$ (continuous line) and $\frac{\epsilon^*}{\kappa_c} = 0.02$ (dashed line) (Right). A, B and C refers to the different filament shapes shown in Fig. 4.2.

this temperature effect in the Langevin dynamics simulations of FtsZ filaments in Sec. (4.3) but before we estimated the bending properties for short chains without lateral contacts.

4.2. Interpretation of AFM shapes without lateral contacts

We started the analysis of filaments found in the AFM images with chains one to six of Fig. 4.4. In this image, the protein density is very low so that we can distinguish individual filaments. In our model, the shape of these filaments is controlled by their spontaneous curvature, θ_o, and their bending rigidity, κ_c. We will start with a brief summary of the first attempt to determine these two parameters. Later on, while we were analyzing ring conformations, we noticed that this early description was insufficient.

First attempt

1. We reconstructed the curves representing the filaments using a polynomial of the form $R(\varphi) = \sum_{i=0}^{m} B_i \varphi^i$ and determined the $B_i s$ and the center of the coordinate system with the minimum quadratic error method.

2. Between the two extremes of the reconstructed curves, we placed monomers separated by its diameter $d = 4.5nm$.

3. We calculated the angles between monomers making the assumption that a spontaneous curvature exists and defining the mean curvature of each filament to be positive. This assumption may be justified by the fact that all chains show a globally defined positive or negative curvature. These two opposite global curvatures of the filaments might be found because we cannot distinguish between the (+/-) ends of the chain.

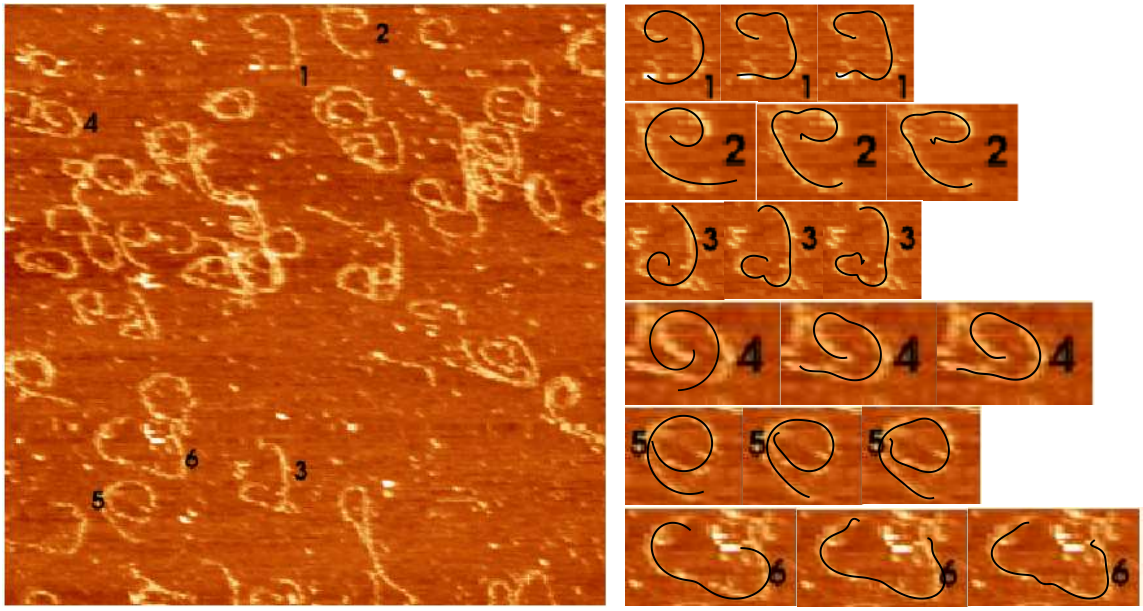

Figure 4.4.: Left: AFM image of FtsZ polymers (size: $3\mu m$ x $3\mu m$) at low density. Right: Zoom of six individual filaments without lateral contacts. Right: superposed reconstructions minimizing a polynomial of degree $m = 5, 10$ and 15 (from left to right).

4. Finally, we could estimate the spontaneous curvature of the filaments, θ_o, as the mean bond angle and the bending rigidity, κ_c, which is related to the mean quadratic deviation of the bond angle through

$$P(\theta) \quad = \quad \sqrt{\frac{\beta\kappa_c}{2\pi}} \exp\left(-\frac{\beta\kappa_c(\theta-\theta_o)^2}{2}\right). \tag{4.10}$$

We used polynomials of degree $m = 15$ to do the reconstructions (see Fig.4.4) and found filament lengths between 145 and 226 monomers:

filament	1	2	3	4	5	6
number of monomers	183	164	184	145	226	203

Fig. 4.5 shows the distribution of the angle between monomers and a Gaussian fit, Eq. (4.10), of this distribution that we obtained by the least squares minimization method. We find $\theta_o = 0.048$ and $\beta\kappa_c = 683$. Due to a calculation error, these values are slightly different to the values presented in [34] but based on the same method. We will continue with the problematics of the above described estimation method that we encountered further on, during the analysis of ring conformations.

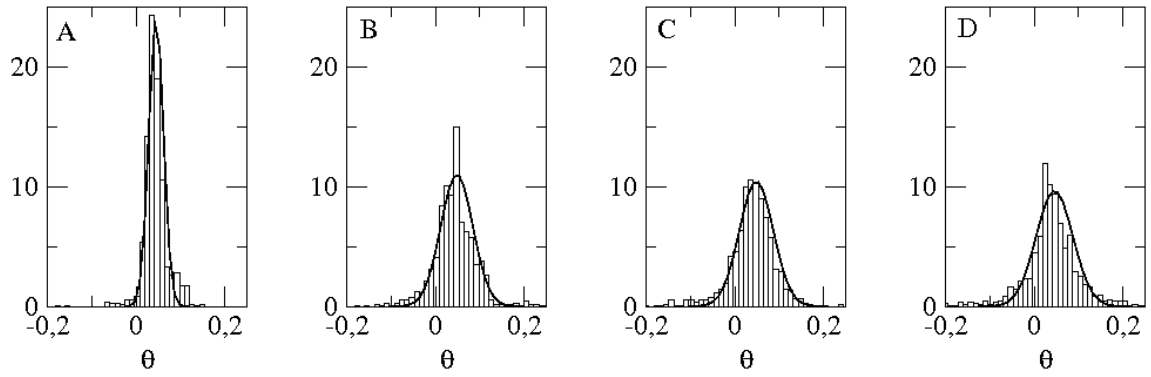

Figure 4.5.: Probability distributions of ≈ 1000 angles reconstructed from filaments 1-6 of Fig. 4.4 minimizing a polynomial of degree A) 5 B) 10 C) 15 and D) 20. The straight lines are least mean squares Gaussian fits of the distributions.

Problematics

At the moment of "reconstruction" of the filament, we artificially add information to the experimental data. The resolution of the AFM images allows to determine the global shape of individual filaments but we do not distinguish individual monomers and we can not "measure" the angles between them. In the above presented estimation, we use this non-existing information about individual bond angles to calculate their fluctuations. In the chapter about ring conformations we will see that the fluctuations in the global shape also allow an estimation of the bending rigidity, but this type of analysis requires a large number of (preferentially ring) filaments. Here we actually control the flexibility of the chain by the degree of the polynomial in the curve reconstruction. Fig. 4.4 shows reconstructions with polynomials of degree $m = 5, 10$ and 15 and Fig. 4.5 the resulting angle distributions. While the spontaneous curvature is almost independent of m, the bending rigidity becomes stiffer for decreasing polynomial degree:

m	5	10	15	20
θ_o	0.045	0.048	0.048	0.046
$\beta\kappa_c$	3645	758	683	583

Approach: Mean values of bond angles

How can we use the experimentally available information about the global shape of the filaments to deduce the bending rigidity of an individual bond? Our next idea consisted in calculating mean values of the angles between the reconstructed monomer positions. The probability distribution of the mean values of n consecutive bonds is

$$P\left(\frac{1}{n}\sum_{i=1}^{n}\theta_i\right) = \sqrt{\frac{n\beta\kappa_c}{2\pi}}\exp\left(-\frac{n\beta\kappa_c\left(\frac{1}{n}\sum_{i=1}^{n}\theta_i-\theta_o\right)^2}{2}\right). \tag{4.11}$$

Here, we assume that consecutive bonds are not correlated. This is true for the bond angles of a filament in the simulation but it is not true for the bond angles of a chain, reconstructed with a polynomial of degree m. Actually, this reconstruction, using a polynomial of degree m, reduces the number of "independent bond angles" by a factor $\frac{m}{N}$ and might be interpreted like averaging over $\frac{m}{N}$ consecutive bonds, giving a coarse grained view of the filament. Before analysing the experimental data, we have checked this assumption with simulation data where we know the actual value of the bending rigidity. We have realized a simulation of a monomer chain of length $N = 50$ with $\beta\kappa_c = 200$ and $\theta_o = \frac{2\pi}{100}$. We have taken snapshots of 100 chain conformations and reconstructed these chains with polynomials of degree $m = 4, 5, 6, 7, 8, 9$ and 10. This should correspond to average over $n = \frac{50}{m}$ consecutive bond angles. The following table shows the results for a least means squares fit of the angle probability distribution to Eq. (4.11) for the above degrees of the reconstruction polynomial.

m	4	5	6	7	8	9	10
n	12.5	10	8.3	7.1	6.3	5.6	5
θ_o	0.063	0.065	0.066	0.067	0.067	0.067	0.067
$\beta\kappa_c$	171	165	218	207	201	204	192

The estimated mean value, $\beta\kappa_c^{est} = 194 \pm 18$, is quite close to the actual value, $\beta\kappa_c = 200$, which is covered by the error. The estimated spontaneous curvature, $\theta_o^{est} = 0.066 \pm 0.001$, is also very close to the actual preferential angle, $\theta_o = 0.063$. Apparently, the estimation of the material parameters works quite well for simulated configurations that we reconstruct as if they were experimental data.

Now we will come back to the set of six experimental filaments. Again, we have reconstructed the filaments with polynomials of the same degrees as the simulated configurations. We approximate the length of the chains by their mean value ($N = 184 \pm 27$) to get the values of n and present the results as above in the following table:

m	4	5	6	7	8	9	10
n	46	37	31	26	23	20	18
θ_o	0.043	0.042	0.041	0.042	0.044	0.042	0.042
$\beta\kappa_c$	85	114	82	76	54	59	62

With this method, for the experimental data we get an estimation of the bending rigidity, $\beta\kappa_c = 76 \pm 19$, and the preferential curvature, $\theta_0 = 0.042 \pm 0.001$. The filaments seem to be 10 times

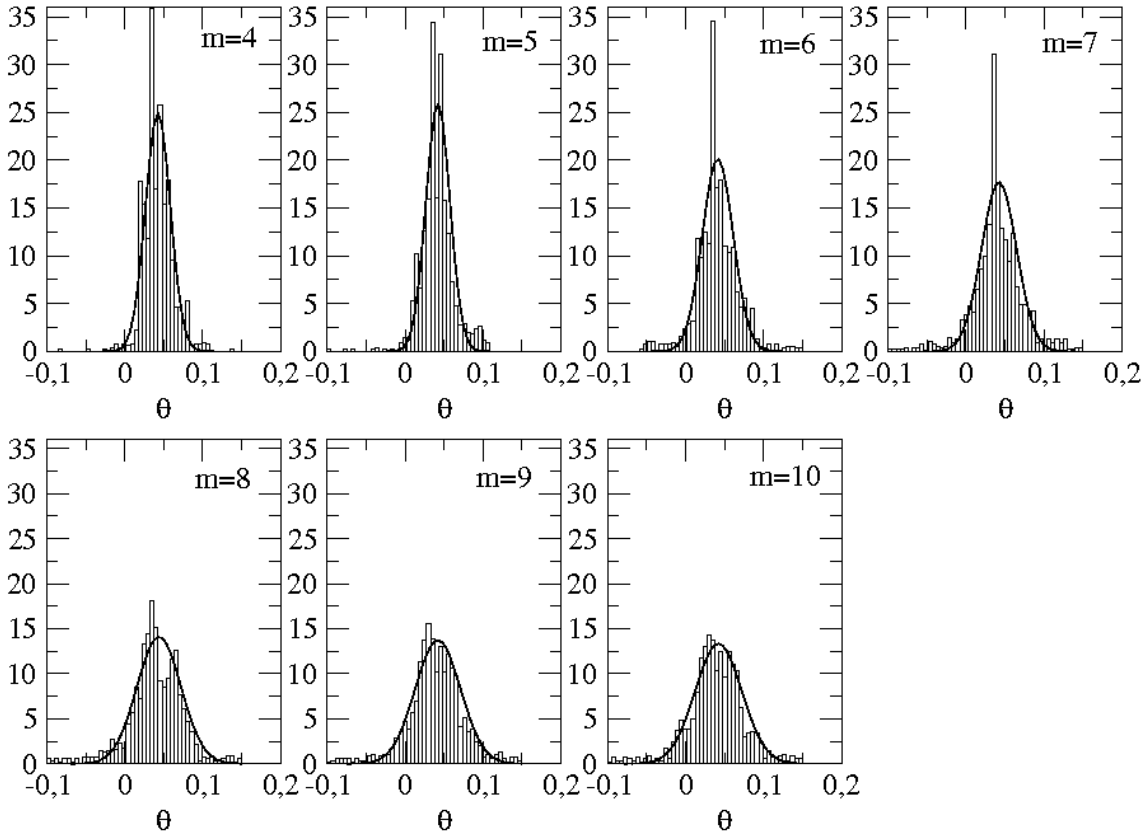

Figure 4.6.: Probability distributions of ≈ 1000 angles reconstructed from filaments 1-6 of Fig. 4.4 minimizing a polynomial of degree 4-10. The straight lines are least mean squares Gaussian fits of the distributions.

more flexible than estimated above! At this point, we should give strong warning of the problems associated to the comparison between model and experiment. The interpretation of often incomplete experimental information has to be done very carefully. A good way to check the validity of the estimations seems to be the "creation" of "experimental" samples in simulations with known parameters and their further analysis using the same tools as for the experiments. With this procedure we can check, whether we can extract the original parameters and also how precise the estimations are. In the next section we will analyse the effect of lateral contacts between filaments.

4.3. AFM shapes with lateral contacts

At higher protein densities, filaments start approaching each other and lateral interactions become important. Fig. 4.7A shows an AFM image with medium protein coverage. Here, long filaments form loops with several turns. The pitch distance, that is the distance between filaments in consecutive turns of a loop depends strongly on the experimental conditions [23]. The high resolution of Fig. 4.7B permits a direct measurement of this distance for the AFM images that we analyse here and gives an estimate of $\sigma^* \approx 12nm$.

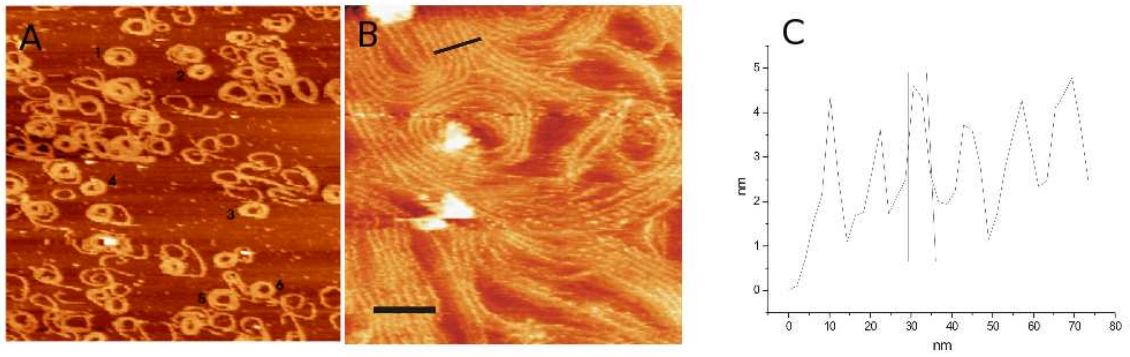

Figure 4.7.: A) AFM image of FtsZ polymers at mean protein density (size: $3\mu m$ x $3\mu m$). B) Zoom into a high resolution AFM image. C) Topography image of the zone marked with a black line in image B) the peak to peak distance between the first and the last filament is $60nm$ resulting in a distance of $\approx 12nm$ between filaments.

We will now estimate the depth of the lateral interaction potential between the filaments shown in Fig. 4.7A in two ways. First analytically and then comparing snapshots of simulations to the experimental configurations.

4.3.1. Analytical estimation of the lateral interaction

We get a rough estimation of the depth of the lateral interaction potential using Eq. (4.9),

$$\frac{\epsilon^*}{\kappa_c} = f(R_o - R_i)\left[\frac{f\sigma^*}{R_i R_o} - \frac{2\theta_o}{R_i + R_o}\right]. \tag{4.12}$$

R_i and R_o are the inner and outer radii of the loop, assuming that these radii correspond to the radius of the first and last monomer respectively. We measured these two values for the filaments marked in Fig. 4.7A. The resolution of the AFM images is not high enough to permit precise measurements so that the errors in R_i and R_o are quite high and therewith all further estimations based on these values as the number of monomers in the filaments, $N = (R_o^2 - R_i^2)\frac{\pi}{f\sigma^{*2}}$. Fig. 4.8 represents the loop revolutions of a filament of $N = 600$ monomers as a function of the force of the lateral interaction using the before estimated value of κ_c. The result is shown for zero spontaneous curvature and for $\theta_0 = 0.042$. In the latter case, the equilibrium configuration is a loop even without lateral interaction and the effect of a growing value of ϵ is that the loop becomes closer. For $\theta_0 = 0$ the lateral interaction is responsible for the formation of the loop configuration. The table below summarizes the results of the estimations done for the six loops marked in Fig. 4.7.
So, this first and very rough estimation gives $\epsilon^* \approx 0.9kT$. The value of ϵ in the Lennard-Jones potential of our simulations should be smaller due to the fact, that one monomer experiences lateral interactions with more than two neighbours. To calculate the value of ϵ in the Lennard-Jones potential that correspond to the value of ϵ^* that we use here, we have to solve the following

	1	2	3	4	5	6
R_{in} [nm]	45	30	40	40	50	50
R_{out} [nm]	105	85	85	85	95	85
N	520	370	330	330	380	270
$\epsilon^*[kT]$	0.7	1.7	0.9	0.9	0.5	0.5

equation:

$$\begin{aligned} U_{lat} &= U_{LJ} \\ \epsilon^* &= \sum_i 4\epsilon \left[\left(\frac{\sigma}{d(i)} \right)^{12} - \left(\frac{\sigma}{d(i)} \right)^{6} \right], \end{aligned} \tag{4.13}$$

with i counting all the neighbours that one monomer has in a neighbouring filament and $d(i)$ being the corresponding distance. As a result, we get: $\epsilon \approx \frac{\epsilon^*}{4}$. Here we still have not counted the neighbours that one monomer may have in a second neighbour filament, but the additional reduction that we would get here does not change the result significantly.

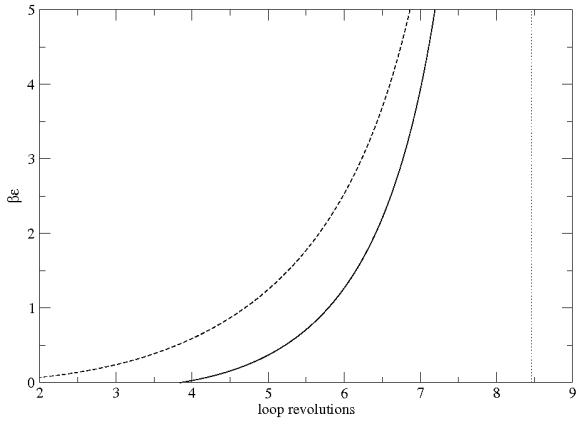

Figure 4.8.: Loop revolutions of a filament of $N = 600$ monomers as a function of the force of the lateral interaction with $\beta\kappa_c = 80$ and $\theta_0 = 0$ (dashed line) and $\theta_0 = 0.042$ (continuous line). The vertical line represents the limit $R_i = 0$.

4.3.2. Simulation of chains with lateral interaction

We have realized LD simulations of filaments including the lateral interaction potential described in Chp. 3. The purpose here was to remain as close as possible to the experimental conditions. Mimicking the FtsZ filaments anchored to the mica surface and in equilibrium with a bath of the protein solution we can think of the following scenario: Monomers and short filaments attach to the membrane (and return to the solution). Filaments then start growing on the mica. During

the growth process a loop may be formed. Actually, especially the experiments that we analyse here, were done at a protein concentration above the critical polymerization in bulk, so that polymers formed already in solution. Still, the first images show single, unlooped filaments and the simplified picture of one by one growth on mica should not alter the final aspect of the spirals and may even allow the determination of some qualitative aspects of the growth process. We started the simulations with an initially very short filament of only 5 monomers. Every 10^6 time steps, we added a single monomer to the existing chain, simulating in a simplified way the growth of the filament. The formation of a first lateral contact in these simulations took place for filament lengths of about 150-250 monomers. We continued the growth process until reaching a total number of 600 monomers.

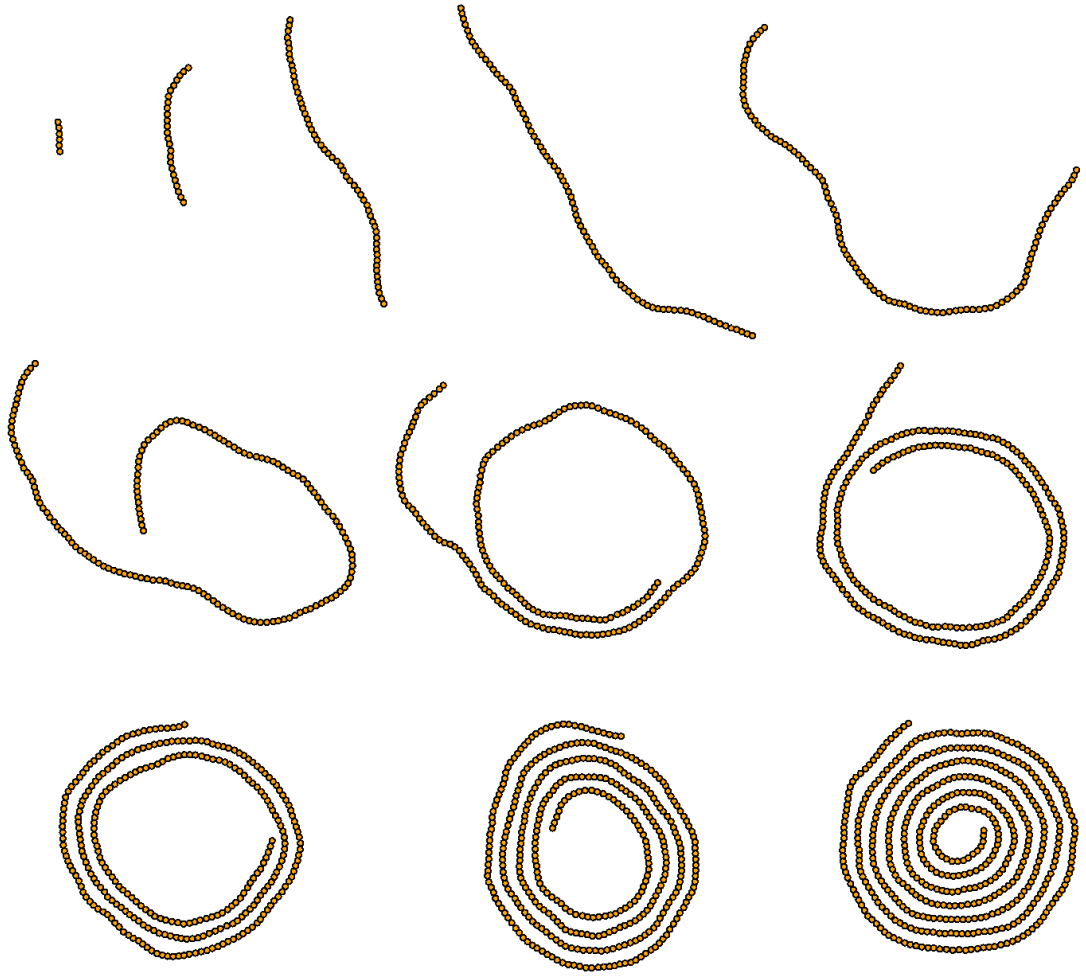

Figure 4.9.: Snapshots of a growing filament in an LD simulation with $\beta\kappa_c = 80, \beta\epsilon = 0.2, \theta_0 = 0.042$ The initial configuration was a five monomers long chain, each 10^6 time steps one monomer was added to the inner extreme of the filament, so that the spiral grew inwards. The last chain consists of 600 monomers.

In the first simulations, the filament growth only took place at one extreme of the filament. Filaments, that built up their first lateral contacts with the growing extreme inside (Fig. 4.9, started growing inside the loop and the loop started getting closer and closer as the time between monomer insertion was not long enough to allow for an equilibration of the filament once lateral contacts had been established. Filaments that built up their first lateral contact with the growing extreme on the outside of the loop kept on growing outside (Fig. 4.10) and ended up in loops with a much bigger "hole" in the center. Both of these loops should end up in similar loops with a constant relation between the inner and the outer radii depending only on $\frac{\epsilon}{\kappa}$ and θ_o. Actually this equilibration process is very slow (Fig. 4.12). In a previous study, where we estimated a bending rigidity, $\kappa_c = 890$, we got the best qualitative agreement between the spirals found in the simulations and the spirals found in the AFM images for $\epsilon \approx 2kT$ [34]. After the correction of κ_c to a value about ten times smaller, we also reduced ϵ by the same factor and again found good agreement between simulation and experimental shapes for $\epsilon \approx 0.2kT$. This value is also compatible with the analytical estimation, $\epsilon^* = 0.9$ and $\epsilon \simeq \frac{\epsilon^*}{4}$. All simulations done with the above estimated parameters ($\beta\kappa_c = 80, \theta_o = 0.042, \beta\epsilon = 0.2$) ended up in spiral configurations.

This evolution is mainly due to the preferred bond angle θ_o, which favours a first contact with parallel topology. Without the effect of a preferential curvature, the fluctuations of initially straight chains may produce first contacts with anti-parallel topology which rapidly evolve into hairpin configurations where the two halves of the chain are paired. Such structures are shorter and more rigid than the initially unfolded chain, so that its fluctuations would be much weaker and the chance to establish further lateral contacts may be very small. Therefore, these hairpin states are easily formed and have very long life times although they do not optimize the lateral contacts and represent metastable states with respect to the spiral configurations. We have done some exploratory simulations for chains without preferential angle and found evolutions into spiral as well as hairpin configurations. The existence of a preferential angle θ_o favours the formation of the spiral contacts, avoiding the trap of the hairpin structures. The absence of hairpin structures and straight chains in the AFM images gives support to the existence of a spontaneous curvature of FtsZ filaments.

During the formation of spirals in the simulations we could observe a great variety of intermediate states. Here, we only present two extreme cases, where the spirals grow inwards or outwards whereas growth in both directions is possible and the two growth rates depend primarily on the availability of protein. In Fig. 4.7 we can also observe very diverse spiral shapes. Highly condensed spirals, more open configurations and loops, where at some points lateral contacts are not (yet) established (Fig. 4.11). All these different shapes are also found during the simulation of growing filaments. This indicates, that the AFM images may be interpreted as snapshots taken during the growth process rather than an equilibrium state. Fig. 4.12 illustrates the very slow equilibration process of established spirals. Actually, the difference between the energy per monomer in "open" and "closed" configurations is much smaller than the thermal fluctuations.

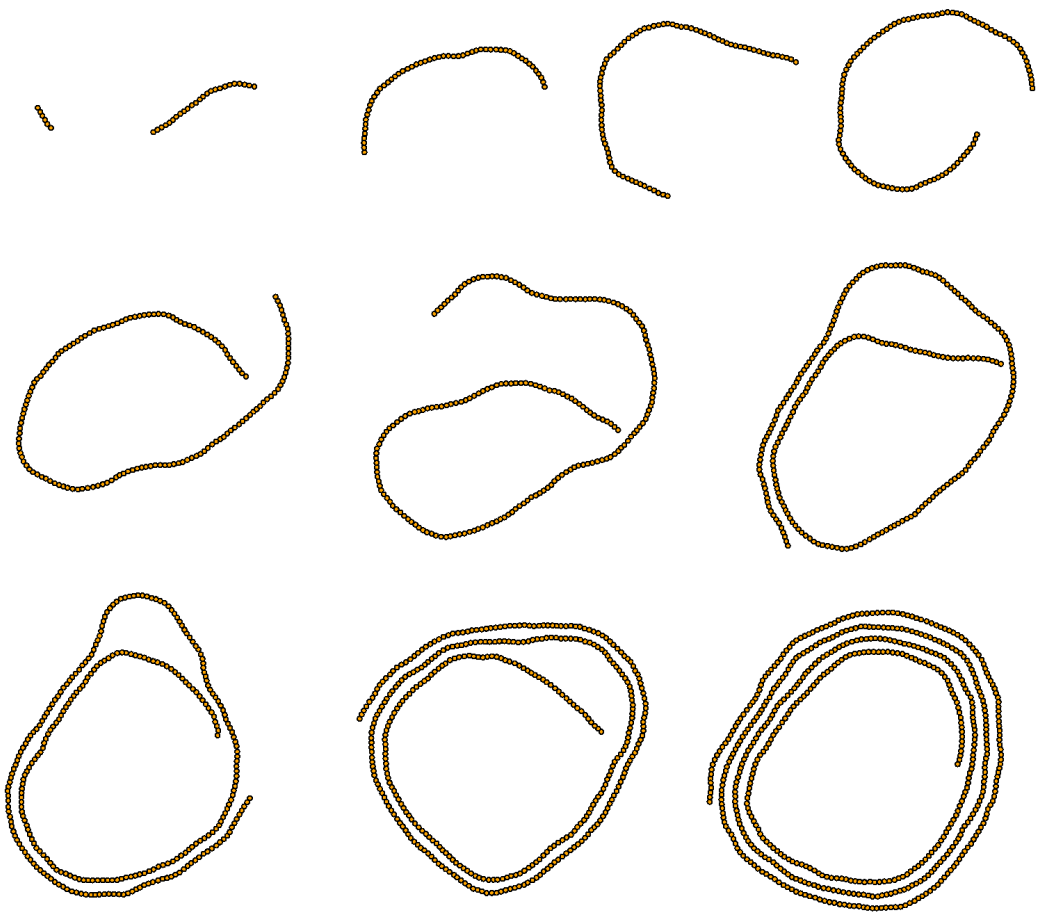

Figure 4.10.: Snapshots of a growing filament in an LD simulation with $\beta\kappa_c = 80, \beta\epsilon = 0.2, \theta_o = 0.042$ The initial configuration was a five monomers long chain, each 10^6 time steps one monomer was added to the outer extreme of the filament, so that the spiral grew outwards. The last chain consists of 600 monomers.

4.4. Conclusions

In the first part of our work we have estimated the model parameters for monomer-monomer interactions in FtsZ filaments formed on mica surface in the presence of GDP-AlF_3. We started with the analysis of short filaments, without lateral contacts and estimated the bending parameters, κ_c and θ_o. For longer chains, we estimated the strength of the lateral attraction comparing the shapes obtained in LD simulations and experiments and we extracted the optimal distance between filaments directly from the AFM images. We can now give values to the parameters defined in Tbl. 3.1 for the specific experimental conditions of the filaments analysed in this chapter.

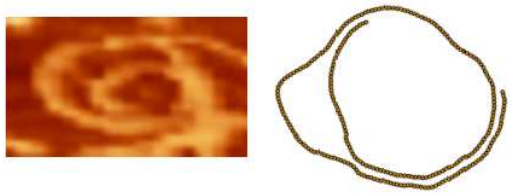

Figure 4.11.: Spiral configuration where not all of the possible lateral contacts are established.

covalent bond		curvature		lateral interaction	
d	4.5 nm	θ_o	0.042	σ	12 nm
κ_b	200 kT	κ_c	80 kT	ϵ	0.2 kT

Using a simple model for FtsZ filaments describing the monomers as coarse grained beads in a chain and their effective interactions with a minimum number of parameters, we were able to explain and reproduce the global shapes observed in AFM images of FtsZ with GDP-AlF_3. We can calculate the persistence length of FtsZ filaments, $L_p = \beta\kappa_c d \approx 400nm$ and compare it to the values estimated for microtubules and actin filaments. It is about one thousand times smaller than for microtubules which have a persistence length of a few millimeters [26, 27, 35] and still about 50 times smaller than the persistence length of actin filaments with $L_p \approx 18\mu m$ [26, 36]. FtsZ filaments are half way between perfectly stiff chains and random polymers with typical lengths in the order of the persistence length, $N \approx \beta\kappa$. Lateral attractions are important and take influence on the shape of long filaments or filament bundles. The finale conformation is the result of a fine balance between the optimization of lateral contacts and the cost for bending and is very sensitive to the environmental conditions. This fine tuning might be crucial for the biological role of FtsZ filaments during the cell division process.

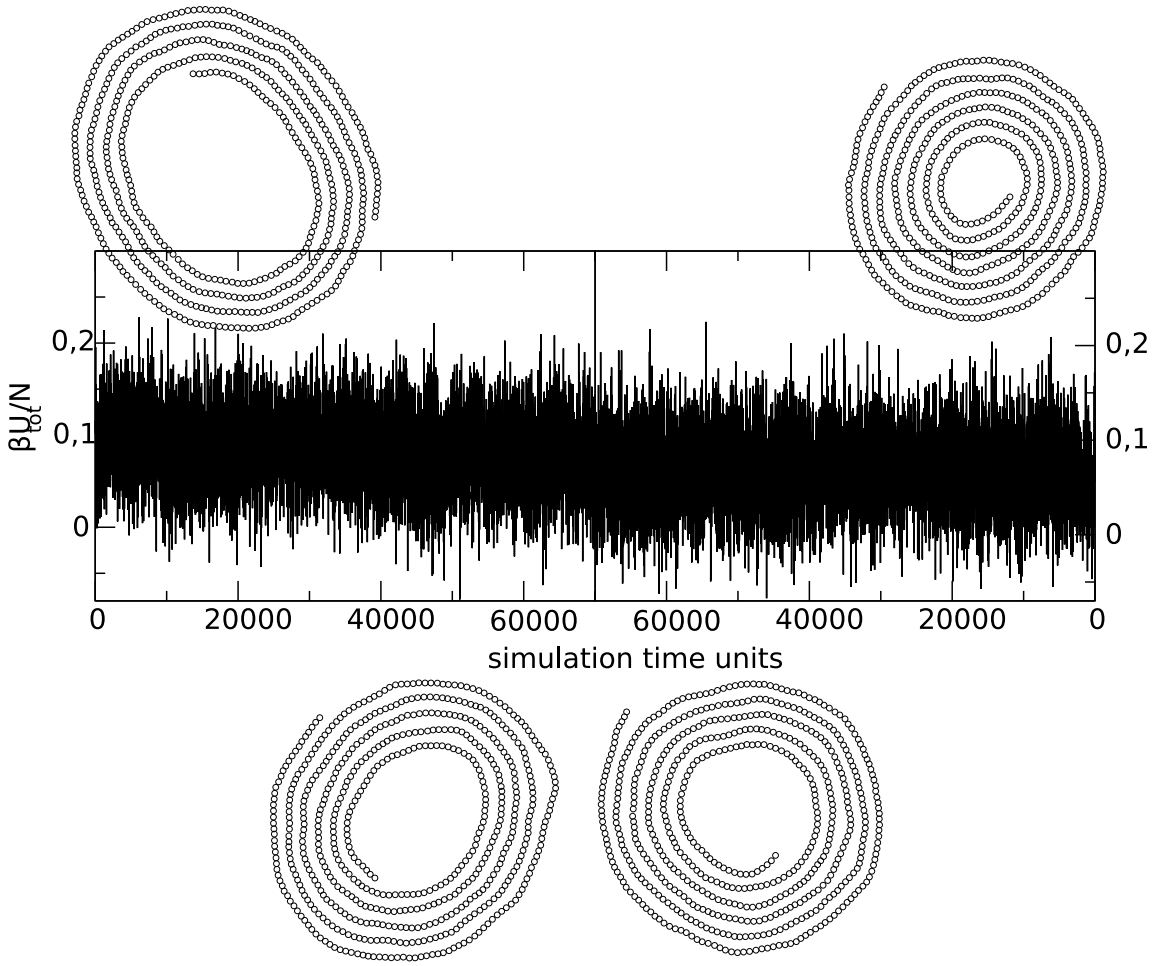

Figure 4.12.: Simulation of the opening (from left to right) and closing (from right to left) process of loops with $N = 600$, $\beta\kappa_c = 80$, $\beta\epsilon = 0.2$ and $\theta_o = 0.042$. Spirals with initially 4 (opening) or 6.5 (closing) turns end up in the equilibrium shape with ≈ 5 loop turns.

5. Filaments on cylindrical surfaces

So far, we have described simulations of two-dimensional growth and diffusion processes of filaments on a flat surface since the experimental data to fit our model energy came from the behavior of the filaments on mica. The access to experimental data of the more interesting cylindrical *in vivo* geometry is much more complicated but, at least in a qualitative way, we can extrapolate the behavior of the filaments on mica to the altered conditions. Previous models [37, 38] have assumed that the formation of the septal ring in bacteria was driven by a specific off-plane spontaneous curvature of the FtsZ filaments that tends to align them on a plane perpendicular to the long (cylindrical) axis. Here, we explore the effect of the lateral attraction to stabilize ring-like structures which are qualitatively different from the compact spiral shapes formed on a plane. Such spiral forms are also possible on a cylindrical substrate and compete with the helical rings. Within the simulations of a long single filament the formation of one or other type of aggregate depends on how the first lateral contact is made. Quantitative estimations are more complicated as, from the AFM experiments, we do not have access to the bending coefficients away from the planar conformations. In this chapter, we will first treat simulations of filaments forming a helix in cylindrical geometry with the simplest possible extrapolation of the model developed for filaments on mica. Then we will analyze the possible effects of the off-plane spontaneous curvature of the filaments. We end with some remarks on the competition between helical and spiral shapes and on the possible role of the rings in the process of force generation required for the constriction of the membrane.

5.1. Simulation of filaments on a cylindrical surface

The simplest way to simulate filaments attached to the inner bacterial membrane is to remain in two dimensions and to apply periodic boundary conditions in one of the two directions to introduce lateral interactions between filaments (Fig. 5.1). The radius of the bacterial membrane is about $0.5\mu m$, so that ≈ 700 monomers are needed to complete one turn around the cylinder. Prior to cell division, ≈ 10000 FtsZ monomers are present in the cytoplasm (in *E. Coli*) and $\approx 30\%$ of them are concentrated at midcell. The force ring therefore may be made up of a maximum of 5 turns. Actually, the ring consists of several shorter, individual filaments in lateral contact with each other [39]. In our simulations, we have used a variety of simplifications. We have reduced the radius of the cylinder (R_c) and the number of FtsZ monomers to get reasonable simulation times. We started the simulations with a short, 5 monomer long filament and simulated its growth, as before, up to a length of about five times the perimeter of the cylinder with $p_{cyl} = 2\pi R_c$. Instead of a series of short filaments we assume one long filament. Once the ring around the cylinder has been formed, we could not assert a significant difference between simulating one long filament

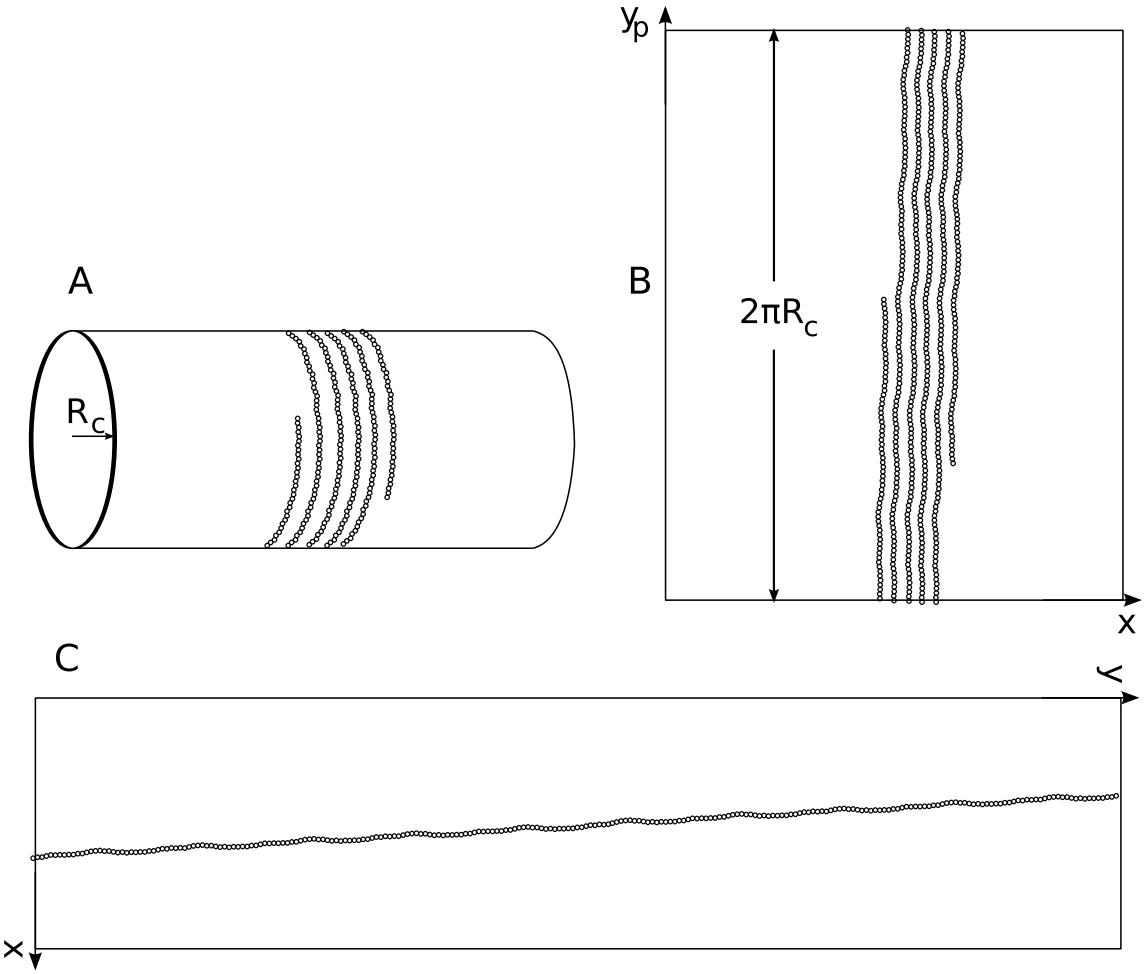

Figure 5.1.: A) Schematic illustration of a filament on a cylindrical surface. B) Unfolding the cylinder: two dimensional view of the filament in periodic coordinates (x, y_p). Lateral interaction between filaments are calculated in these coordinates. C) Two dimensional view of the filament in coordinates (x, y). In theses coordinates we calculate interactions between direct neighbours along the chain.

and several short chains. This difference might show up at the time of formation of the septal ring and further on we will shortly discuss different possible mechanisms that favor the formation of rings in place of loop shapes. The mechanism that we have used in the simulation consists in switching off the preferential on-plane curvature. We did the simulations in two steps, growth of the filament and formation of the ring around the cylinder was followed by an estimation of the constriction force generated by the force ring.

5.1.1. Filament growth and ring formation

Starting with a 5 monomer long filament, we added one monomer each 10 simulation time units until reaching a length of 150 monomers. In that way, during the growth process (or after it) the filaments typically started forming a helix around the cylinder. Fig. 5.3 shows the total energy

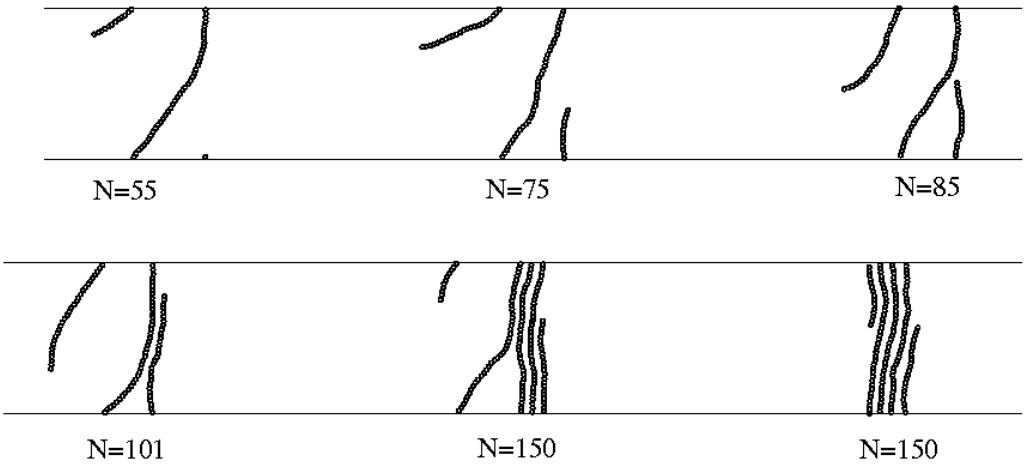

Figure 5.2.: Illustration of the process of filament growth and helix formation on a cylindrical surface. A view of the unfolded cylinder is represented. For $N \approx 85$ the first lateral contacts are formed.

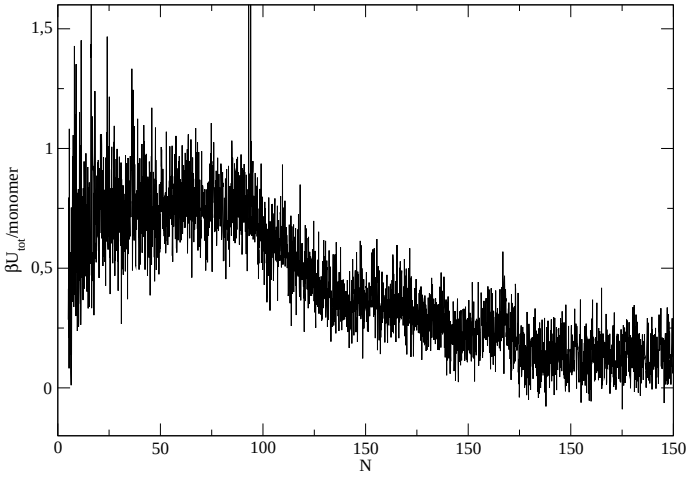

Figure 5.3: Total energy per monomer during filament growth and helix formation on a cylindrical surface. For $N \approx 85$ the first lateral contacts are formed and U_{tot} decreases abruptly until a closed packed helix is formed.

per monomer during a specific growth process of a filament. The sudden decrease of U_{tot} when the filament reaches a length of $N \approx 85$ coincides with the first lateral contact in between the filament (Fig. 5.2). Here the filament keeps on growing at the "free" end, so that the final close packed helix is reached about 1600 simulation time units later. Fig. 5.2 illustrates the growth of the filament and the formation of the helix around the cylinder representing an unfolded view of the cylinder.

5.1.2. Contractile force

The effect of the lateral attraction in a ring supported by an elastic wall is qualitatively different from its effect in planar loops where the radius is determined by a balance between the lateral interaction gain and the cost for bending the filament. Here we should account for several aspects:

- The on-plane cost for bending is fixed for ring shapes where the average yaw angle between

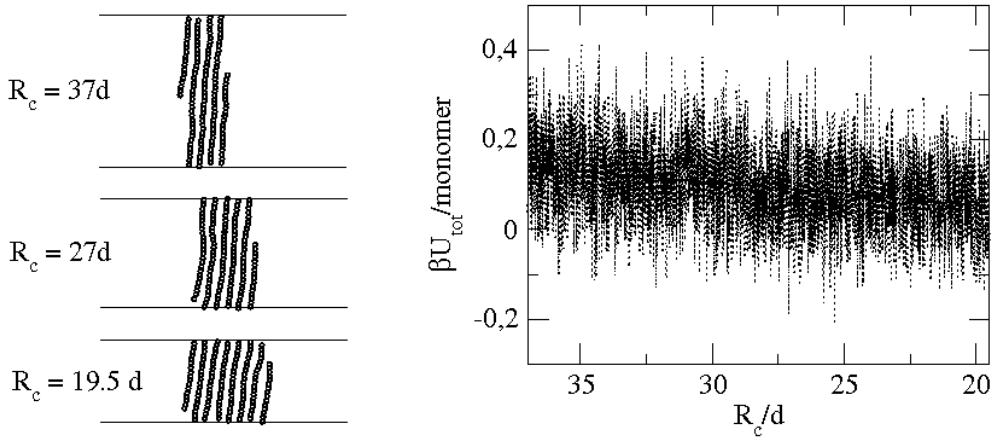

Figure 5.4.: Left: Illustration of the reduction of the cylindrical radius. Right: Total energy per monomer while the radius of the cylinder is reduced from initially $37d$ down to $19.5d$. U_{tot} decreases linearly indicating that the Z-ring generates a constant constriction force.

monomers is zero.

- An additional bending direction, perpendicular to the plane of the cylinder appears. For preferential curvatures bigger than the inverse of the radius of the ring, bending tends to reduce this ring radius. It tends to augment it for preferential curvatures lower than $\frac{1}{R_c}$.
- Lateral interactions are in all cases optimized by a reduction of the ring radius.
- The supporting bacterial membrane works against the reduction of the ring radius.

Due to the presence of the membrane, the ring can not simply adopt its equilibrium radius and instead of that it generates a force that generally tends to decrease the membrane radius. In the second part of this work, we will study the reaction of the membrane upon the application of this constriction force. The constriction force is composed by a bending part and by a lateral interaction part. Experimental data about preferential curvatures off-plane are still converse and we will concentrate here on the estimation of the force generated by optimizing the lateral contacts. In the simulation, we calculated the total energy per monomer for the helices formed in the first part of the simulation. Then we started shrinking the radius of the cylinder at a reduction rate that assures the equilibration of the filament along the process. Fig. 5.4 illustrates the reduction of the cylindrical radius and the reorganization of the filament. It also shows the total energy per monomer as a function of R_c. U_{tot} decreases linearly with the radius of the cylinder and we can roughly estimate the constriction force, $f_R = -\frac{\delta U_{tot}}{\delta R_c} \approx 4pN$. The table below gives a short summary of the whole simulation.

Although we did the simulations with reduced cylindrical radius and a reduced number of monomers the estimated force should not be very different from the value we would get from a simulation with more realistic values. The force is independent of the radius and, for more than two helical turns, also of the number of monomers. Lateral contacts can only be optimized at the extremes, the contribution of the center of the helix is negligible and the number of helical

Initial configuration	5 monomers
Final length	150 monomers
Growth rate	1 monomer / 10 simulation time units (stu)
First lateral contact	85 monomers
Time between first lateral contact and final helix	1600 stu
Initial radius of the cylinder	$\frac{37}{2\pi}d$
Final radius of the cylinder	$\frac{19.5}{2\pi}d$
Reduction rate	$\frac{0.005}{2\pi}d$ / stu
f_r	$\approx 4pN$

turns does not take influence on the generated force. In these simulations, we took advantage of switching off any spontaneous curvature as one possible way to achieve that the filament adopts a ring conformation (for further mechanisms see 5.3). In the next section we will discuss the dependence between the filament shape and the mechanical properties of the chain.

5.2. Shapes of filaments with off- and on-plane spontaneous curvatures

The mechanical properties of a filament on a cylindrical surface include three different curvature modes. To represent these modes, we introduce the three angles represented in Fig. 5.5. The yaw curvature, α_φ, is the same as θ in our simulations, describing the curvature of the filament on the plane of the cylinder. The pitch curvature, α_θ, is taken perpendicular to α_φ and finally, the roll curvature, α_ψ, describes the internal twist of the polymer. Constrained to a cylindrical surface these three angles are not independent and we will use the following, continuous parametrization:

$$\begin{aligned} \alpha_\phi &= \alpha \\ \alpha_\theta &= -\frac{\sin^2 b}{R_c} \\ \alpha_\psi &= \frac{\sin b \cos b}{R_c}. \end{aligned} \tag{5.1}$$

Now, α is the curvature on the flat plane and b is the absolute direction on this plane. $b = 0$ means that the filament is parallel to the axis of the cylinder. We can then express the total internal energy density of the filament, $\omega(s)$ for the ideal case without any lateral interactions,

$$\omega(s) = \frac{\kappa_\varphi}{2}\left[\alpha_\varphi(s) - \alpha_\varphi^0\right]^2 + \frac{\kappa_\theta}{2}\left[\alpha_\theta(s) - \alpha_\theta^0\right]^2 + \frac{\kappa_\psi}{2}\left[\alpha_\psi(s) - \alpha_\psi^0\right]^2, \tag{5.2}$$

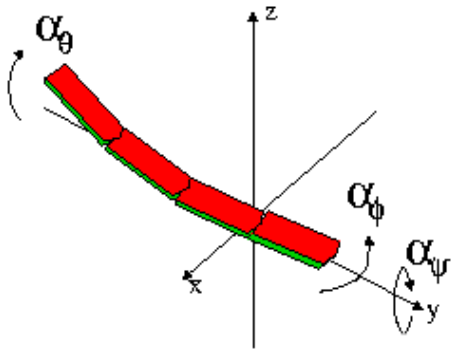

Figure 5.5: Definitions of the yaw, pitch and roll curvatures, α_φ, α_θ and α_ψ.

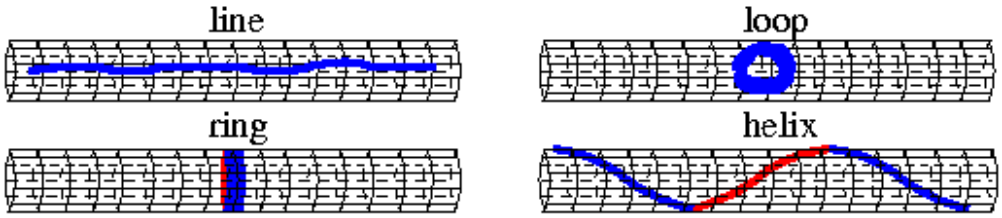

Figure 5.6.: Sketch of the optimal configurations of a filament anchored to a cylindrical surface: line, ring, loop and helix

where s is the path length and l is the length of one monomer. Andrews and Arkin [40] analyzed how the shape that adopts a filament constrained to a cylindrical surface depends on the bending rigidities and spontaneous curvatures. Four, qualitatively different structures can be distinguished (5.6). These are lines parallel to the cylinder axis, loops or rolls on the plane of the cylinder, tight rings around the cylinder and perpendicular to its axis and left- or right-handed helices of variable pitches that enclose the cylinder. The whole spectrum is already found for the simple case of equal bending rigidity in all three angular directions. Loops only appear for non-vanishing spontaneous yaw curvature. For $\varphi_o = 0$ the shape is defined by the value of b that minimizes Eq. (5.2), b_m. For symmetry reasons, b_m must be constant along the filament. The table below summarizes the chain conformations for $\kappa_\varphi = \kappa_\theta$.

For $\kappa_\varphi \neq \kappa_\theta$ the energy spectrum changes and possibly two minima appear [40] so that two instead of one stable polymer conformations would result. For $\alpha_\varphi^0 \neq 0$ a loop region emerges for low values of the remaining preferential curvatures. Fig. 5.7A shows the shape diagram for $\varphi_o = 0.042$ and $\kappa_\varphi = \kappa_\varphi = \kappa_\theta$ in the $\theta_o - \psi_o$ plane. In this purely mechanical model, the biologically relevant ring region is restricted to the sparse line region, $\psi_o = 0$. For any spontaneous roll curvature of the polymer, helical shapes completely replace rings. The experimental evidence of lateral attraction between FtsZ filaments changes this shape diagram and reduces the restrictions on spontaneous curvatures that allow the formation of rings around the cylinder [41].

α_θ^0	α_ψ^0	b_m	shape
$> -\frac{1}{2R_c}$	0	0	line
$\leq -\frac{1}{2R_c}$	0	$\frac{\pi}{2}$	ring
$-\frac{1}{2R_c}$	$> / < 0$	$\frac{\pi}{4}$ / $\frac{3\pi}{4}$	left-/ right-handed helix
$> -\frac{1}{2R_c}$	$> / < 0$	$0.5 \arctan\left(\frac{\alpha_\theta^0}{\alpha_\theta^0 + 1/(2R_c)}\right)$	left-/ right-handed helix
$\leq -\frac{1}{2R_c}$	$> / < 0$	$0.5 \arctan\left(\frac{\alpha_\theta^0}{\alpha_\theta^0 + 1/(2R_c)}\right) + \frac{\pi}{2}$	left-/ right-handed helix

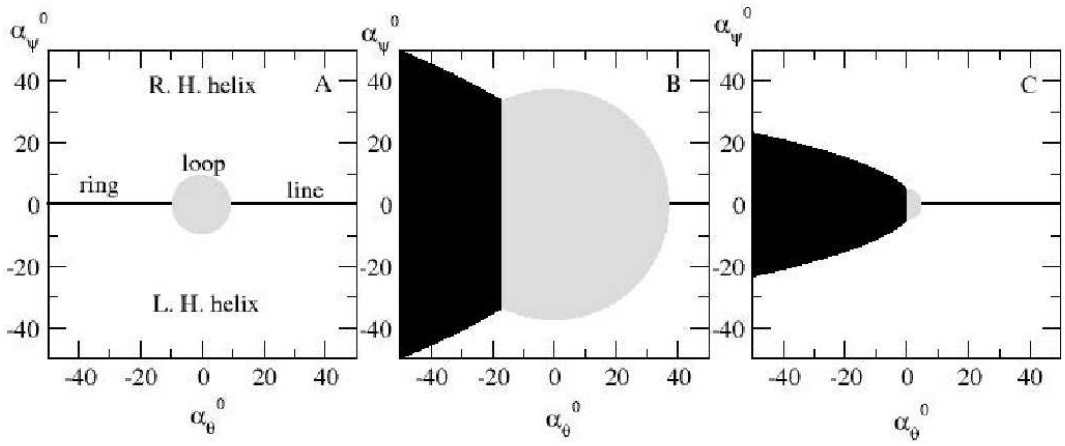

Figure 5.7.: Shape diagram for filaments with 2000 FtsZ monomers anchored to a cylindrical surface with radius $R_c = 500nm$. The optimal configurations, line, helix, loop and ring are found in different regions of the $(\alpha_\theta^0, \alpha_\psi^0)$ plane. The bending rigidity in all directions is $\beta\kappa_c = 80$. A) $\alpha_\phi^0 = 0.042$, $\beta\epsilon = 0$. B) $\alpha_\phi^0 = 0.042$, $\beta\epsilon = 0.2$. C) $\alpha_\phi^0 = 0$, $\beta\epsilon = 0.05$.

Polymer shapes with lateral attraction

Including the effect of lateral attraction between filaments, the energy density takes on the following form:

$$\omega(s) = \frac{\kappa_\varphi}{2}\left[\alpha_\varphi(s) - \alpha_\varphi^0\right]^2 + \frac{\kappa_\theta}{2}\left[\alpha_\theta(s) - \alpha_\theta^0\right]^2 + \frac{\kappa_\psi}{2}\left[\alpha_\psi(s) - \alpha_\psi^0\right]^2 + N_n\frac{l}{2s}\epsilon^*. \qquad (5.3)$$

ϵ^* is the average lateral interaction potential between one monomer and its neighbour filament and N_n is the number of neighbour filaments which can take the values 0, 1 or 2. Both configurations with lateral contacts along the filament, rolls and rings, gain importance compared to line and helix conformations. To determine the shape diagrams for fixed preferential curvature, $\varphi_o = 0$, we numerically calculated the energy along the filament for each of the conformations on the $(\alpha_\theta^0, \alpha_\psi^0)$ plane. In Fig. 5.7B we have used the values for κ_φ, φ_o and ϵ^* that we extracted from experimental AFM images in Chp. 4 and a 2000 monomer long filament on a cylindrical mem-

brane with the radius $R_c = 500nm$ of *E. Coli*. The qualitative change between the shape diagrams including or not the experimentally evident lateral attraction in FtsZ filaments is obvious. The ring conformation becomes stable with respect to the open helix within a large parabolic region over the unknown parameters α_θ^0 and α_ψ^0, so that a strict spontaneous roll curvature, $\psi_o = 0$, can no longer be hold as a condition for the appearance of FtsZ rings in bacteria.

Our experimental data come from the analysis of individual filaments. Several proteins, that interact with FtsZ and excluded volume conditions are known to induce filament bundling [24, 42]. This may have two effects: braiding of individual filaments could suppress a global preferential curvature of the bundle and the effective strength of the lateral interactions between bundles would be reduced. *In vivo* visualization of the Z-ring indicates that the ring is made up of a multitude of individual filaments rather than one long chain [39]. Entropy gain favours anti-parallel alignments and results in a cancelling of the preferential curvatures of the individual polymers [43]. Fig. 5.7C explores the assumption that the lateral attractions are reduced to a 4th of the observed value on mica and the spontaneous curvature is suppressed. The loop region almost disappears leaving only helices and rings which are the predominant structures observed *in vivo*. The presence of lateral interactions has strong implications, being in accordance with the fact, that ring structures are energetically much more favorable than one could expect accounting only for the bending properties of the filaments. Still, the presence of lateral interactions favours not only ring but also roll structures. These roll structures have not been observed *in vivo*. As we have seen, suppression of the spontaneous yaw curvature is one of the possible mechanisms that conduce to the formation of rings instead of rolls. In the last section of this chapter we will shortly mention two further, biologically relevant mechanisms.

5.3. Preferential nucleation of rings versus rolls

In the simulations of filaments on a cylindrical surface, we could confirm the predictions of the shape diagram where a direct transfer of the bending and lateral interaction parameters estimated for polymers on mica, conduce to the formation of spirals rather than rings. Actually, in these simulations, the filaments do not "feel" the cylindrical shape of the substrate apart from the periodic boundary conditions. No off-plane curvatures were included in the calculations. In parallel to the Langevin dynamics simulations of FtsZ protein filaments a different approach, consisting in Monte Carlo simulations on a two dimensional triangular lattice model has been done in our group [43, 44]. Within this description, the formation of rolls instead of rings could be confirmed for a direct transfer of the planar lattice model parameters to a cylindrical geometry. In addition to the condensation effects of lateral attractions that support both - rings and rolls a further push that gives advantage to the preferential nucleation of rings versus rolls is required. Three different conditions have been explored using the above mentioned lattice model [44].

Elimination of the on-plane preferential curvature

As in the Langevin dynamics simulations, the elimination of the on-plane preferential curvature promoted the formation of rings around the cylinder. The on-plane spontaneous curvature observed for FtsZ filaments on mica can be easily canceled through the formation of bundles of

filaments with mixed orientations [43] under any bundling promoting conditions [24, 45, 46, 47].

Addition of an off-plane preferential curvature

Ring formation is also induced when a preferential off-plane curvature is added while keeping the on-plane curvature. Although there are no experimental data available to quantify this off-plane energy, its effects have been explored in the lattice model. A small, 2% modification of the energy for bonds formed perpendicular compared to parallel to the cylindrical axis while keeping the on-plane curvature was enough to overcome the tendency of the filaments to form rolls and drove them to form ring condensates.

Enhanced lateral attraction at the center of the cylinder

The effect of lowering the longitudinal bond energy in a narrow cylindrical segment can be associated to the role played *in vivo* by MinC. The presence of MinC reduces the typical filament length [48] in the cell regions where the ring is not formed. Longer FtsZ filaments migrate to the MinC-free region at the center of the cylinder where the FtsZ coverage becomes very large. The influence of the MinC system was introduced in the lattice model by an only 2.5% reduction of the bond energy outside the central part of the cylinder, with the energy parameters obtained for FtsZ on mica and without any off-plane spontaneous curvature. Again a preferential nucleation of rings instead of rolls could be observed.

During the bacterial cell cycle a reliable and precise control of FtsZ filament condensation and ring formation is essential. The apparent sensibility of the filament shape on minor modifications of the energy parameters and the active monomer exchange due to GTP-controlled polymerization may be related to the biological role of the protein. In this picture, subtle bio-chemical signals are able to drive Z-ring formation at the correct place and time of the cell cycle.

5.4. Conclusions

We have done simulations of growing FtsZ filaments on a cylindrical surface. Filaments started to form rings around the cylinder after reaching lengths longer than the perimeter of the cylinder. In polymers with spontaneous on-plane curvatures these ring structures compete with spirals that form on the cylindrical surface, equal to the structures that we find in two dimensional AFM images. Nevertheless, several mechanisms favor the formation of rings versus spirals and in the simulation we applied one of them suppressing the on-plane spontaneous curvature. Although fluorescent microscopy images supported the idea that the Z-ring is a single continuous structure [49, 50], recent cryoelectron tomography showed a discontinuous Z-ring, made up of many short ($\approx 100nm$ long) individual filaments [39]. In the simulations, once the ring was formed, we could not detect a notable difference in the global shape of a ring made up of a long, single filament or several short ones. In contrast to spiral structures, where the final shape is determined by a balance between curvature energy and lateral attraction, the shape of ring structures is fixed by the cylindrical support. In this case, an optimization of lateral contacts can be reached by a

reduction of the cylindrical radius so that the Z-ring generates a radial force. We calculated this force in the simulations and again found negligible differences between a long, single filament and several shorter ones. The estimated radial force, $f_r \approx 4pN$, is small but in the range of typical forces created by biological motors [51] and might constitute only part of the force generated by the Z-ring. In recent years, several models for force generating mechanisms have been proposed, based on either lateral interaction [34, 41, 52, 53] or spontaneous curvature effects [37, 38], but the essential mechanisms responsible for cell division are still unclear [3]. Still, the importance of lateral attraction is supported by experiments with FtsZ mutations, affecting the surface involved in lateral interactions, that did not support cell division [54].

The existence of lateral attraction between FtsZ filaments is further crucial for the appearance of rings on cylindrical surfaces [41]. Without this condensing effect, helical shapes would be predominant for a wide range of bending parameters and spontaneous curvatures of the protein chains [40], although the biological role of FtsZ underlines the importance of ring formation.

6. Phenomenology of ring conformations

During the realization of this PhD thesis, AFM experiments under different experimental conditions gave as the opportunity for the study of different aspects of FtsZ filament shapes and dynamics. In the first AFM images of FtsZ with GDP-AlF_3, we analysed the shape of polymers formed in the bulk and stabilized on mica by inhibiting nucleotide exchange. We estimated the bending properties and the force of the lateral interaction under these conditions. The motivation for a new set of experiments was the study of the characteristics of bonds under different polymerization conditions. The filaments that we will analyse in this chapter polymerized on the surface as described in Chp. 3. The process provided "clean" and long-life images of the most stable structures, closed rings. The evolution of these rings under depolymerization conditions could be observed over long time periods. The structures obtained in these experiments differ from the previous filaments in the following aspects:

1. Only ring structures are observed so that an additional bond connects the two filament extremes and lateral attractions play no role (protein density on the "washed" surface is low and the surviving ring structures are distributed sparsely with no contact between them).
2. Rings are observed over several time frames so that we get dynamic information.
3. Bond dynamics with nonhydrolyzable (GMPCPP) and hydrolyzable (GTP) nucleotides may be compared.
4. The influence of the pH value can be analyzed.

Shape fluctuations are related to the flexibility of the rings while the typical ring size and the life time of the rings are given by their preferential curvature, polymerization and depolymerization rates, diffusion and entropic factors. We will start this chapter with a short description of the different data sets and of how different nucleotides and pH values are supposed to take influence on the polymerization and depolymerization properties of filaments. We will then develop the necessary analytical and Langevin dynamics simulation tools to analyse the experimental samples and finally apply these tools to estimate the bending properties of the rings and calibrate the time scale in the simulations.

6.1. Experimental samples

In these experiments, the shape evolution of FtsZ filament rings is observed until its depolymerization. AFM images of the same sample are taken in time steps of approximately one minute. A more detailed description of the experimental procedure can be found in Chp. 3. The size of the

data sets was between 240 and 375 ring conformations. One ring was observed during several time frames. The most stable ring survived during 140 frames but the typical survival time was in the order of 20 frames. Two factors took influence on the polymerization rate of the filaments: the type of nucleotide and the pH-value. In three of the data sets, the evolution of the filaments took place in presence of GTP bringing about unstable bonds as the GTP bound at the interface of two monomers is almost immediately hydrolysed to GDP followed by GDP-GTP exchange. Actually, the GTP-rate depends on the pH value of the buffer and decreases significantly for decreasing pH so that bonds should be more stable for lower pH values. The dependency between the bending rigidity and the pH value might reflect this tendency as unstable bonds might lead to more flexibility. We will check the validity of this assumption for filament evolutions in a buffer containing GTP at pH = 7.4, 6.5 and 5.0. Using the non hydrolyzable nucleotide GMPCPP instead of GTP has the same effect on the bond stability as lowering the pH value so that the filaments with GMPCPP should be stiffer than the filaments with GTP. The first step on the way of estimating the bending rigidities is the digitalization of the rings. We have used Bezier curves to trace the line of the rings and interpolated the monomer positions placing them along the curves separated by their size. Fig. 6.1 illustrates the original AFM images with superposed Bezier curves. In the next section, we will generally describe ring filament shapes in terms of Fourier series and then apply this description to experimental and simulated configurations.

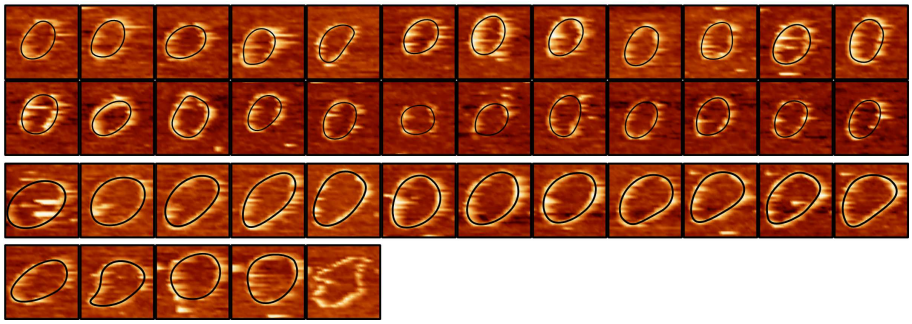

Figure 6.1.: Shape evolution of three rings from Fig. 3.3 with superposed Bezier curves for the digitalization of the ring coordinates.

6.2. Analytical analysis

The geometrical shape of closed FtsZ polymer rings can be described by considering small deviations from uniformly distributed monomer positions on a perfect circle. In polar coordinates these deviations can be expressed as deviations in the distance of the monomers to the center of the circle from a mean radius and deviations of the angular position of monomers from their optimal value corresponding to a uniform distribution. Figure (6.2) illustrates the parametrization we have chosen to describe the ring deformation. With d_o being the distance between monomers and $\varphi_o = 2\pi/N$ the angle between monomers in a perfect ring of length N, the radius of this ring is

$$r_o = \frac{d_o}{2\sin(\varphi_o/2)}. \tag{6.1}$$

The position of the k^{th} monomer is

$$\mathbf{r}_k = r_k \begin{pmatrix} \cos\varphi_k \\ \sin\varphi_k \end{pmatrix}, \tag{6.2}$$

and for small deviations Δr_k and $\Delta\varphi_k$ we get

$$\mathbf{r}_k \simeq (r_0 + \Delta r_k) \begin{pmatrix} \cos(k\varphi_o) \\ \sin(k\varphi_o) \end{pmatrix} + r_0 \Delta\varphi_k \begin{pmatrix} -\sin(k\varphi_o) \\ \cos(k\varphi_o) \end{pmatrix}. \tag{6.3}$$

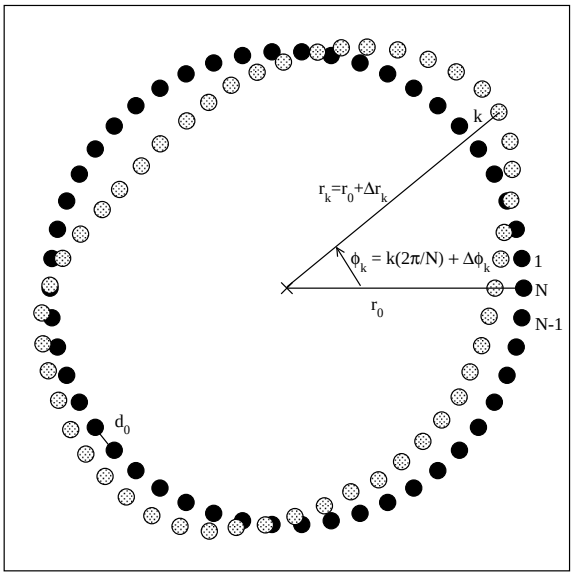

Figure 6.2.: Illustration of the ring parametrization

The thermal deviations of the monomer positions from their ideal positions depend on the flexibility of the polymer chains. They are directly related to the energy costs of changing the distance, d_k, and the bond angle, θ_k, between monomers:

$$\begin{aligned} U_b &= \sum_{k=1}^{N} \frac{\kappa_b}{2}(d_k - d_o)^2, \\ U_c &= \sum_{k=1}^{N} \frac{\kappa_c}{2}(\theta_k - \theta_o)^2, \\ d_k = \sqrt{(\mathbf{r}_{k+1} - \mathbf{r}_k)^2}, &\qquad \theta_k = \arccos\left[\frac{(\mathbf{r}_{k+1} - \mathbf{r}_k)(\mathbf{r}_k - \mathbf{r}_{k-1})}{|\mathbf{r}_{k+1} - \mathbf{r}_k||\mathbf{r}_k - \mathbf{r}_{k-1}|}\right]. \end{aligned} \tag{6.4}$$

The configurations that we observe in the AFM experiments are not circular. They are elongated in one direction and have much more an elliptical shape. This implies that the equilibrium angle between monomers is no longer constant (assuming that the distance between monomers remains constant). The analytical analysis of these configurations gets more complicated and so we will start with an analysis of circular shapes and mention some considerations about how to include the ellipticity in the second part of this section.

6.2.1. Circular shapes

Treating the deviations of the monomers from their ideal positions as small, the bond and the bond angle energies can be written as a Taylor series in Δr_k and $\Delta\varphi_k$:

$$U_b = \sum_{k=1}^{N} U_{b,k}^{0} + \frac{1}{2}\sum_{k=1}^{N}\Big[U_{b,k}^{r_k,\varphi_k}\Delta r_k^2 + U_{b,k}^{r_k,\varphi_k}\Delta\varphi_k^2 + U_{b,k}^{r_{k+1},\varphi_{k+1}}\Delta r_{k+1}^2 + U_{b,k}^{r_{k+1},\varphi_{k+1}}\Delta\varphi_{k+1}^2 + 2\left(U_{b,k}^{r_k,r_{k+1}}\Delta r_k\Delta r_{k+1} + U_{b,k}^{\varphi_k,\varphi_{k+1}}\Delta\varphi_k\Delta\varphi_{k+1} + U_{b,k}^{r_k,\varphi_{k+1}}\Delta r_k\Delta\varphi_{k+1} + U_{b,k}^{\varphi_k,r_{k+1}}\Delta\varphi_k\Delta r_{k+1}\right)\Big], \quad (6.5)$$

where $U_{b,k}^{r_k,r_k}$ means $\left.\frac{\partial^2 U_{b,k}}{\partial\Delta r_k^2}\right|_{\substack{\Delta r_k=0\\ \Delta\varphi_k=0}}$.

Contributions that are linear in Δr_k or $\Delta\varphi_k$ vanish as $\sum_k \Delta r_k = 0$ and $\sum_k \Delta\varphi_k = 0$. The curvature energy, U_c, can be expressed in the same way, including derivatives with respect to Δr_{k-1} and $\Delta\varphi_{k-1}$. Tbls. 6.1 and 6.2 contain the coefficients of the Taylor series up to quadratic order in φ_o.

$U_{b,k}^{r_k,r_k} = U_{b,k}^{r_{k+1},r_{k+1}} = U_{b,k}^{r_k,r_{k+1}}$	$\frac{\kappa_b}{2}\frac{\varphi_o^2}{2}$	$U_{b,k}^{r_k,\varphi_k} = -U_{b,k}^{r_{k+1},\varphi_{k+1}}$	$\frac{\kappa_b}{2}\left[-d_o + \frac{d_o}{8}\varphi_o^2\right]$
$U_{b,k}^{\varphi_k,\varphi_k} = U_{b,k}^{\varphi_{k+1},\varphi_{k+1}} = -U_{b,k}^{\varphi_k,\varphi_{k+1}}$	$\frac{\kappa_b}{2}d_o^2\left[\frac{2}{\varphi_o^2} - \frac{1}{3} + \frac{\varphi_o^2}{120}\right]$	$U_{b,k}^{r_k,\varphi_{k+1}} = -U_{b,k}^{r_{k+1},\varphi_k}$	$\frac{\kappa_b}{2}\frac{d_o}{4}(8-\varphi_o^2)$

Table 6.1.: Taylor series coefficients of the bond energy, U_b.

In the next step, we will express Δr_k and $\Delta\varphi_k$ as Fourier series:

$$\Delta r_k = \sum_{n=-\frac{N}{2}}^{\frac{N}{2}} A_n e^{ink\varphi_o}, \quad (6.6)$$

$$\Delta\varphi_k = \sum_{n=-\frac{N}{2}}^{\frac{N}{2}} B_n e^{ink\varphi_o}. \quad (6.7)$$

Hence we get:

$U_{c,k}^{r_k,r_k}$	$\frac{\kappa_c}{2}\frac{1}{d_o^2}\left[8+4\theta_0\varphi_o-6\varphi_o^2\right]$	$U_{b,k}^{r_k,\varphi_k}$	0
$U_{c,k}^{r_{k+1},r_{k+1}}=U_{c,k}^{r_{k-1},r_{k-1}}$	$\frac{\kappa_c}{2}\frac{1}{d_o^2}\left[2-2\theta_0\varphi_o+\frac{3}{2}\varphi_o^2\right]$	$U_{b,k}^{r_{k-1},\varphi_{k-1}}=-U_{b,k}^{r_{k+1},\varphi_{k+1}}$	$\frac{\kappa_c}{2}\frac{1}{d_o}\left[2\frac{\theta_0}{\varphi_o}-1-\frac{11}{12}\theta_0\varphi_o+\frac{19}{24}\varphi_o^2\right]$
$U_{c,k}^{r_{k-1},r_k}=U_{c,k}^{r_k,r_{k+1}}=-2U_{c,k}^{r_{k-1},r_{k+1}}$	$\frac{\kappa_c}{2}\frac{1}{d_o^2}(\varphi_o^2-4)$	$U_{b,k}^{r_{k-1},\varphi_{k+1}}=-U_{b,k}^{r_{k+1},\varphi_{k-1}}$	$\frac{\kappa_c}{2}\frac{1}{d_o}(-1+\frac{1}{8}\varphi_o^2)$
$U_{b,k}^{\varphi_k,\varphi_k}$	$-\frac{\kappa_c}{2}\left[4\frac{\theta_0}{\varphi_o}-4-\frac{\theta_0\varphi_o}{3}+\frac{\varphi_o^2}{3}\right]$	$U_{b,k}^{r_{k-1},\varphi_k}=-U_{b,k}^{r_{k+1},\varphi_k}$	$\frac{\kappa_c}{2}\frac{1}{d_o}\left[-2\frac{\theta_0}{\varphi_o}+2-\frac{1}{12}\theta_0\varphi_o+\frac{1}{12}\varphi_o^2\right]$
$U_{b,k}^{\varphi_{k+1},\varphi_{k+1}}=U_{b,k}^{\varphi_{k-1},\varphi_{k-1}}$	$\frac{\kappa_c}{2}\left[2\frac{\theta_0}{\varphi_o}-\frac{3}{2}-\frac{\theta_0\varphi_o}{6}+\frac{\varphi_o^2}{6}\right]$	$U_{b,k}^{r_k,\varphi_{k-1}}=-U_{b,k}^{r_k,\varphi_{k+1}}$	$\frac{\kappa_c}{2}\frac{1}{d_o}\left[-2\frac{\theta_0}{\varphi_o}-\frac{1}{12}\theta_0\varphi_o+\frac{1}{3}\varphi_o^2\right]$
$U_{b,k}^{\varphi_{k-1},\varphi_k}=U_{b,k}^{\varphi_k,\varphi_{k+1}}$	0		
$U_{b,k}^{\varphi_{k-1},\varphi_{k+1}}$	$-\frac{\kappa_c}{2}\frac{1}{2}$		

Table 6.2.: Taylor series coefficients of the curvature energy, U_c.

$$\begin{aligned}\sum_k \Delta r_k^2 &= \sum_{n=-\frac{N}{2}}^{\frac{N}{2}}\sum_{n'=-\frac{N}{2}}^{\frac{N}{2}}\sum_{k=1}^{N} A_n e^{ink\varphi_o} A'_n e^{-in'k\varphi_o} \\ &= N\sum_{n=-\frac{N}{2}}^{\frac{N}{2}} A_n A_n^* \\ &= NA_o^2 + 2N\sum_{n=1}^{\frac{N}{2}} A_n A_n^*, \qquad (6.8)\end{aligned}$$

$$\sum_k \Delta\varphi_k^2 = 2N\sum_{n=1}^{\frac{N}{2}} B_n B_n^*. \qquad (6.9)$$

B_0 equals 0 due to the definition of $\Delta\varphi_o = \frac{2\pi}{N}$.

$$\sum_k \Delta r_k \Delta r_{k+1} = NA_o^2 + 2N\sum_{n=1}^{\frac{N}{2}} A_n A_n^* \cos(n\varphi_o), \qquad (6.10)$$

$$\sum_k (\Delta r_{k+1}\Delta\varphi_k - \Delta r_k \Delta\varphi_{k+1}) = 2N\sum_{n=1}^{\frac{N}{2}} (A_n B_n^* - A_n^* B_n) i\sin(n\varphi_o). \qquad (6.11)$$

We can now write the bond and the curvature energy in the following way:

$$U_b = N\frac{\kappa_b}{2}\varphi_o^2 A_o^2 + N\frac{\kappa_b}{2}\sum_{n=1}^{\frac{N}{2}} (A_n, B_n)\begin{pmatrix} a_b & b_b \\ b_b^* & c_b\end{pmatrix}\begin{pmatrix} A_n^* \\ B_n^*\end{pmatrix}, \qquad (6.12)$$

$$U_c = N\frac{\kappa_c}{2}\sum_{n=1}^{\frac{N}{2}}(A_n, B_n)\begin{pmatrix} a_c & b_c \\ b_c^* & c_c \end{pmatrix}\begin{pmatrix} A_n^* \\ B_n^* \end{pmatrix}, \tag{6.13}$$

with

$$\begin{aligned} a_b &= \varphi_o^2[1+\cos(n\varphi_o)], \\ b_b &= i\frac{d_o}{4}(\varphi_o^2-8)\sin(n\varphi_o), \\ c_b &= 2d_o^2\left(\frac{2}{\varphi_o^2}-\frac{1}{3}+\frac{\varphi_o^2}{120}\right)[1-\cos(n\varphi_o)], \end{aligned} \tag{6.14}$$

and

$$\begin{aligned} a_c &= \frac{4-\varphi_o^2}{d_o^2}[3-4\cos(n\varphi_o)+\cos(2n\varphi_o)], \\ b_c &= i\frac{\varphi_o^2-8}{4d_o}[2\sin(n\varphi_o)-\sin(2n\varphi_o)], \\ c_c &= 1-\cos(2n\varphi_o). \end{aligned}$$

We can now express the total energy of the ring as follows:

$$U = N\frac{\kappa_b}{2}\varphi_o^2 A_o^2 + \frac{N}{2}\sum_{n=1}^{\frac{N}{2}}(A_n, B_n)\begin{pmatrix} a & b \\ b^* & c \end{pmatrix}\begin{pmatrix} A_n^* \\ B_n^* \end{pmatrix}, \tag{6.15}$$

with

$$\begin{aligned} a &= \kappa_b a_b + \kappa_c a_c, \\ b &= \kappa_b b_b + \kappa_c b_c, \\ c &= \kappa_b c_b + \kappa_c c_c. \end{aligned}$$

The energy can be written as a sum of orthogonal contributions. Therefore we have to determine the Eigenvalues and the Eigenvectors of the matrix:

$$\lambda_{1/2} = \frac{a+c}{2} \pm \frac{1}{2}\sqrt{(a-c)^2+4bb^*}, \tag{6.16}$$

$$u_1 = \frac{1}{\sqrt{bb^*+(a-\lambda_1)^2}}\begin{pmatrix} b \\ \lambda_1 - a \end{pmatrix}, \qquad u_2 = \frac{1}{\sqrt{bb^*+(a-\lambda_1)^2}}\begin{pmatrix} a-\lambda_1 \\ b^* \end{pmatrix}. \tag{6.17}$$

We can now write

$$\begin{pmatrix} a & b \\ b^* & c \end{pmatrix} = U_t \begin{pmatrix} \lambda_1 & 0 \\ 0 & \lambda_2 \end{pmatrix} U_t^{-1}, \tag{6.18}$$

with

$$\begin{aligned} U_t &= \frac{1}{\sqrt{bb^* + (a-\lambda_1)^2}} \begin{pmatrix} b & a-\lambda_1 \\ \lambda_1 - a & b^* \end{pmatrix}, \\ U_t^{-1} &= \frac{1}{\sqrt{bb^* + (a-\lambda_1)^2}} \begin{pmatrix} b^* & \lambda_1 - a \\ a-\lambda_1 & b \end{pmatrix}. \end{aligned} \tag{6.19}$$

The total energy becomes

$$U = N\frac{\kappa_b}{2}\varphi_o^2 A_o^2 + \frac{N}{2}\sum_{n=1}^{\frac{N}{2}} (v_n, w_n) \begin{pmatrix} \lambda_1 & 0 \\ 0 & \lambda_2 \end{pmatrix} \begin{pmatrix} v_n^* \\ w_n^* \end{pmatrix}, \tag{6.20}$$

and the average total energy

$$< U > = N\frac{\kappa_b}{2}\varphi_o^2 < A_o^2 > + \frac{N}{2}\sum_{n=1}^{\frac{N}{2}} (\lambda_1 < v_n^2 > + \lambda_2 < w_n >^2). \tag{6.21}$$

Using the law of equipartition of energy, we can calculate the average values of $< v_n^2 >$ and $< w_n^2 >$,

$$< v_n^2 > = \frac{2k_BT}{N\lambda_1}, \qquad < w_n^2 > = \frac{2k_BT}{N\lambda_2}. \tag{6.22}$$

Back transformation gives the average values of $< A_n^2 >$, $< B_n^2 >$, $< A_n^* B_n + A_n B_n^* >$ and $< A_n^* B_n - A_n B_n^* >$:

$$\begin{aligned} A_n &= \frac{1}{\sqrt{bb^* + (a-\lambda_1)^2}}(b^* v_n + (a-\lambda_1) w_n), \\ B_n &= \frac{1}{\sqrt{bb^* + (a-\lambda_1)^2}}((\lambda_1 - a) v_n + b w_n), \\ < A_n^2 > &= \frac{bb^*}{bb^* + (a-\lambda_1)^2} < v_n^2 > + \frac{(a-\lambda_1)^2}{bb^* + (a-\lambda_1)^2} < w_n^2 >, \\ < B_n^2 > &= \frac{(a-\lambda_1)^2}{bb^* + (a-\lambda_1)^2} < v_n^2 > + \frac{bb^*}{bb^* + (a-\lambda_1)^2} < w_n^2 >, \\ < A_n^* B_n + A_n B_n^* > &= 0, \\ < A_n^* B_n - A_n B_n^* > &= \frac{2b(a-\lambda_1)}{bb^* + (a-\lambda_1)^2}(< w_n^2 > - < v_n^2 >). \end{aligned} \tag{6.23}$$

Using d_o as the unit length, for small angles φ_o ($N \gtrapprox 50$) these expressions reduce to:

$$\begin{aligned} < A_n^2 > &= \frac{3N^3}{4\pi^4(\kappa_b + 12\kappa_c(1-n^2)^2)}, \\ < B_n^2 > &= \frac{3N}{\pi^2 n^2(\kappa_b + 12\kappa_c(1-n^2)^2)}, \\ < A_n^* B_n - A_n B_n^* > &= \frac{3N^2}{\pi^3 n(\kappa_b + 12\kappa_c(1-n^2)^2)}. \end{aligned} \tag{6.24}$$

This approximation is valid only for the lower Fourier coefficients (n small) as it contains approximations of $\sin(n\varphi_o)$ and $\cos(n\varphi_o)$ for small angles.

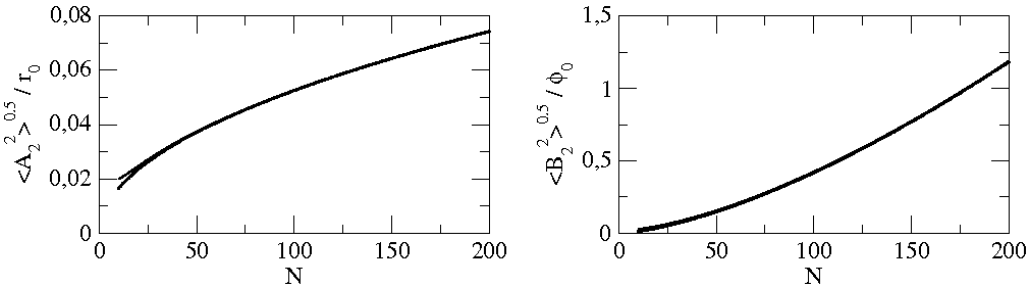

Figure 6.3.: Relative mean quadratic deviations, $\frac{\sqrt{<A_2^2>}}{r_o}$ and $\frac{\sqrt{<B_2^2>}}{\varphi_o}$ of the leading Fourier coefficients of a polymer ring of length N. The monomers are connected by bonds with spring constants $\kappa_b = 200\frac{kT}{d_o^2}$ and $\kappa_c = 100kT$. The continuous line shows the full expression, Eq. 6.23, and the circles represent the approximation, Eq. 6.24.

More meaningful than the absolute values of $< A_n^2 >$ and $< B_n^2 >$ are the relative mean deviations of the monomer positions, which we can express as the relative mean quadratic deviation of its radius, $\frac{\sqrt{<A_n^2>}}{r_o}$, and its angular position, $\frac{\sqrt{<B_n^2>}}{\varphi_o}$. For the leading Fourier coefficients we get (Fig. 6.3):

$$\frac{< A_2^2 >}{r_o^2} = \frac{3N}{\pi^2(\kappa_b + 108\kappa_c)}, \tag{6.25}$$

$$\frac{< B_2^2 >}{\varphi_o^2} = \frac{3N^3}{16(\kappa_b + 108\kappa_c)}. \tag{6.26}$$

For the radius, the relative deviation in the Fourier coefficients grows with $\sqrt{N}$ and for the angle we find a $\sqrt{N}^3$ dependency. Eq. 6.25 relates the mean quadratic deviation of the leading Fourier coefficient, A_2, to the spring constants κ_b and κ_c. This relation is very useful, connecting the global shape of the polymer ring, as it can be captured experimentally, to the interaction between its constituent parts, the monomers. Another interesting question is how we can directly express the mean quadratic deviation of the angle between monomers by means of the Fourier coefficients of the ring shape.

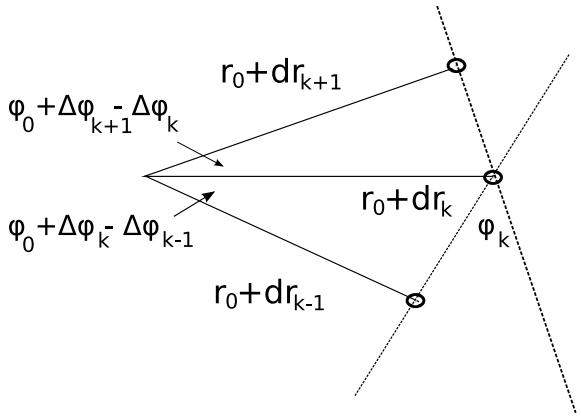

Figure 6.4: Illustration of the angle between monomers, θ_k.

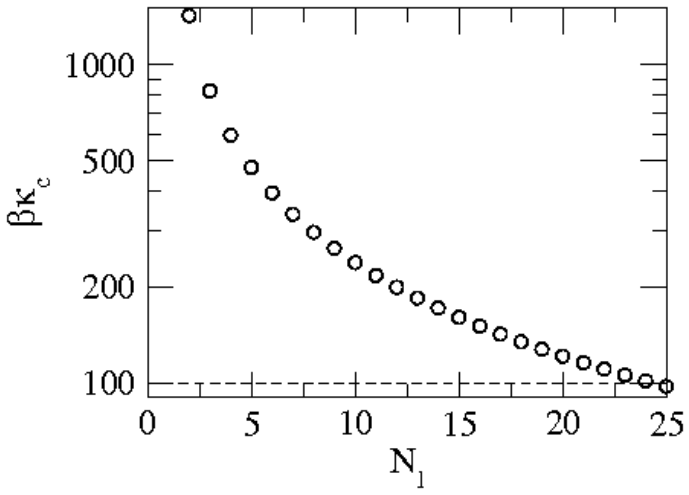

Figure 6.5: Angle spring constant, $\beta\kappa_c$, calculated from Eq. 6.28 and evaluating the sum over n up to N_l (circles). We have used $N = 50$, $\beta\kappa_b = 200$ and $\beta\kappa_c = 100$ (dashed line).

Angle between monomers

Within the parametrization $\Delta\varphi_k, \Delta r_k$ we can linearize Eq. 6.7 for the angle between monomers, θ_k, for small equilibrium angles φ_o:

$$\theta_k = \varphi_o + \frac{1}{2}(\Delta\varphi_{k+1} - \Delta\varphi_{k-1}) + 2\Delta r_k - \Delta r_{k+1} - \Delta r_{k-1} \tag{6.27}$$

The angular spring constant, κ_c, is related to the mean quadratic deviation in the angle between monomers:

$$\begin{aligned}
\frac{1}{\beta\kappa_c} &= <(\theta_k - \theta_o)^2> - <\theta_k - \theta_o>^2 \\
&= <\theta_k^2> - \varphi_o^2 \\
&= 6<\Delta r_k^2> - 8<\Delta r_k \Delta r_{k+1}> + 2<\Delta r_{k-1}\Delta r_{k+1}> + \frac{1}{2}\left(<\Delta\varphi_k^2> - <\Delta\varphi_{k-1}\Delta\varphi_{k+1}>\right) \\
&= 4\sum_{n=1}^{\frac{N}{2}} <A_n^2>(3 - 4\cos(n\varphi_o) + \cos(2n\varphi_o)) + \sum_{n=1}^{\frac{N}{2}} <B_n^2>(1 - \cos(n\varphi_o)).
\end{aligned} \tag{6.28}$$

The direct calculation of the angle spring constant involves the knowledge of the whole series of Fourier coefficients as Fig. 6.5 shows. Hence, this method is not suitable for the estimation of κ_c

from experimental data, as it would require the resolution of single monomers (needed in order to do the complete Fourier analysis) so that the advantage over the direct calculation of the angle between monomers is completely lost.

6.2.2. Elliptical shapes

The rings that we find in the AFM images have a non isotropic distribution of shapes. Probably due to an interaction between the mica and the FtsZ proteins, the rings appear stretched along a specific axes of the mica and their mean shape is slightly elliptical.

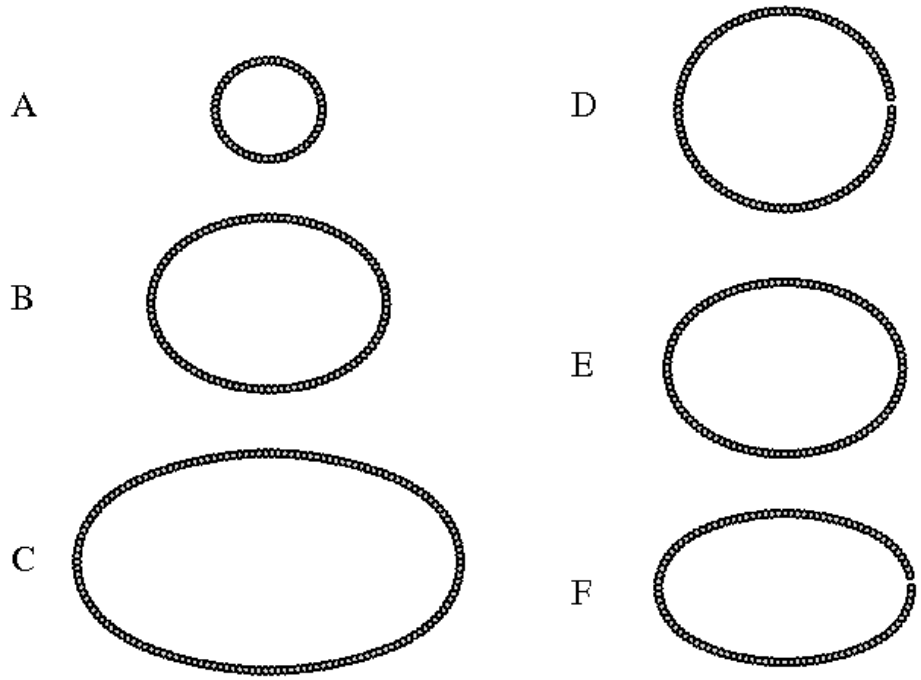

Figure 6.6.: On the left, the stretching factor is fixed to $\beta\gamma = 0.4$. The relative elongation of the ellipse becomes stronger for growing monomer number (A) $N = 50$, B) $N = 100$, C) $N = 150$). On the right, a chain with 100 monomers is stretched with a stretching factor of D) $\beta\gamma = 0.1$, E) $\beta\gamma = 0.4$ and F) $\beta\gamma = 0.8$.

We will introduce this ellipticity in form of an additional energy term which includes a cost for bonds along the y-axis and a gain for bonds along the x-axis,

$$U_s = \sum_{k=1}^{N} \frac{\gamma}{2}(\mathbf{r}_{k+1} - \mathbf{r}_k)(\hat{e}_y - \hat{e}_x). \tag{6.29}$$

For $\gamma = 0$, the equilibrium shape of a closed polymer ring is found for equally distributed distances and angles between its monomers as in a perfect circle. The monomer positions in this case can be described by r_o and $k\Delta\varphi$ while Δr_k and $\Delta\varphi_k$ are zero and therewith all of their Fourier coefficients. Including the additional stretching energy term we will approximate the monomer positions, keeping the above description, but now Δr_k and $\Delta\varphi_k$ are no longer zero at equilibrium.

The shape of the ellipse can be found be searching for the minimum of $U = U_b + U_c + U_s$ with respect to all of the Fourier coefficients A_n^0 and B_n^0. For symmetry reasons, only symmetric deformations of the circle are allowed and so all impair coefficients must equal zero. A closed analytical solution of this problem is complicated as the optimal distance and angle between two adjacent monomers depend not only on their relative positions but also on the global orientation of their connecting axes. We limited the calculation to Fourier coefficients up to order four and got numerical results for A_o^0, A_2^0, A_4^0, B_2^0 and B_4^0 for fixed polymer length as a function of the stretching factor, γ, and for fixed γ as a function of N (Fig. 6.7).

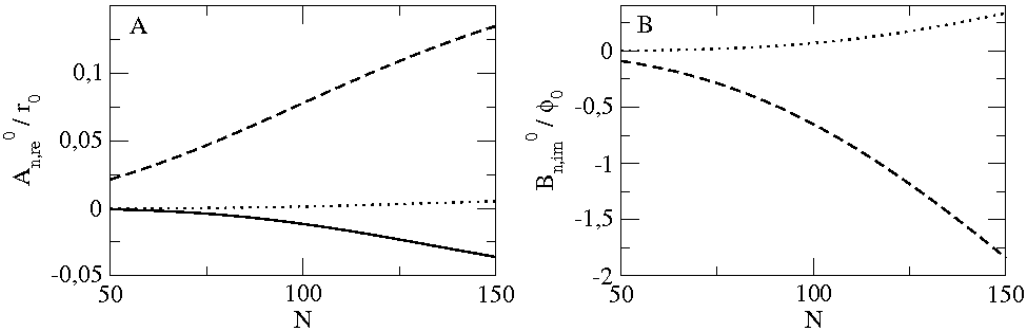

Figure 6.7.: Fourier coefficients for the equilibrium shape of a polymer ring, stretched by $\beta\gamma = 0.4$ as a function of the ring length, N. A) $A_{0,re}^0$ (continuous line), $A_{2,re}^0$ (dashed line) and $A_{4,re}^0$ (pointed line). B) $B_{4,re}^0$ (dashed line) and $B_{4,im}^0$ (pointed line).

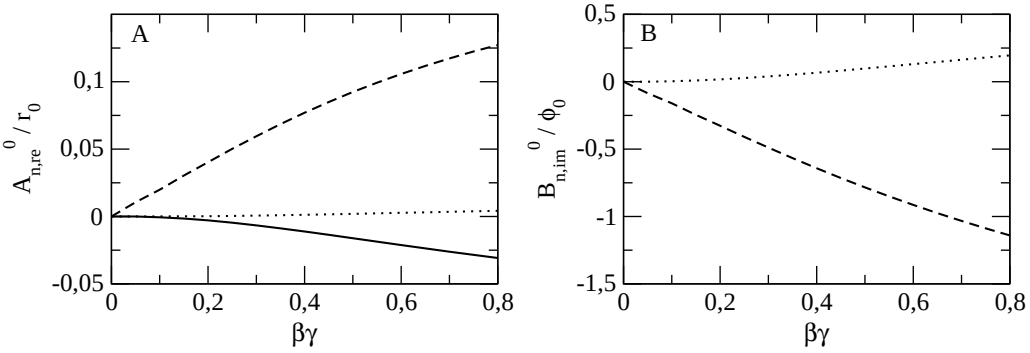

Figure 6.8.: Fourier coefficients for the equilibrium shape of a polymer ring of $N = 100$ monomers as a function of the stretching factor, γ. A) $A_{0,re}^0$ (continuous line), $A_{2,re}^0$ (dashed line) and $A_{4,re}^0$ (pointed line). B) $B_{4,re}^0$ (dashed line) and $B_{4,im}^0$ (pointed line).

Due to the definition of the orientation of the stretching energy, the imaginary part of A_n^0 and the real part of B_n^0 vanish. The evolution of A_2^0 as a function of the chain length shows that the relative elongation of the ellipse becomes stronger as the number of monomers increases. Now, what about the mean quadratic values of the Fourier coefficients? There will no longer be a direct relation between $< A_2^2 >$ and the bending rigidity of the chain, κ_c. For small values of γ, the mean quadratic deviation of A_2 might not be too different from the values found for $\gamma = 0$. We can calculate σ_{A_2} as follows:

$$\sigma^2_{A_2} = < A_2^2 > - < A_2 >^2 = < A_{2,re}^2 + A_{2,im}^2 > - < A_{2,re} >^2 - < A_{2,im} >^2 \tag{6.30}$$

This quantity is easily accessible in our simulations and in the next section, we will check the validity of the assumption that σ_{A_2} is independent of γ for small stretching deformations in Langevin dynamics simulations of circles and ellipses.

6.3. Simulation of FtsZ filament rings

The purpose of the analysis of the phenomenology of ring conformations is to use the available experimental information on the global behaviour of FtsZ polymer chains to extract the origin of this behaviour which is found in the interaction between single monomers. We have seen that the analytical analysis offers a good method to calculate the angle spring constant between monomers using only the mean quadratic deviation of the leading Fourier coefficient of the radius of the ring, a value which can easily be extracted from the AFM images of polymer rings. The reason for the ellipticity of the conformations does not lie in the interaction between monomers but in the interaction between the polymer chain and the substrate. We have done simulations to check to what extent the ellipticity takes influence on the fluctuations of the Fourier coefficients starting with simulations of isotropic rings to test whether the results of the analytical analysis can be reproduced.

6.3.1. Circular shapes

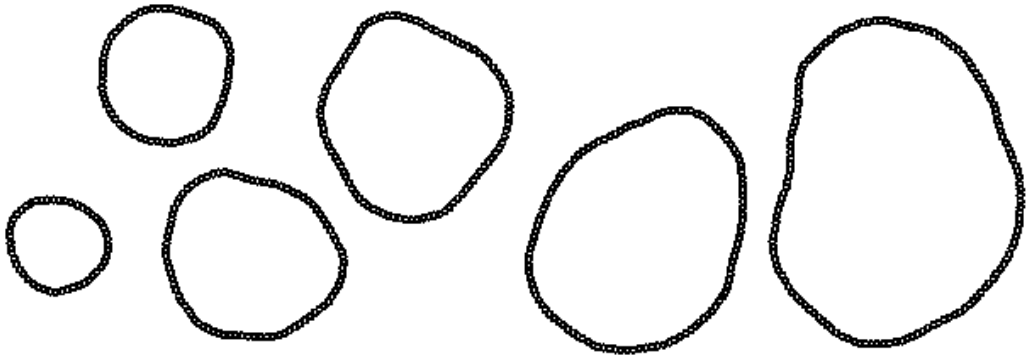

Figure 6.9.: Typical ring conformations from a simulation with $\beta\kappa_c = 100$. From left to right: $N = 50, 70, 90, 100, 120, 150$.

Compared to the simulation of a simple polymer chain, we first have to introduce an interaction between monomer 1 and monomer N. This can be easily done by simply treating the extremes like monomers in the interior of the chain. We are interested in the Fourier coefficients of the radius and the angle of the monomer positions during the simulation,

$$A_n = \frac{1}{N}\sum_{k=1}^{N} \Delta r_k \left[\cos(nk\varphi_o) + i\sin(nk\varphi_o)\right], \tag{6.31}$$

$$B_n = \frac{1}{N}\sum_{k=1}^{N} \Delta \varphi_k \left[\cos(nk\varphi_o) + i\sin(nk\varphi_o)\right]. \tag{6.32}$$

In order to check the accordance between the analytical analysis and the simulation, we calculated the mean values of A_2^2 and B_2^2 for different lengths of the polymer chain (Fig. 6.10). Therefore, we run the simulation over 10^9 time steps for $N < 100$ and 10^{10} time steps for $N > 100$, calculating the Fourier coefficients each 10^5 (10^6) time steps.

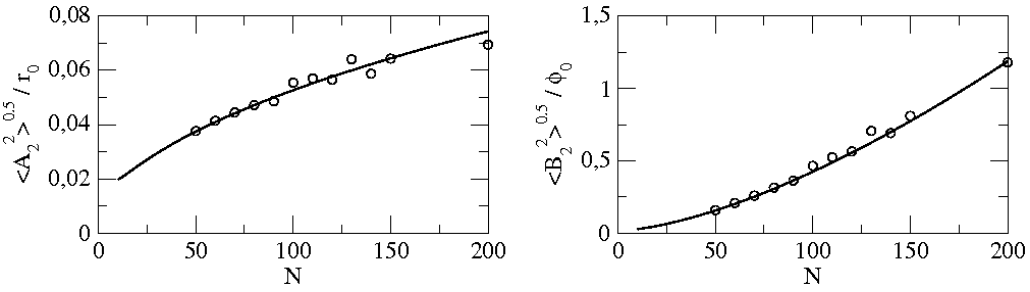

Figure 6.10.: Relative mean quadratic values, $\frac{\sqrt{<A_2^2>}}{r_o}$ and $\frac{\sqrt{<B_2^2>}}{\varphi_o}$, of the leading Fourier coefficients of a polymer ring of length N. The monomers are connected by bonds with spring constants $\beta\kappa_b = 200$ and $\beta\kappa_c = 100$. The continuous line shows the result of the analytical analysis, Eq. 6.23 and the circles are the values calculated from the simulation data.

We get very good accordance for short chains. For longer chains, the results could be improved by longer simulation times. Fig. 6.9 shows some snapshots of the simulation for different polymer lengths. Here we can see that the relative deformation of the ring becomes stronger for growing chain length. As a next step, we include the stretching potential that will lead to elliptical ring conformations.

6.3.2. Elliptical shapes

The forces that result from the stretching potential Eq. 6.29 and that we have included in the simulations are:

$$F_{xk}^s = -\frac{\delta U_s}{\delta x_k} = -\gamma(x_{k-1} - 2x_k + x_{k+1}), \tag{6.33}$$

$$F_{yk}^s = -\frac{\delta U_s}{\delta y_k} = \gamma(y_{k-1} + 2y_k + y_{k+1}). \tag{6.34}$$

We did the same simulations as above for $\gamma = 0$, setting now $\beta\gamma = 0.4$. We used the ellipses calculated above as initial configurations. Fig. 6.11 shows some snapshots of configurations during the simulations. Now, we get two results. On the one hand, we can compare the mean values of the Fourier coefficients to the result of the numerical energy minimization with respect to

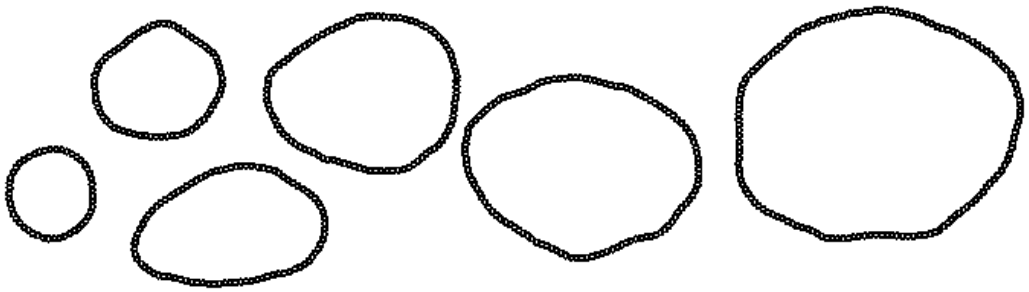

Figure 6.11.: Typical elliptical conformations from a simulation with $\beta\kappa_c = 100$ and $\beta\gamma = 0.4$. From left to right: $N = 50, 70, 90, 100, 120, 150$.

$A_o^0, A_2^0, A_4^0, B_2^0$ and B_4^0 (Fig. 6.12). On the other hand, we can now check the validity of the assumption, that the mean quadratic deviation of these coefficients can be approximated by the values for $\gamma = 0$. The mean values found in the simulation are in good agreement with the calculated equilibrium coefficients. The large deviations for $< A_{4,re} >$ can be explained by an overestimation of $A_{4,re}^0$ in the determination of the equilibrium shape because higher coefficients are not included in the calculation. Fig. 6.13 shows the mean quadratic deviations of A_2 and B_2.

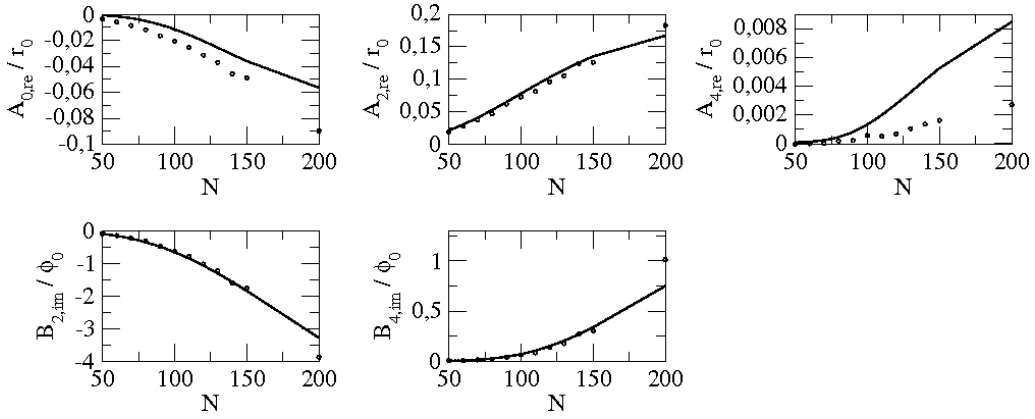

Figure 6.12.: Circles: mean values $< A_{0,re} >$, $< A_{2,re} >$, $< A_{4,re} >$, $< B_{2,im} >$ and $< B_{4,im} >$ calculated in a simulation with $\beta\gamma = 0.4$ and $\beta\kappa_c = 100$ compared to the equilibrium values resulting from the numerical energy minimization (continuous line).

We confirm, in particular for A_2, the approximation, that σ_{A_2} is independent of γ (for values of $\frac{\gamma}{\kappa_c}$ up to at least 0.004) . This assumption will help us to estimate the parameters γ and κ_c that best reproduce the experimental data.

6.4. Experimental results

We have analysed four data sets of FtsZ filament rings on mica substrate under depolymerization conditions. In three of them the buffer contained GTP and the pH values were 7.4, 6.5 and 5.0. In the fourth sample, GTP was replaced by GMPCPP at pH=7.4. The rings could be observed over

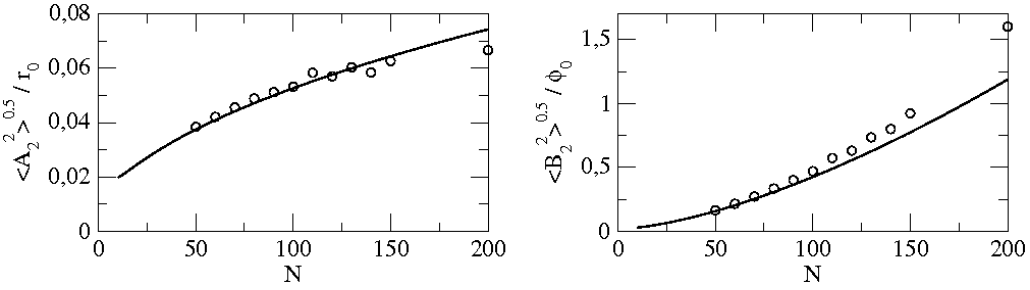

Figure 6.13.: Relative mean quadratic values, $\frac{\sqrt{<A_2^2>}}{r_o}$ and $\frac{\sqrt{<B_2^2>}}{\varphi_o}$ of the leading Fourier coefficients of a polymer ring of length N with $\beta\kappa_c = 100$ and $\beta\gamma = 0.4$. The continuous line shows the result of the analytical analysis, Eq. 6.23 for $\gamma = 0$ and the circles are the values calculated from the simulation data.

several time frames (between 4 and 141). Images were taken every 60s. Each data set consists of ≈ 300 ring conformations of ≈ 10 different rings observed during shorter or longer time periods:

	FtsZ - GTP pH = 7.4	FtsZ - GTP pH = 6.5	FtsZ - GTP pH = 5	FtsZ - GMPCPP pH = 7.4
# of rings	340	239	353	365

6.4.1. Estimation of Anisotropy and Bending rigidity

First of all, we have to mention that the resolution of the AFM images is not sufficient to distinguish single monomers. So, the only reliable data that we can extract are the lowest order Fourier coefficients of the radius of the polymer rings. We do not have any information about the angular positions of the monomers. The experimental data clearly show an anisotropy of the rings. On average, they are not circular but elliptical. We suppose that the reason for this ellipticity is an interaction between the monomers and the substrate that favors polymerization along certain axes of the mica. As the orientation of the mica is not under control, the directions of these axes are unknown and compared to the simulations there is a lack of information. In the simulations, both components of the Fourier coefficients, the real and the imaginary part, can be calculated and averaged independently as they can be defined with respect to the axes of the stretching potential. This is not possible in the experiment so that it is not possible to calculate σ_{A_2}. There are still two quantities that can be extracted from the experimental data, the mean absolute value of A_2 and its mean quadratic deviation, $< |A_2| >$ and $\sigma_{|A_2|}$ respectively. In order to get a relation between these quantities and κ_c and γ we will start with the probability distribution function of A_2. The probability distributions of the real and the imaginary part of A_2 are purely gaussian:

$$f(A_{2,re}) = \frac{1}{\sqrt{2\pi}\sigma_{A_{2,re}}} \exp\left(-\frac{(A_{2,re} - A^0_{2,re})^2}{2\sigma^2_{A2_re}}\right), \tag{6.35}$$

$$f(A_{2,im}) = \frac{1}{\sqrt{2\pi}\sigma_{A_{2,im}}} \exp\left(-\frac{(A_{2,im} - A^0_{2,im})^2}{2\sigma^2_{A2_im}}\right), \tag{6.36}$$

and

$$f(A_2 = A_{2,re} + IA_{2,im}) = f(A_{2,re})f(A_{2,im}). \tag{6.37}$$

Let us first consider circular shapes.

$\underline{\gamma = 0}$

In this case, $A^0_{2,re}$ and $A^0_{2,im}$ vanish and $\sigma_{A_{2,re}} = \sigma_{A_{2,im}} := \sigma_{A_2}$. The Fourier coefficients between $|A_2|$ and $|A_2| + dA_2$ are found between two circles with radius $|A_2|$ and $|A_2| + dA_2$, covering a surface of $2\pi|A_2|dA_2$. The probability distribution for $|A_2|$ becomes

$$f(|A_2|) = \frac{|A_2|}{\sigma^2_{A_2}} \exp\left(-\frac{A_2^2}{2\sigma^2_{A_2}}\right). \tag{6.38}$$

Using this probability distribution, we get

$$< A_2^2 > = 2\sigma^2_{A_2}, \tag{6.39}$$

$$< |A_2| > = \sqrt{\frac{\pi}{2}}\sigma_{A_2}. \tag{6.40}$$

We can now relate $\sigma^2_{A_2}$ to the bending rigidity, Eq. 6.25:

$$\sigma^2_{A_2/\sqrt{N}r_o} = \frac{1}{72\pi^2\kappa_c}. \tag{6.41}$$

Here we neglect κ_b as it is of the same order of magnitude as κ_c. Fig. 6.14 shows that for circular shapes the theoretical predictions of the probability distributions agree with the simulation results. Especially Fig. 6.14C shows that the bending rigidity of the chain, κ_c, is directly related to the width of the distribution of the absolute value of the Fourier coefficient, A_2. For elliptical shapes, the distribution of $|A_2|$ is more complicated and we will have to make some approximations.

$\underline{\gamma > 0}$

In the analytical analysis and in simulations we control the orientation of the stretching axis, not so in the experiments. We can express the probability distribution of A_2 with respect to the angle θ between the stretching axis and the coordinate system where we measure the real and the imaginary part of the Fourier coefficients,

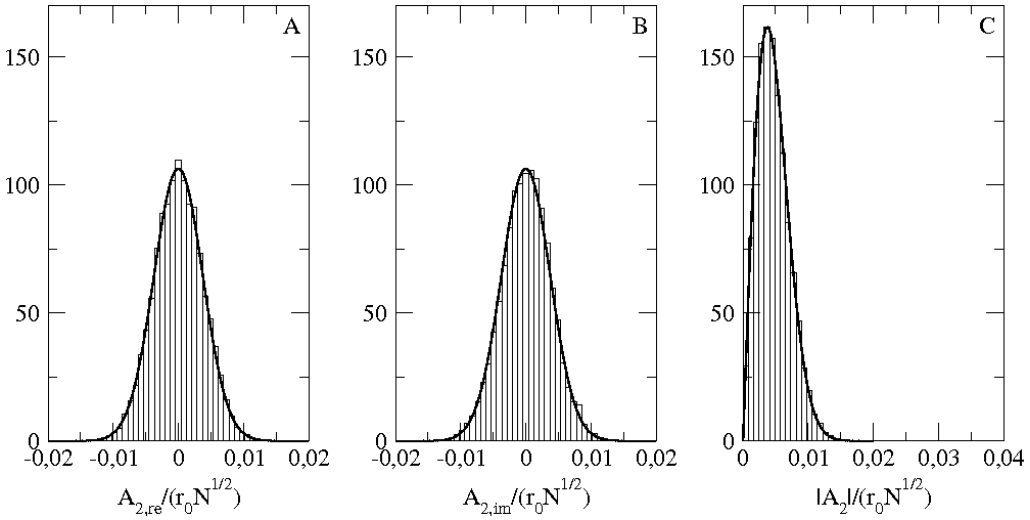

Figure 6.14.: Probability distributions of the Fourier coefficients $A_{2,re}$, $A_{2,im}$ and $|A_2|$. The histogram shows the result of a simulation with $N = 50$, $\beta\kappa_c = 100$ and $\gamma = 0$ and the black lines are the corresponding theoretical distributions Eqs. 6.35, 6.36 and 6.38 with $\sigma^2_{A_2/\sqrt{N}r_o}$ as in Eq. 6.41.

$$f(A_2,\theta) = \frac{1}{2\pi\sigma^2_{A_2}} \exp\left(-\frac{(A_{2,re} - A_o\cos(\theta))^2 + (A_{2,im} - A_o\sin(\theta))^2}{2\sigma^2_{A_2}}\right). \tag{6.42}$$

Here we assume a gaussian distribution of the real and the imaginary part of A_2 with equal mean deviation. We will see later that this is a good approximation only for short chains and small stretching coefficients. With $A_{2,re} = |A_2|\cos(\varphi)$ and $A_{2,im} = |A_2|\sin(\varphi)$ we get:

$$\begin{aligned} f(|A_2|,\theta) &= \frac{|A_2|}{2\pi\sigma^2_{A_2}} \\ &\quad \int_0^{2\pi} d\varphi \exp\left(-\frac{A_2^2 + A_o^2 - 2A_o(|A_2|\cos(\varphi)\cos(\theta) + |A_2|\sin(\varphi)\sin(\theta))}{2\sigma^2_{A_2}}\right) \\ &= \frac{|A_2|}{2\pi\sigma^2_{A_2}} \exp\left(-\frac{A_2^2 + A_o^2}{2\sigma^2_{A_2}}\right) \int_0^{2\pi} d\varphi \exp\left(\frac{2A_o|A_2|\cos(\varphi - \theta)}{2\sigma^2_{A_2}}\right), \end{aligned} \tag{6.43}$$

$$f(|A_2|) = \frac{|A_2|}{\sigma^2_{A_2}} \exp\left(-\frac{A_2^2 + A_o^2}{2\sigma^2_{A_2}}\right) I_0\left(\frac{A_o|A_2|}{\sigma^2_{A_2}}\right). \tag{6.44}$$

$I_0(x)$ is the first Bessel Integral,

$$I_0(x) = \frac{1}{2\pi}\int_0^{2\pi} \exp(x\cos(\varphi))d\varphi, \tag{6.45}$$

and the phase, θ, vanishes in the integration.
The probability distribution of the absolute value of A_2, which can be extracted from the experiments, is determined by σ_{A_2} and A_2^0 which are related to the material parameters κ_c and γ. The

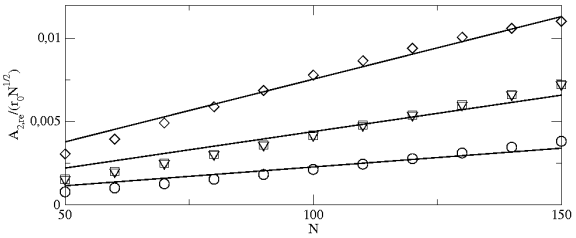

Figure 6.15: $A^0_{2,re}$ as a result of the numerical energy minimization of a chain with length N. Circles: $\beta\gamma = 0.1, \beta\kappa_c = 100$, squares: $\beta\gamma = 0.2, \beta\kappa_c = 100$, diamonds: $\beta\gamma = 0.4, \beta\kappa_c = 100$, triangles: $\beta\gamma = 0.1, \beta\kappa_c = 50$. The lines are linear fits of the numerical data points.

relation between the bending rigidity of the chain and σ_{A_2} is given by Eq. 6.41 and $A^0_2 = A^0_{2,re}$ for $\theta = 0$ as it is the case in the simulation and in the analytical analysis. The relation between $A^0_{2,re}$ and γ is less straight. Fig. 6.15 shows $A^0_{2,re}$ as a result of the numerical energy minimization of a chain with bending rigidity κ_c and stretching factor γ as a function of the chain length. We can approximate the relation between $A^0_{2,re}$ and κ_c, γ and N by

$$\frac{A^0_{2,re}}{r_0\sqrt{N}} \approx c_o \frac{\gamma}{\kappa_c} N. \tag{6.46}$$

Analysing the four parameter pairs, $\beta\kappa_c = 100, \beta\gamma = 0.1, 0.2, 0.4$ and $\beta\kappa_c = 50, \beta\gamma = 0.1$, we get $c_o = 0.021 \pm 0.002$.

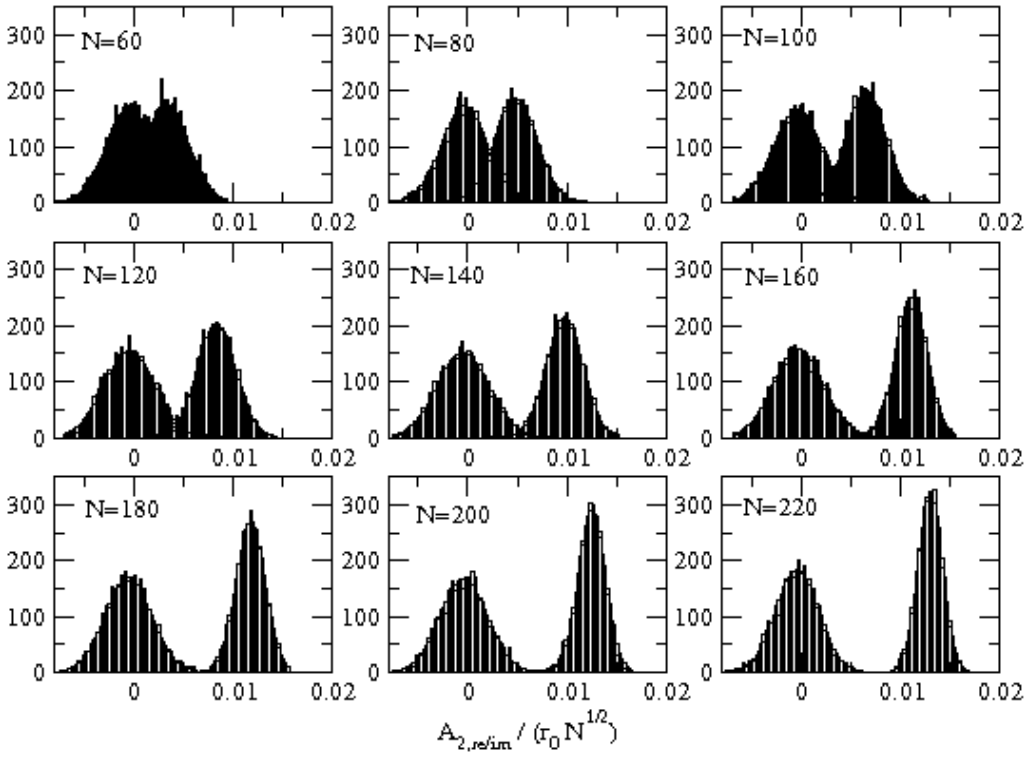

Figure 6.16.: Probability distributions of the Fourier coefficients $A_{2,re}$ and $A_{2,im}$ for different chain lengths. The histograms show the result of a simulation with $\beta\kappa_c = 300$ and $\beta\gamma = 1.0$. The lines are the least mean squares fits of the distributions using Eqs. 6.35 and 6.36.

We can actually not confirm the validity of the above assumption, $\sigma_{A_{2,re}} \approx \sigma_{A_{2,im}}$, for chains

longer than $N \approx 100$ and $\beta\kappa_c = 300$, $\beta\gamma = 1$ (Fig. 6.16). The rings seem to become stiffer with respect to deformations along the long elliptical axes. This effect becomes more important for growing chain length and can not be neglected as it changes significantly the interpretation of the mechanical parameters of the filaments. The distribution of the absolute value of A_2 becomes

$$f(|A_2|, \theta = 0) = \frac{|A_2|}{2\pi\sigma_{A_2,re}\sigma_{A_2,im}} \int_0^{2\pi} d\varphi \exp\left(-\frac{(|A_2|\cos(\varphi) - A_o)^2}{2\sigma^2_{A_2,re}} - \frac{|A_2|\sin(\varphi)}{2\sigma^2_{A_2,im}} \right).$$

The real and the imaginary part of the Fourier coefficients can be considered as independently Gaussian distributed only in the case of choosing the elliptical axis as the reference system, so that we have to set $\theta = 0$.

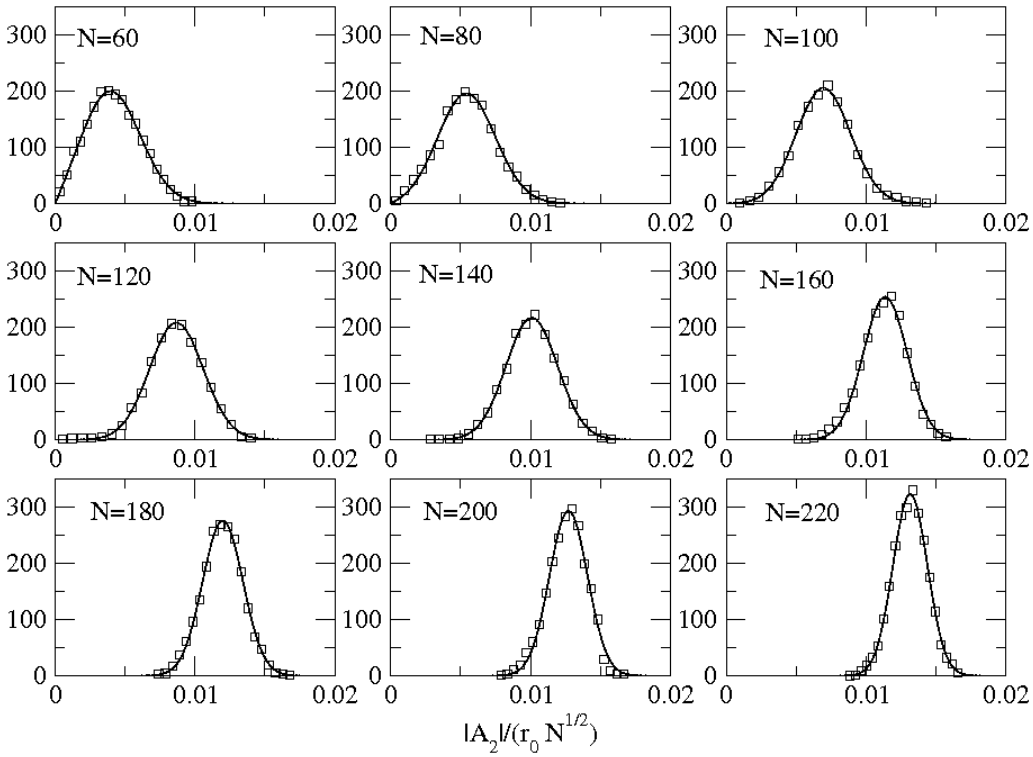

Figure 6.17.: Probability distributions of the absolute values of the coefficients A_2 for different chain lengths. The squares represent the result of a simulation with $\beta\kappa_c = 300$ and $\beta\gamma = 1.0$. The lines are the least mean squares fits of the distributions using Eq. 6.44.

Fig. 6.17 shows distributions of the absolute value of A_2 obtained in simulations with chain lengths between $N = 60$ and $N = 220$ and $\beta\kappa_c = 300$, $\beta\gamma = 1$. For the least mean squares fit we used Eq. 6.44 instead of Eq. 6.47 due to the highly reduced numerical effort. Now we can establish some empirical rules, that we will apply to determine the mechanical properties of the experimental data sets. Therefore, we need a relation between A_o, estimated using the real and imaginary part of A_2, and the estimation using the absolute value of A_2. Further, we need the

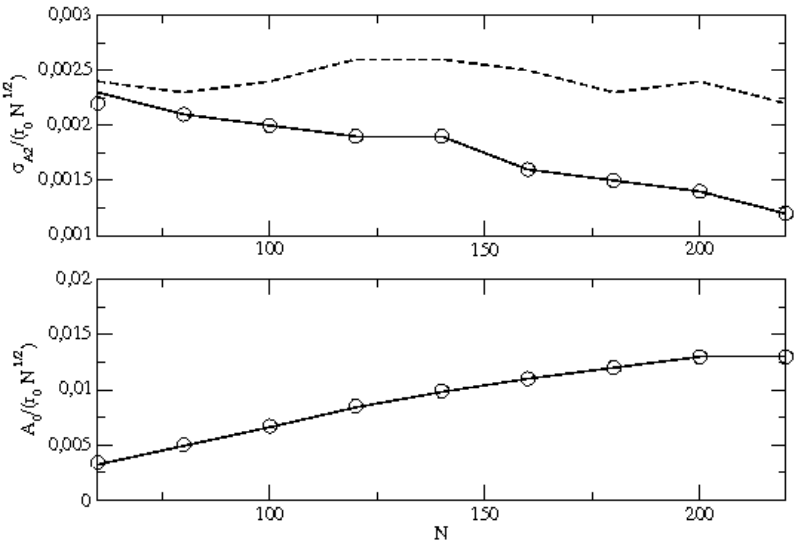

Figure 6.18: Fitting parameters of the probability distributions as shown in Figs. 6.16 and 6.17. A) $\sigma_{A_{2,re}}$ (continuous line), $\sigma_{A_{2,im}}$ (dashed line) and $\sigma_{A_{2,re}}$ (circles). B) $A^0_{2,re}$ (continuous line) and A^0_2 (circles).

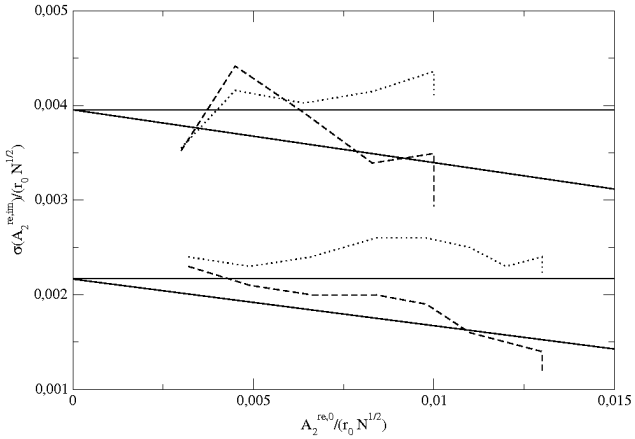

Figure 6.19: Real (dashed) and imaginary (dotted) part of the fitting parameters of the probability distributions of the Fourier coefficients A_2 as a function of the fitting parameter A_o in simulations of chains with lengths between 60 and 220 monomers. The result of simulations with two different parameter pairs are shown. Upper part: $\beta\kappa_c = 90$, $\beta\gamma = 0.3$ and lower part: $\beta\kappa_c = 300$, $\beta\gamma = 1.0$. The straight lines represent the theoretical value of σ_{A_2} as given in Eq. 6.41 and a linear fit of the simulation results using Eq. 6.47.

relation between σ_{A_2} and $\sigma_{A_{2,im/re}}$ as well as its relation to the material parameters γ and κ_c. Fig. 6.18 shows that the fitting parameters of the absolute value coincide with the fitting parameters of the real part of the Fourier coefficients. Fig. 6.19 illustrates the dependency between the mean deviation and the displacement of the real part of the Fourier coefficients. In a first approximation we find a linear relation between these two parameters. For vanishing ellipticity (A_o = 0), $\sigma_{A_{2,re}}$ should take the theoretical value as in Eq. 6.41. $\sigma_{A_{2,re}}$ then linearly decreases with increasing ellipticity,

$$\sigma_{A_{2,re}} = \sigma^0_{A_{2,re}} - c_2 A_o. \tag{6.47}$$

We have used two sets of parameters, $\beta\kappa_c = 300$, $\beta\gamma = 1$ and $\beta\kappa_c = 90$, $\beta\gamma = 0.3$ to calibrate the value of c_2. In the first case, we get $c_2 = 0.049$, in the second one we get $c_2 = 0.056$. In summary, we get the following empirical rules that we have to apply in order to calculate the models parameters κ_c and γ using only the probability distribution of the absolute value of the

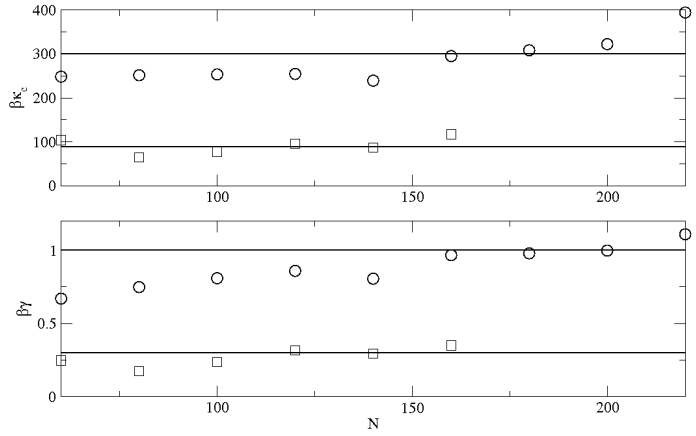

Figure 6.20: $\beta\kappa_c$ and $\beta\gamma$ as a function of the chain length for simulations done with $\beta\kappa_c = 300, \beta\gamma = 1$ (circles) and $\beta\kappa_c = 90, \beta\gamma = 0.3$ and calculated using Eqs. 6.48 and 6.49 after fitting the probability distributions of the absolute values of the Fourier coefficients A_2.

Fourier coefficients A_2 of a sample of ring configurations:

$$\beta\kappa_c = \frac{1}{72\pi^2(\sigma_{A_2} + c_2 A_o)^2} \tag{6.48}$$

$$\beta\gamma = \frac{\beta\kappa_c}{N c_1} A_o \tag{6.49}$$

with $c_1 \approx 0.021$ and $c_2 \approx 0.053$. Remains to test whether like this, we are able to extract the simulation parameters $\beta\kappa_c$ and $\beta\gamma$ from the probability distribution of the absolute values of the Fourier coefficients A_2 along these simulations. Fig. 6.20 represents the result as a function of the chain length. For the mean values over different chain lengths we get: $\beta\kappa_c = 285 \pm 48$, $\beta\gamma = 0.88 \pm 0.13$ and $\beta\kappa_c = 91 \pm 17$, $\beta\gamma = 0.27 \pm 0.06$ for simulation parameters $\beta\kappa_c = 300$, $\beta\gamma = 1$ and $\beta\kappa_c = 90, \beta\gamma = 0.3$ respectively. The actual simulation parameters lie between the error bars of the estimated parameters. We can apply this method to estimate the mechanical properties of the experimental data sets, being aware of the error that will be even larger in this case due to sparse sampling.

Analysis of experimental samples

We have used the above described method to analyse 4 samples of FtsZ polymer rings formed under different experimental conditions. The sample sizes lie between 239 rings (for FtsZ - GTP, pH6.5) and 365 rings (for FtsZ - GMPCPP) and the lengths of the rings vary between 50 and 220. An analysis of these rings for each ring length is not possible as the averages would have to be done over very sparse samples.

Fig. 6.21 shows the distribution of the ring lengths for the different samples. In order to find a balance between sparse averages and mixing of very different ring lengths, we divided each sample into two (in the case of GMPCPP three) sub-samples. Fig. 6.22 shows the distribution of $|A_2|/(\sqrt{N} r_o)$ for each sub-sample. The least mean squares fit of these distributions using Eq. 6.44 together with Eqs. 6.48 and 6.49 give an estimate of the mechanical parameters κ_c and γ of the filaments on the mica substrate under different experimental conditions. The table below summarizes these results.

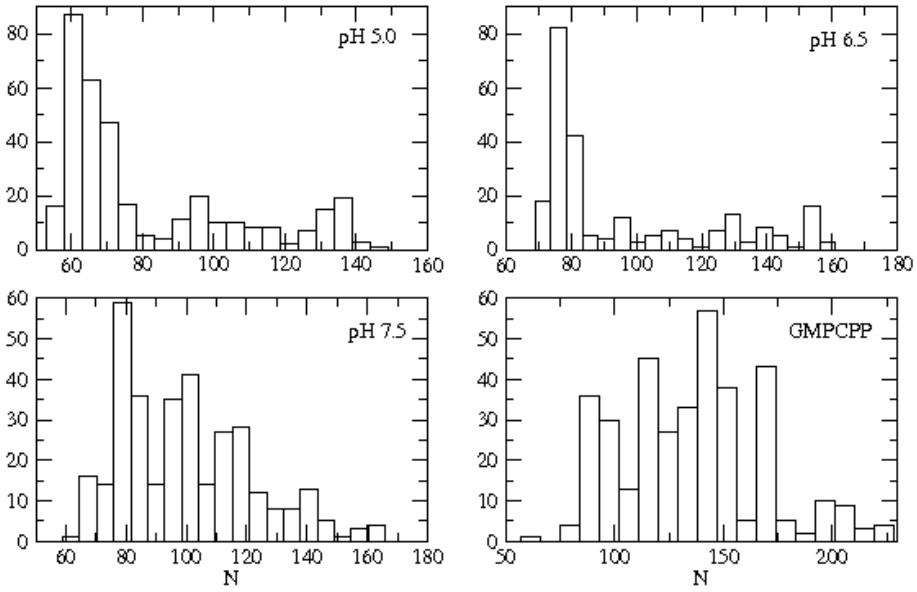

Figure 6.21.: Length distributions of samples of FtsZ filament rings for different experimental conditions.

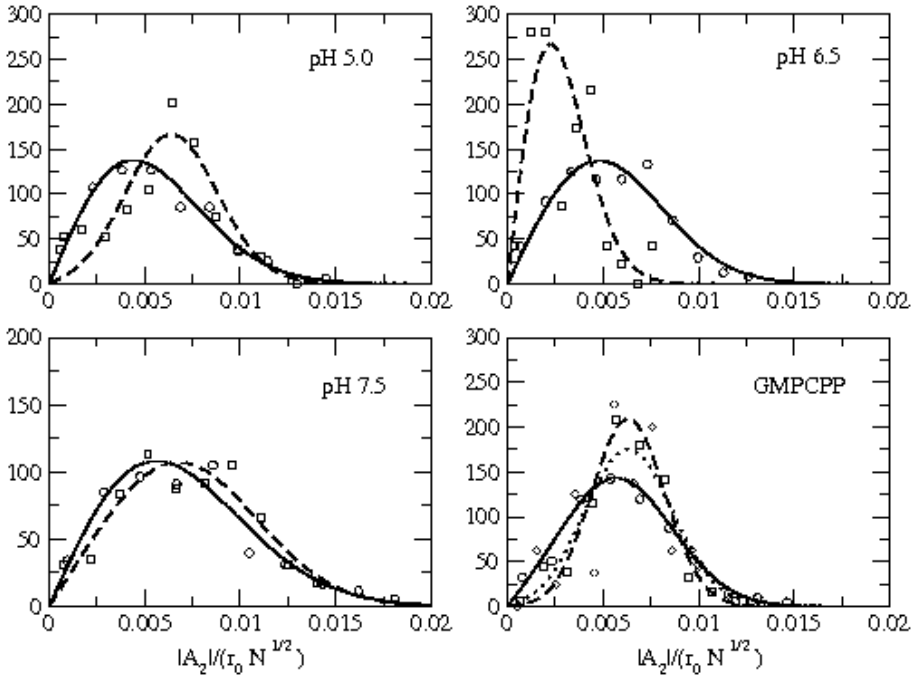

Figure 6.22.: Distribution of $|A_2|/(\sqrt{N}r_o)$ for each sub-sample defined in table 6.4.1. Circles/squares/diamonds represent the experimental data points for increasing lengths and the continuous/dashed/pointed lines the corresponding least mean squares fits using Eq. 6.44.

Apparently the results must be interpreted with a big error bar. This error is due to the mixing of different ring lengths, the resolution of the images, sparse sampling and correlation effects

pH 5.0

$N_{average}$	# of rings.	$\beta\kappa_c$	$\beta\gamma$	$\frac{\gamma}{\kappa_c}$
66 ± 6	238	72	0.0067	0.000093
114 ± 17	115	177	0.44	0.0025

pH 6.5

$N_{average}$	# of rings.	$\beta\kappa_c$	$\beta\gamma$	$\frac{\gamma}{\kappa_c}$
82 ± 11	181	97	0.21	0.0022
140 ± 12	58	272	0.0036	0.000013

pH 7.5

$N_{average}$	# of rings.	$\beta\kappa_c$	$\beta\gamma$	$\frac{\gamma}{\kappa_c}$
83 ± 9	185	45	0.00060	0.00010
120 ± 18	155	67	0.15	0.0020

GMPCPP

$N_{average}$	# of rings.	$\beta\kappa_c$	$\beta\gamma$	$\frac{\gamma}{\kappa_c}$
104 ± 13	141	128	0.29	0.0023
142 ± 8	145	271	0.55	0.0020
182 ± 18	79	196	0.3	0.0015

between subsequent images of the same ring. To get a better idea of the usable information that we can extract of the experimental data, we reproduced the experiment using simulation data. Using the length distributions of the different samples and the simulation data for rings with lengths between 60 and 220 monomers (with known parameters $\beta\kappa_c = 300$ and $\beta\gamma = 1$) we chose 5 different possible distributions for each sample (for each experimental ring with length N we randomly chose the value of A_2 along a simulation with the closest number of monomers). We then did the same analysis as before for the "real" experimental data sets and observed the following tendencies (see Fig. 6.23):

- The estimated value of $\beta\kappa_c$ lies about 30 % below its actual value and may be reproduced with an error of $\approx 10 - 20\%$. Two exceptions are the two sub-samples with less than 80 rings. Here the average estimated values of $\beta\kappa_c$ are found above its actual value and the errors are more than 50 %.
- The accuracy of the estimation does not (strongly) depend on the average size of the rings.
- The most precisely reproduced quantity is the quotient between the two material parameters, $\frac{\gamma}{\kappa_c}$. It is estimated to lie about $5 \pm 7\%$ above the actual value.

The last observation might lead to a criterion for choosing the "good" experimental samples. In the result of the analysis of the experimental data, we can clearly distinguish two groups. Samples with $\frac{\gamma}{\kappa_c} \approx 0.002$ and samples with $\frac{\gamma}{\kappa_c} < 0.0001$. Choosing only the first group and augmenting the stiffness about 30% we get the final results for the bending rigidities of the analysed rings.

Final estimation of bending rigidities of FtsZ filament rings

The best estimation for the bending rigidities of FtsZ filament rings that we could calculate for experimental AFM images under different experimental conditions is the following:
We can observe two tendencies: Lowering the pH-value seems to make the filaments stiffer. The same occurs for the insertion of the slowly hydrolyzable GTP homologue, GMPCPP. We know that in principle the pH values and the type of nucleotide affect the bond dynamics of the filaments. While monomers in GTP bonds at pH = 7.4 are exchanged every 8s [10], lower pH values

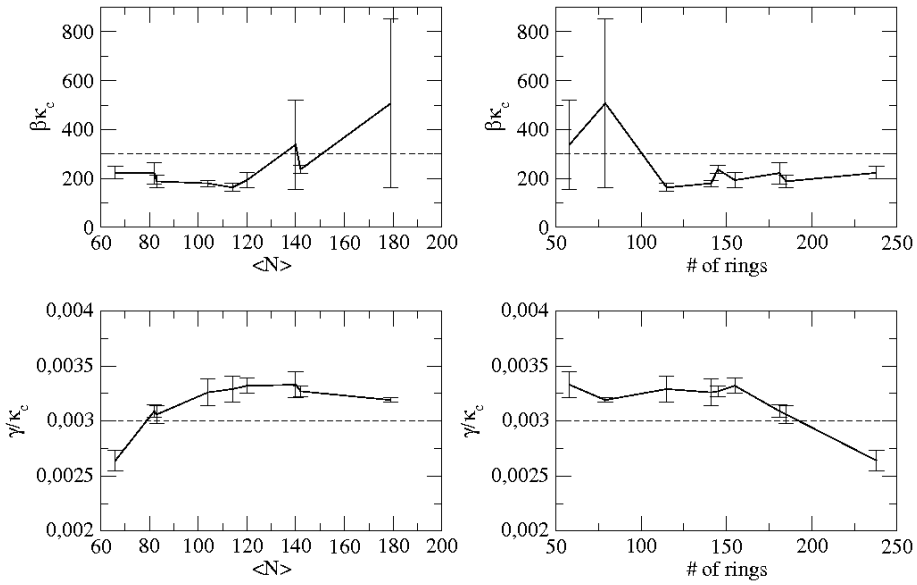

Figure 6.23.: Mean values of $\beta\kappa_c$ and $\frac{\gamma}{\kappa_c}$ for each time 5 fitted distributions of the absolute value of A_2 for randomly chosen simulation data keeping the experimental length distributions. The results are presented once as a function of the average size of the rings, $< N >$, and once as a function of the sample size.

	FtsZ - GTP, pH = 7.5	FtsZ - GTP, pH = 6.5	FtsZ - GTP, pH = 5	FtsZ - GMPCPP, pH = 7.5
$\beta\kappa_c$	90 ± 20	130 ± 30	230 ± 50	260 ± 50

Table 6.3.: Mean values of κ_c for different experimental samples.

and nonhydrolyzable nucleotides augment the bond life time. Little is known about the exact mechanism of hydrolysis, bond rupture, nucleotide and monomer exchange. For a detailed analysis of these processes, much higher resolutions in time and in space are necessary. Here we only have access to average effects of these dynamics on the global shape fluctuations of the whole ring and we can confirm the assumption that more stable bonds provide stiffer filaments. A further effect might affect the flexibility of the rings. Experiments [3] indicate, that GTP-filaments have lower spontaneous curvature than GDP chains. One might imagine, that rings with both, GTP and GDP bonds varying with the time, are more flexible than rings with constant spontaneous curvature, but simulations showed that this effect does not affect global shape fluctuations.

6.4.2. Calibration of the time scale

Low n modes, first of all A_2, show slow dynamics that can be followed in subsequent AFM snapshots. We can take advantage of this and estimate the correlation time of these global shape fluctuations and in that way calibrate the time scale of the simulations.

Correlation time in simulations

The correlation time τ for the Fourier coefficient A_2 in the simulation is defined as

$$< A_2(\Delta t + t_o)A_2(t_o) > \quad = \quad < A_2 >^2 + \left(< A_2^2 > - < A_2 >^2 \right) \exp\left(-\frac{\Delta t}{\tau} \right). \qquad (6.50)$$

We have estimated the correlation time as a function of the chain length in simulations with three different parameter pairs $\beta\kappa_c$ and $\beta\gamma$. After a first, very rough estimation of τ we simulated the rings during a time of $\approx 500\tau$ and calculated for each ring length 5000 data points, separated in time $\approx 0.1\tau$. We then used these data points to calculate mean values of $A_{2,re/im}(\Delta t + t_o)A_{2,re/im}(t_o)$ as a function of Δt. Fig. 6.24A shows the result for the real part of a ring of length N=80 and the parameters $\beta\kappa_c = 300, \beta\gamma = 1$. A least mean squares fit of the data points using Eq. 6.50 gives an estimation of the correlation time τ. Although $< A_2^2 >$ and $< A_2 >^2$ are different for the real and the imaginary part (for $\gamma \neq 0$), the correlation time should be the same. We have calculated the two values of τ as a function of the chain length for different parameter pairs (Tbl. 6.4).

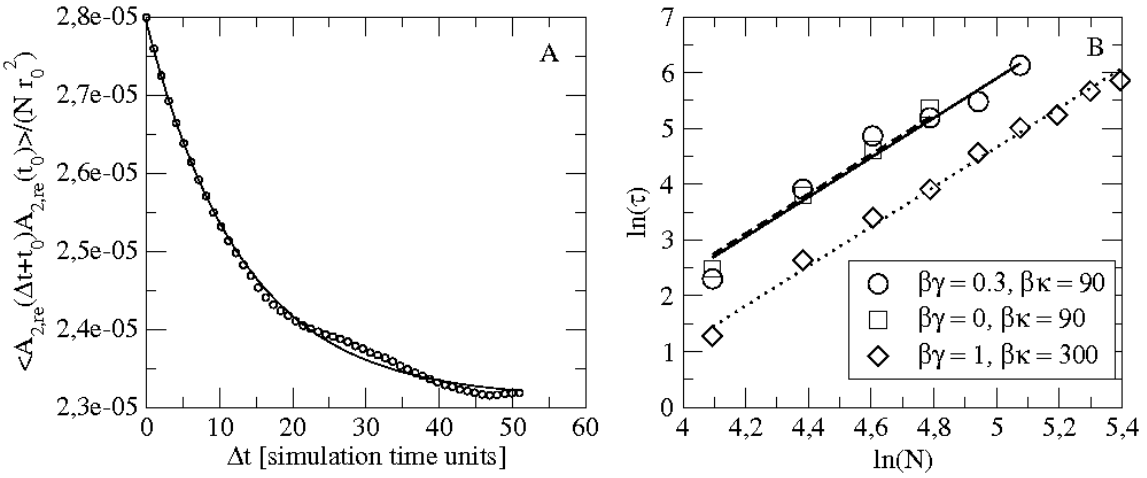

Figure 6.24.: A) $< A_{2,re}(\Delta t + t_o)A_{2,re}(t_o) >$ as a function of Δt for $N = 80, \beta\kappa_c = 300, \beta\gamma = 1$. The circles are the mean values calculated along the simulation and the straight line shows the least mean squares fit using Eq. 6.50. B) Logarithmic representation of the correlation time τ as a function of the ring length for different material parameter sets.

The correlation time of A_2 depends on the ring length and on the chain flexibility but not on the ellipticity and seems to grow linearly with $\frac{1}{\beta\kappa_c}$. The accuracy of the estimation of τ in the simulations with $\beta\kappa_c = 90$ is lower than in the simulations with $\beta\kappa_c = 300$ as we did not change the simulation time. A plot of τ as a function of N (Fig. 6.24) indicates a power law relation:

$$\tau \quad = \quad \frac{\alpha}{\beta\kappa_c} N^{\gamma}, \qquad (6.51)$$

with $\gamma \approx 3.55$ and $\alpha \approx 6.2 \cdot 10^{-4}$ simulation time units.

$\beta\kappa_c = 300, \beta\gamma = 1$

N	60	80	100	120	140	160	180	200	220
τ_{re}	3.46	13.2	29.0	52.7	90.7	131	176	300	344
τ_{im}	3.77	14.0	30.1	48.0	102	177	205	273	354
τ	3.6	14	30	50	96	150	190	290	350

$\beta\kappa_c = 90, \beta\gamma = 0.3$

N	60	80	100	120	140	160
τ_{re}	8.0	55	169	151	236	356
τ_{im}	12	44	94	200	244	566
τ	10	50	130	180	240	460

$\beta\kappa_c = 90, \beta\gamma = 0$

N	60	80	100	120
τ_{re}	13	52	89	216
τ_{im}	11	38	112	208
τ	12	45	100	210

Table 6.4.: Correlation times calculated in simulations with different parameters, κ_c and γ.

Time correlation in AFM videos of FtsZ rings

An estimation of the time correlation in AFM videos is limited by the temporal resolution of the subsequent images which is of the order of magnitude of the correlation time and by the reduced number of "long" videos where the fluctuations of one ring can be observed over time periods that allow for statistical averaging. We may only hope to get an idea about the order of magnitude of the correlation time. We have estimated the correlation time of one ring that could be observed during 141 time frames with a time separation of ≈ 1 minute. The ring belongs to the sample of FtsZ with GTP at $pH = 6.5$. We have calculated the mean value of $|A_2|(\Delta t + t_o)|A_2|(t_o)$ for Δt between 0 and 10 frames (Fig. 6.25).

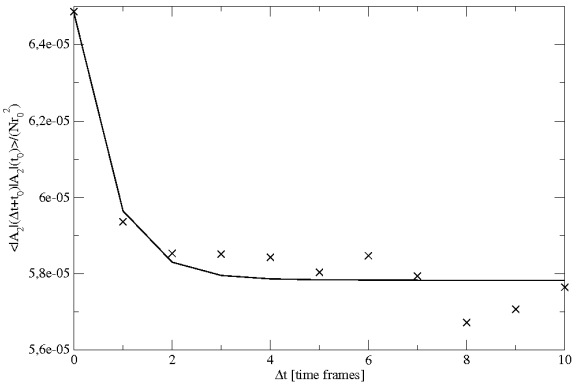

Figure 6.25.: $< |A_2|(\Delta t + t_o)|A_2|(t_o) >$ as a function of Δt for a ring of average length $N = 77$ during 141 time frames. The circles are the calculated mean values and the straight line shows the least mean squares fit using Eq. 6.50. The ring belongs to the sample of FtsZ with GTP at $pH = 6.5$.

We get $\tau \approx 0.74$ min. Before we have estimated the bending rigidity of this sample to be $\beta\kappa_c \approx 130$.

The correlation time in a simulation with these parameters ($N = 77, \beta\kappa_c = 130$) can be calculated using Eq. 6.51 and gives $\tau_{sim} = 60stu$. In that way, we obtain a very rough calibration of the time scale in our simulations:

1 simulation time unit ≈ 1 second

6.5. Formation of rings and loops

This section is focused on a series of AFM experiments where almost exclusively ring conformations were observed. In Chp. 4 we have seen that lateral attraction between filaments leads to spiral configurations. The fact that in the present experiments no spiral configurations are observed might have two reasons. No spirals were formed or all of the initially formed spirals had depolymerized before the first image was taken. The latter one would imply a special stability of ring conformations while the first one again may have two explanations. For some reason, the lateral attraction in these experiments is insignificant or the polymerization mechanism and velocity generate predominantly (almost exclusively) ring conformations. The non existence of lateral attraction in these experiments is improbable as the environmental conditions compared to the experiments described in Chp. 4 only differ in the type of nucleotide (GMPCPP or GTP instead of AlF_3) and should not have too much influence on the lateral interactions. A significant influence of the pH value should also be excluded because spirals are not observed for neither of the tested values including pH = 7.5 used in the experiments analysed in Chp. 4. We have tested the influence of the polymerization velocity on the generation of ring and spiral conformations in Langevin dynamics simulations. For these simulations we used the parameter values estimated in Chp. 4, $\beta\kappa_c = 80$, $\beta\epsilon = 0.2$ and $\theta_o = 0.042$. The mica anisotropy was not included in these simulations ($\gamma = 0$). All simulations were started with a filament of length $N = 30$. We tested two growth rates, $\nu_1 = 1\frac{1\text{mon}}{\text{stu}}$ and $\nu_2 = \frac{1\text{mon}}{10\text{stu}}$ and chose a criterion for ring formation. The tolerance for the distance between the two extremes was $0.25d$ and the angle tolerance was 0.5. At each simulation step, we checked whether a ring had been formed and when this was the case, we listed its length and started again with a 30 monomers long filament. On the other hand, we also tested whether a loop was formed. At each time step, we calculated the total lateral energy along the chain, counting a loop for $U_{lat} < -20kT$.

Fig. 6.26 shows an example of a ring and a loop configuration generated in the simulations. The criteria for ring and loop formation were chosen arbitrarily and should not change qualitatively the difference in the fraction of generated rings for different growth rates and the size distributions of the rings and spirals. The preferential curvature leads to an optimal ring length of $N = 150$. The average lengths of the rings formed in the simulations are slightly shorter, $N = 131$ for the slower growth rate, ν_1, and $N = 116$ for the faster growth rate, ν_2. For loops this tendency is vice-versa with $< N >= 198$ for ν_1 and $< N >= 218$ for ν_2. The fraction of ring formation for the slower growth rate was 18% (364 rings and 1610 spirals) and significantly higher than for the faster growth rate where only 5% (364 rings and 6730 spirals) of the filaments ended up as rings. Fig. 6.27 shows the length distributions of the rings and spirals generated in the simulations. Spirals are longer than rings and their distribution is much broader although the general shape

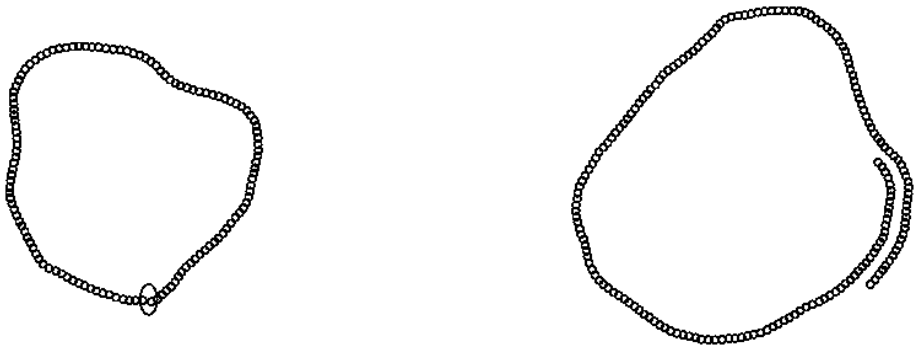

Figure 6.26.: Example of a ring and a loop conformation generated in Langevin dynamics simulations. The lengths are N=126 for the ring and N=182 for the loop.

of the distributions is similar. For short lengths it decays exponentially, the probability for the extremes to get close is limited energetically while for long filaments entropic aspects become more important and the decay is slower.

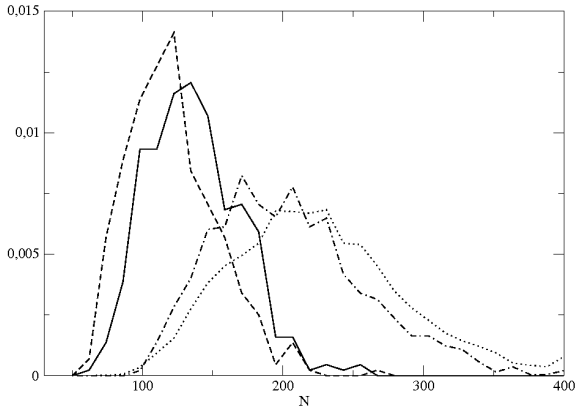

Figure 6.27.: Normalized length distributions of the rings and spirals formed in Langevin dynamics simulations. Rings: dashed line: growth rate ν_1, straight line: ν_2. Spirals: pointed line: ν_1, dashed-pointed line: ν_2. The filament growth was stopped at $N = 400$.

6.6. Conclusions

We have analyzed different sets of experimental AFM images showing shape fluctuations of stable FtsZ filament rings in depolymerization conditions. We associated fluctuations in the global ring shapes with the flexibility of individual bonds between the monomers constituting the chain. We started with a general analytical analysis of the phenomenology of ring conformations expressing the monomer positions in terms of small deviations from equilibrium radial and angular positions in a perfect circle. We found a relation between the lowest Fourier mode of the ring radius and the bending rigidity, κ_c, and confirmed these results in Langevin dynamics sim-

ulations of filament rings. We encountered technical problems as we analyzed the experimental samples due to a systematic anisotropy, probably caused by an interaction between the filaments and the substrate. Instead of beeing circular, in average the rings appeared elliptical and the estimation of the bending rigidity became more complicated and unprecise. Still we could confirm the experimentally expected tendency that decreasing pH value or nonhydrolyzable nucleotides lead to more stable and less flexible bonds. We also took advantage of the slow dynamics of the lowest Fourier mode of the ring shapes, obvious in subsequent AFM images of individual rings. Comparing the correlation time in experiment and simulation, we roughly calibrated the time scale of the simulations. We further explored in simulations the influence of the polymerization velocity on the formation of either rings or spirals and their size distributions. The ring size is, of course, dominated by the spontaneous curvature of the filaments but the size distribution of rings with slower growth rates is shifted towards smaller rings.

One interesting task for the future is the analysis of the depolymerization process of ring configurations. The AFM videos give evidence that rings are very stable structures and that their size decreases with time. Monomer-monomer bonds along the ring constantly break up and form again but from time to time during this process one monomer gets lost and the ring size becomes smaller. The ”catastrophe“ occurs when the bond can not be reestablished and the ring irreversibly breaks up in a filament with open ends. From that point on, the depolymerization process becomes very fast. The question, whether a broken bond can be built again or not depends on the concentration of GTP, the flexibility of the bond and on the diffusion that augments the distance between the two separated monomers. The diffusion process depends on whether a bond in the center of a filament, including rings, or at one of its extremes is broken. The whole process of rings that first slowly decrease in size and then suddenly break up and rapidly depolymerize is complicated and its theoretical description is still in progress. Nevertheless, its analysis might yield interesting information about the frequency of bond rupture, bond flexibility and depolymerization rates.

7. Open chain structures with protein - substrate interaction

An apparent polymorphism in the shapes adopted by FtsZ filaments on mica in recent experiments [29] can not be explained within the previous model of monomer-monomer interactions. The AFM images show a coexistence of straight and curved filaments. A possible explanation for the coexistence of populations with different curvatures might be the existence of a preferential binding site of the protein to the substrate together with a spontaneous roll curvature between monomers. In this chapter we will first analyze these new experimental samples and then present a modified model for FtsZ filaments on mica including the anchoring between monomers and substrate as well as a preferential roll curvature.

7.1. Experimental results: straight and curved filaments

Compared to the images of FtsZ filaments on mica analyzed in Chps. 4 and 6 the experimental conditions for the images in Ref. [29] are modified in a way that might enforce the anchoring between filament and substrate. A description of the experiment can be found in Chp. 3. The observed polymer shapes are similar to those described in Chp. 4, short individual filaments at low protein coverage and roll structures for higher densities. Nevertheless, a significant difference can be found for individual, short chains. In contrast to the exclusively curved structures analyzed before, here we can clearly distinguish between very straight polymers and the typical curved shapes. We can observe this tendency for 5s incubation time and relatively short chains (Fig. 7.1) as well as for 30s incubation time and longer chains, although due to the much more crowded surface less individual filaments can be characterized (Fig. 7.2).

Characterization of the filaments

To determine the length and angle distributions of the filaments marked in Figs. 7.1 and 7.2, we used the method presented in Ch. (4) and chose the degree of the reconstruction polynomial for each filament such that we got averages over $n = 8$ angles.

Filament lengths

Polymerization takes place on the mica substrate. For an incubation time of 5s (Fig. 7.1) we could extract 78 filaments with an average length of 41 ± 11 monomers. The 17 filaments marked in Fig. 7.2 have polymerized during 30s incubation time and are twice as long, $< N >= 80 \pm 22$ monomers.

Figure 7.1.: Left: Mica incubated during 5s with 80 nM FtsZ in polymerization buffer. The scale bar is 500 nm. Right: 78 individual filaments extracted from the AFM image.

Curvatures

The existence of populations with different mean curvatures becomes obvious in the distribution of the average angle between monomers in individual filaments, Fig. 7.3. A first peak at very low angles corresponds to almost straight polymers. A second peak appears further on at the value of the spontaneous curvature of the curved filaments. We have estimated the bending rigidity and the spontaneous curvature for this type of chains in the same way as for individual filaments in Chp. 4. As an approximation for separating straight and curved chains, we only included filaments with average curvatures bigger than 0.01 in the calculation. We get the following values:

incubation time	# of filaments	$< N >$	$\beta\kappa_c$	θ_o
5 s	78	41	120	0.023
30 s	17	80	80	0.039

The bending rigidity for both incubation times is similar to that estimated in Chp. 4 for filaments of FtsZ with $GDP - AlF_3$. The spontaneous curvature for the 80 monomer long filaments is also close to that found in Chp. 4 while the value for short chains is almost only half as big.

Interpretation

A possible explanation for the existence of populations with different mean curvatures might be a preferential binding site of the protein on the mica substrate together with a spontaneous roll curvature between monomers. So far, neither of these interaction terms had been included in our

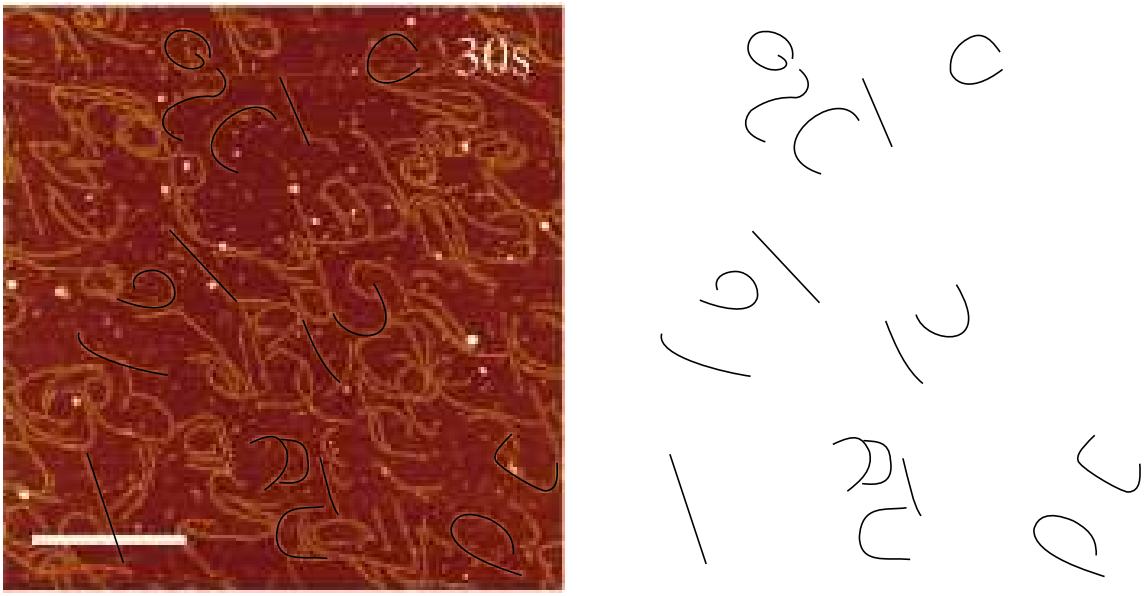

Figure 7.2.: Left: Mica incubated during 30s with 80 nM FtsZ in polymerization buffer. The scale bar is 500 nm. Right: 17 individual filaments extracted from the AFM image.

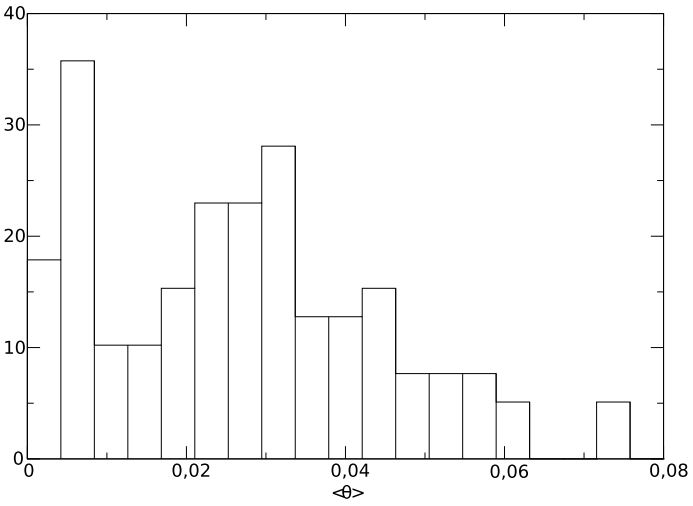

Figure 7.3: Distribution of the mean angle between monomers of individual filaments marked in Figs. 7.1 and 7.2.

model. The present experimental data do not permit a direct and quantitative estimation of the strength of these interactions although there is room for some qualitative considerations: in a first approximation, we expect a linear dependency between the roll curvature and an additional on-plane yaw curvature induced by the twist of the filament. The fact that we observe a considerable quantity of (almost) completely straight filaments may indicate, that the spontaneous yaw curvature is close to zero and corresponds to polymers without roll curvature. The observed on-plane preferential curvature in filaments is in this interpretation induced by the roll curvature of twisted polymers. Now, whether a filament is straight or curved depends on the relative strength of the above mentioned interactions. A preferential binding site of the protein on the substrate drives the chain towards a straight conformation while a spontaneous roll curvature

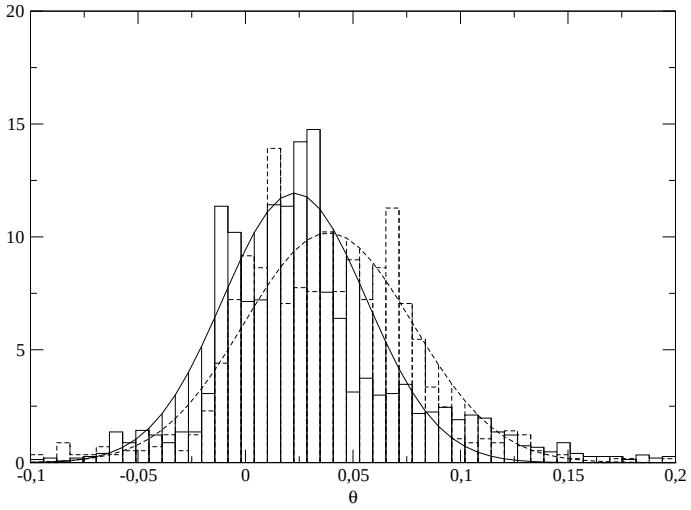

Figure 7.4: Distribution of individual angles between monomers for filaments marked in Fig. 7.1 (continuous line) and Fig. 7.2 (dashed line). Only filaments with average curvature bigger than 0.01 are included.

tends to curve the filament. The energy balance depends on the chain length, for short filaments the energy gain due to optimal protein substrate bonding will more easily compensate the cost for bending the chain away from its spontaneous roll curvature. Within this interpretation we can explain three experimental tendencies:

1. In Figs. 7.1 and 7.2 we find more straight filaments among the short chains than among the longer ones.

2. Within the curved filaments, the induced preferential yaw curvature is almost twice as high for long compared to short filaments.

3. The induced spontaneous yaw curvature is close to the spontaneous yaw curvature for filaments in Ch. (4) where we suppose a much lower anchorage between the protein and the substrate so that all filaments are free to adopt their spontaneous roll curvatures.

For a quantitative analysis of the recent experimental results, we will modify our chain model including the protein-substrate interaction and the roll curvature.

7.2. Extension of the chain model

Fig. 7.5 shows a sketch of a filament with preferential binding sites of the proteins to the mica substrate. For a filament with roll curvature it is impossible for all monomers to attach to the mica at their preferential site. The shape that the polymer adopts on the substrate will result from a balance between the cost of bending and the gain due to establishing optimal bonds between the proteins and the mica.
In order to get a qualitative estimation of the shapes that the filaments may adopt in this simple model, we use a quadratic spring bond potential to express the cost for roll bending away from a spontaneous roll curvature, ψ_o, and a cosine relation that assigns an energy gain of $\beta\gamma$ for monomers anchored to the substrate at their preferential binding site and a cost of $\beta\gamma$ for anchorage at the opposite side:

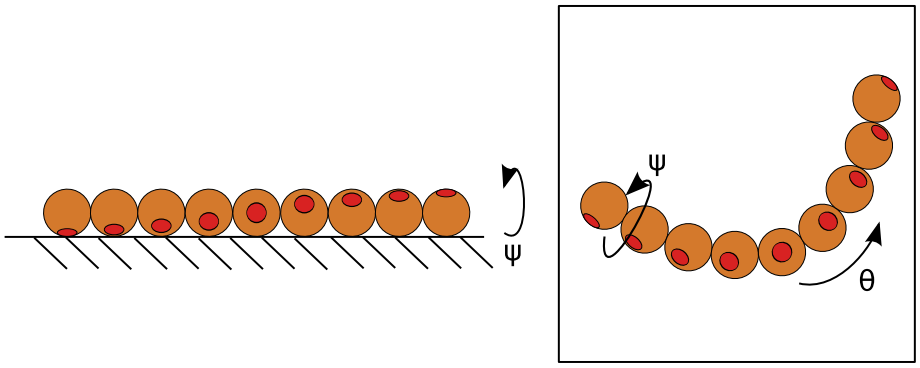

Figure 7.5.: Right: sketch of a filament attached to the mica. The preferential binding site is the dark circle. Left: bird's eye view of the filament illustrating roll (ψ) and yaw (θ) curvature.

$$U = -\gamma + 2\sum_{i=2}^{\frac{(N-1)}{2}}\left[\frac{\kappa_r}{2}\left(\psi(i)-\psi_o\right)^2 - \gamma\cos\left(\varphi_o + \sum_{j=1}^{i}\psi(j)\right)\right], \tag{7.1}$$

with κ_r being the roll bending rigidity. We assume the filament shape to be symmetric with respect to its centre and the central monomer to be anchored to the mica at an angle of φ_o with respect to its preferential binding site. Although we are not able to make quantitative predictions with this minimal representation of the protein-mica binding, it should be enough to get a qualitative idea about the competition between anchorage and bending. To facilitate the minimization of $U(\psi(i))$ with respect to the individual roll angles, $\psi(i)$, we will use a continuous description of the filament. We will replace the monomer positions i by the continuous variable x, the number of monomers N by the length of the filament L:

$$-\frac{L}{2} \le x \le \frac{L}{2}. \tag{7.2}$$

$\psi(x)$ is the roll curvature along the polymer and $\varphi(x) = \varphi_o + \int_0^x dx'\psi(x')$ is the absolute angle between the filament and the substrate counting from the centre of the filament. Derivation with respect to x relates the absolute angle and the roll curvature, $\varphi'(x) = \psi(x)$. For symmetry reasons, we get:

$$\psi(-x) = \psi(x) \quad \longrightarrow \quad \varphi'(-x) = \varphi'(x),$$

so that $\psi'(0) = \varphi''(0) = 0$. In the continuous representation, the chain energy is

$$U = \int_0^{L/2} dx \frac{\kappa_r}{2}\left(\psi(x)-\psi_o\right)^2 - \gamma\int_0^{L/2} dx' \cos\left(\varphi(x')\right). \tag{7.3}$$

The solution of the Euler equation, $\frac{\delta U(\psi(x)}{\delta\psi(x)} = 0$, is a differential equation for $\psi(x)$ that minimizes (or maximizes) the energy of the filament, U:

$$\varphi'(x) = \psi_o - \frac{\gamma}{\kappa_r}\int_x^{L/2} dx' \sin\left(\varphi(x')\right). \tag{7.4}$$

Further derivation of Eq. 7.4 gives the equation of a mathematic pendulum where x represents the time and φ the angle:

$$\varphi''(x) = \frac{\gamma}{\kappa_r}\sin\left(\varphi(x)\right). \tag{7.5}$$

The solution of this equation has to fulfill two boundary conditions:

$$\varphi'\left(\frac{L}{2}\right) = \psi_o - \frac{\gamma}{\kappa_r}\int_{L/2}^{L/2} dx' \sin\left(\varphi(x')\right) \quad = \quad \psi_o, \tag{7.6}$$

$$\sin\left(\varphi(0)\right) = \frac{\kappa_r}{\gamma}\varphi''(0) = 0 \quad \longrightarrow \quad \varphi(0) \equiv \varphi_o = 0, \pi, 2\pi, ... \tag{7.7}$$

Integration of Eq. (7.5) gives

$$\frac{1}{2}\left[\varphi'(x)\right]^2 + \frac{\gamma}{\kappa_r}\cos\left(\varphi(x)\right) = E, \tag{7.8}$$

and

$$x = \int_{\varphi_o}^{\varphi(x)} d\varphi \frac{1}{\sqrt{\left[\varphi'(0)\right]^2 + 2\frac{\gamma}{\kappa_r}\left[\cos\left(\varphi_o\right) - \cos\left(\varphi(x)\right)\right]}}. \tag{7.9}$$

For a filament of length L, we have to integrate from the centre of the filament, φ_o, to its extreme, $\varphi\left(\frac{L}{2}\right)$:

$$\varphi'\left(\frac{L}{2}\right) = \psi_o \longrightarrow \cos\left(\varphi\left(\frac{L}{2}\right)\right) = \cos\left(\varphi_o\right) - \frac{\kappa_r}{2\gamma}\left(\psi_o^2 - \left[\psi(0)\right]^2\right). \tag{7.10}$$

In terms of a pendulum, $\psi(0)$ may be interpreted as the starting velocity which determines, together with the parameters κ_r and γ, the length of the filament until reaching the final "velocity", $\varphi'\left(\frac{L}{2}\right) = \psi_o$. For $\varphi_o = 0, 2\pi, ...$ the initial roll angle, $\psi(0) = \varphi'(0)$, is smaller than the final roll angle, ψ_o, while for $\varphi_o = \pi, 3\pi, ...$ it is bigger. For each initial roll angle, $\psi(0)$, an infinite series of filament lengths fulfills Eq. 7.10. For

$$\varphi_f = \arccos\left[\cos\left(\varphi_o\right) - \frac{\kappa_r}{2\gamma}\left(\psi_o^2 - \left[\psi(0)\right]^2\right)\right], \tag{7.11}$$

we get $\varphi\left(\frac{L}{2}\right) = \varphi_f + k2\pi$ with $k = 0, 2, 4, ...$ Eq. 7.11 imposes lower and upper limits on $\psi(0)$ that depend on φ_o:

$$-2\frac{\gamma}{\kappa_r}\left(1 + \cos(\varphi_o)\right) + \psi_o^2 < \left[\psi(0)\right]^2 < 2\frac{\gamma}{\kappa_r}\left(1 - \cos(\varphi_o)\right) + \psi_o^2. \tag{7.12}$$

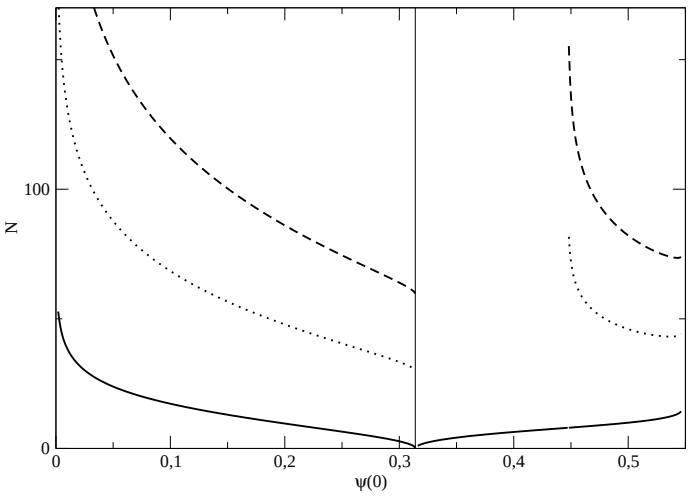

Figure 7.6: Filament length as a function of the initial roll angle, $\psi(0)$, for local minima (left of ψ_o) and maxima (right of ψ_o) of the energy. The horizontal line represents the spontaneous roll angle, ψ_o. At the left of ψ_o: $\varphi_o = 0$ at the right: $\varphi_o = \pi$. The length of the filament is determined by Eq. (7.11) and $\varphi\left(\frac{L}{2}\right) = \varphi_f + k2\pi$ with $k = 0$ (continuous lines), 2 (pointed lines) and 4 (dashed lines).

Fig. 7.6 shows the filament lengths as a function of the initial roll angle, $\psi(0)$, and the angle between the central monomer binding site and the substrate, φ_o, for k = 0, 2 and 4.
How can we interpret the dependence between filament length and initial roll angle? Let us begin with $k = 0$. For very low values of $\psi(0)$ the polymer gets infinitely long, being (almost) unrolled and anchored to the substrate at the specific binding site in the large centric region. Only towards the extremes the filament gets rolled until reaching its final curvature, ψ_o. The centric, unrolled region becomes smaller for increasing $\psi(0)$ and the filament shorter until reaching $\psi(0) = \psi_o$. $\psi(0) > \psi_o$ implies that the polymer center is anchored to the substrate at the opposite of its specific binding site ($\varphi_o = \pi$). For very short filaments, close to $\psi(0) = \psi_o$, it is obvious that this solution constitutes a local maximum of the energy as the cost for the anchorage between proteins and substrate is maximal. Calculating the total energy of the chain, we have seen that all configurations with $\varphi_o = \pi$ correspond to local energy maxima. $k = 2, 4, ...$ describe filament shapes with $1, 2, ...$ additional complete roll turns between the center and each extreme. For each filament length, we find a series of configurations that fulfill Eq. 7.5 together with the boundary conditions. All these solutions for $\varphi_o = 0$ constitute energetic minima of the polymer shape. The corresponding energies and average roll curvatures are shown in Fig. 7.7.

For the parameters that we have used in these calculations, $\beta\kappa_r = 100$, $\beta\gamma = 5$ and $\psi_o = 2\pi/20$, for short filaments up to a length of $N \approx 45$, the minimum energy configuration is that with $k = 0$. At $N \approx 45$ the global minimum "jumps" from $k = 0$ to $k = 2$, corresponding to one complete turn of the filament between its center and each of the extremes. The next "jump" from $k = 2$ to $k = 4$ takes place at a filament length of $N \approx 90$. Close to the "jumps" between different minima, the energy differences between the two configurations are small (for $N = 45 \pm 5$ we get $\Delta U < 0.3kT/\text{monomer}$), so that both shapes may coexist. For $N = 45$, in the lowest mode, $k = 0$, the average curvature of the filament, $< \psi > \approx 0.07$, is much lower than in the $k = 2$ mode where we get $< \psi > \approx 0.32$. For longer filaments, the energy differences between the different shapes and also the differences in the average roll curvature become each time smaller. The significant difference in the mean roll curvature between coexisting shapes may explain, together with the assumed linear relation between roll curvature and on-plane curvature, qualitatively the two peaks in Fig. 7.3. Fig. 7.7 illustrates the distribution of the roll curvature ψ along the filament for

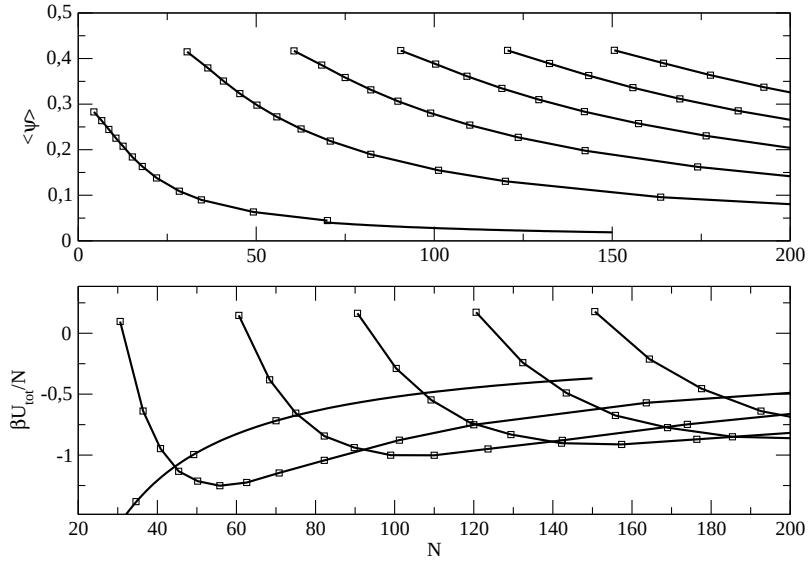

Figure 7.7.: Mean roll curvature $< \psi >$ and total energy as a function of the length of the filament. The different curves correspond to the different local minima for k=0,2,4,6,8 and 10. The first "jump" in the global minimum is found for $N \approx 44$. The parameters are: $\beta\kappa_r = 100$, $\beta\gamma = 5$, $\psi_o = 2\pi/20$

$k = 0$ and $k = 2$.

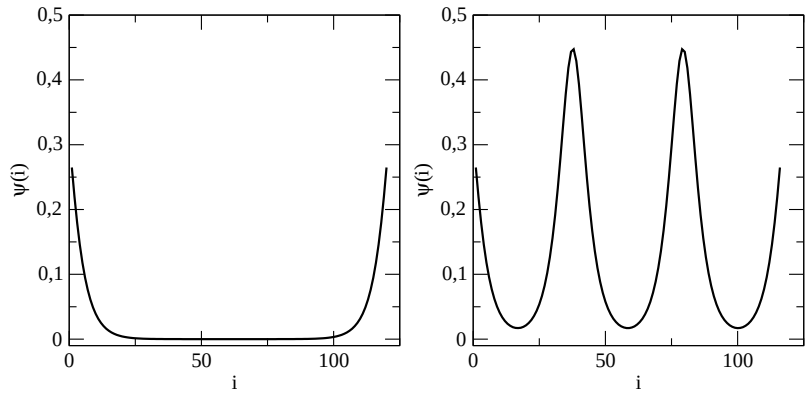

Figure 7.8.: Roll angle in a filament of $N \approx 120$ as a function of the filament length for $k = 0$ (left) and $k = 2$ (right) and the same parameters as in Fig. (7.7).

We can also make some quantitative predictions. In Fig. 7.9, we explore the influence of the spontaneous roll curvature, ψ_o, and the relation between anchorage and bending, $\frac{\gamma}{\kappa_r}$, on the energetic landscape and the filament length where the "jump" from straight to curved configurations takes place. For a constant value of ψ_o, the transition takes place at $N \approx \frac{4\pi}{\psi_o}$, almost independently of $\frac{\gamma}{\kappa_r}$ within a wide range of values. For very low (very high) values of $\frac{\gamma}{\kappa_r}$ the optimal polymer shape will be curved (straight) for all lengths (Fig. 7.9, bottom). For all values in between, the filament lengths where the transitions take place are given almost exclusively by the value of the spontaneous roll curvature. How can we estimate this value from the experimental data? About

70% of the filaments in Fig. 7.1 with a mean length of ≈ 40 monomers are curved. The transition from straight to curved filaments takes place at this monomer length for $\psi_o \approx \frac{2\pi}{20}$. For lower spontaneous roll curvatures we would expect much more straight filaments for this length. For much higher values of ψ_o, almost all filaments should be curved. Altogether, we can estimate $\psi_o \approx \frac{2\pi}{20} - \frac{2\pi}{15}$.

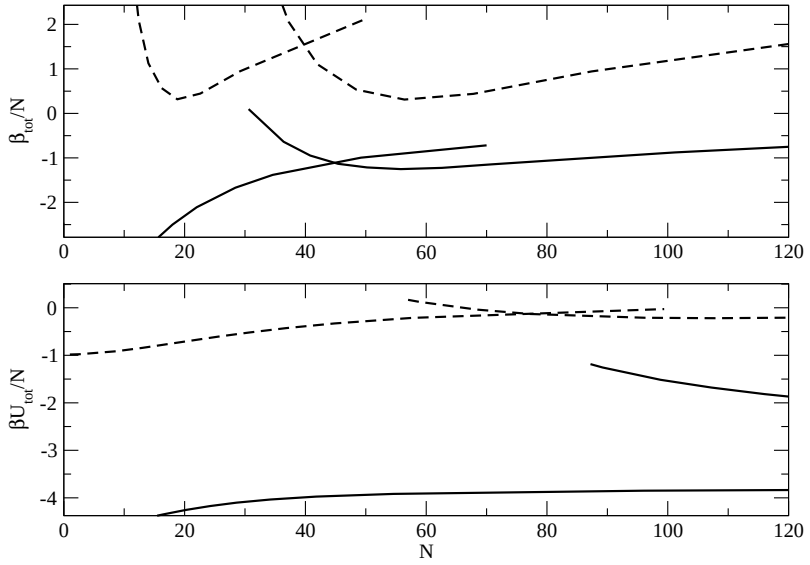

Figure 7.9.: Total energy per monomer as a function of the filament length for $\frac{\gamma}{\kappa_r} = 0.05$ (continuous lines) and $\frac{\gamma}{\kappa_r} = 0.01$ (dashed lines). Top: $\psi_o = \frac{2\pi}{20}$, bottom: $\psi_o = \frac{2\pi}{40}$. Only the $k = 0$ and the $k = 2$ modes are shown.

7.3. Conclusions

The analysis of these most recent AFM images of FtsZ filaments required an amplification of the chain model that we had used before, including the roll curvature of the polymers and the interaction protein - mica. Within this description, we could understand the apparent polymorphism in chain conformations. The appearance of straight and curved filaments can be explained by a preferential roll curvature, ψ_o, between monomers together with a preferential binding site of the monomer to the mica. The mean curvature of a filament depends in this interpretation on its length and the number of roll turns between its extremes which is zero for straight polymers. We could estimate the value of the preferential curvature in the experiments, $\psi_o \approx \frac{2\pi}{20} - \frac{2\pi}{15}$. We can not understand the observation that filaments with a mean length $N \approx 80$ are almost twice as curved as shorter filaments with $N \approx 40$. We will leave this question together with a better understanding of the relation between roll and yaw curvature and the strength of the anchorage between protein and mica for future studies.

Part II.

Membrane Deformations

8. Introduction

In the first part of this thesis, we have concentrated on the role of FtsZ filaments in the generation of the constriction force required for bacterial cell division. In this part, we will treat the reaction of the membrane under application of a radial force. Quantitative experimental data on the process of *in vivo* membrane deformation are not yet available, but recent experiments [14] allowed a fluorescent microscopy observation of the *in vitro* constriction of a free tubular liposome by a Z-ring. In the introduction, we have seen that the bacterial envelope consists of several layers, starting with the inner bacterial cell membrane. Here we will focus on the deformation of this liquid membrane where the constriction might be initiated. At the moment, little is known about how the subsequent layers interact in this process and the role of theoretical models is limited to the exploration of possible effects. The inner cell membrane consists primarily of a double layer of amphipathic phospholipids. These molecules spontaneously arrange in a way that shields the hydrophobic tails from the polar surrounding fluid and brings the more hydrophilic head region in contact with the cytosol and the outer cell wall layers. The cell membrane (in E. Coli) is rod-shaped and constitutes a closed envelope for the cytosol. The theoretical study of membrane deformations will be divided into two parts. Before we start to explore the deformation of *in vivo* membranes, we will treat the simpler and experimentally studied case of the deformation of free tubular liposomes. In both cases, we will describe the membrane in terms of the Helfrich Hamiltonian [55].

9. Theoretical description of liquid membranes: The Helfrich Hamiltonian

We have seen before that the bacterial cell wall and membrane constitute a very complex system that has to be simplified in order to be treated mathematically. The thickness of the inner bacterial membrane of *E. Coli* is about 8 nm, two orders of magnitude less than its diameter. This separation of length scales allows a description of the membrane as a two dimensional mathematical surface, embedded in the Euclidean three-dimensional space like it was done by Helfrich [55]. Within this usual Helfrich Hamiltonian, the free energy of a liquid membrane may be written as a sum of three contributions which are

- the volume, V, associated to an osmotic pressure difference Δp,
- the area, A, associated to a surface tension, σ,
- the mean and Gaussian curvatures, H and K, associated to respective bending rigidities, κ and κ_G, and a possible spontaneous mean curvature, H_o.

Here, we will concentrate on membranes that have axial symmetry and can be described by their radius, $R(z)$, being z the axis of symmetry. Concretely, we have studied two systems: free tubular liposomes where we could compare the results to a recent experimental *in vitro* study [14] and a cylindrical membrane, constrained by a rigid wall representing the inner bacterial membrane. The boundary conditions of these two systems are very different we will detail them further on in this chapter.

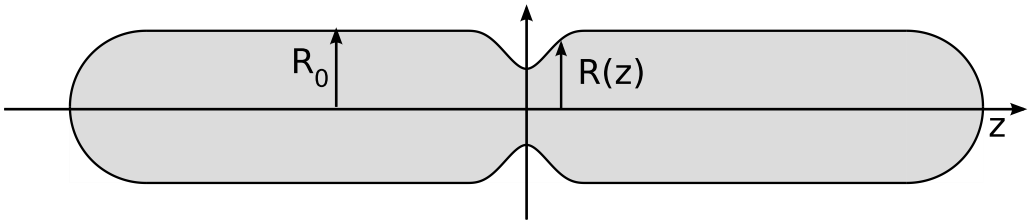

Figure 9.1.: Illustration of a deformed bacterial membrane

9.1. Volume - osmotic pressure difference

Bacteria keep a large osmotic pressure difference, Δp, of about 3-4 atmospheres between the inner cytoplasm and the external medium. Bacterial growth and division cannot be considered

as independent and it is not known, how bacteria regulate their osmotic pressure differences during these processes. By now, we can not make any quantitative estimation of the fraction of Δp that has to be compensated by volume work done by the Z-ring. In general, the osmotic pressure contribution to the free energy is

$$F_{osm} = -\Delta p V, \tag{9.1}$$

and the volume in cylindrical symmetry and as a functional of $R(z)$ is.

$$V[R] = \pi \int dz R(z)^2 \tag{9.2}$$

Here we approximate rod-shaped bacteria like *E. Coli* by a cylinder and neglect the contributions of the spherical caps at the ends. This can be justified by the fact, that we are only interested in free energy changes due to the deformation of the membrane and this deformation is localized at the center of the bacterium and vanishes at the ends. As Δp is positive, the membrane is stretched in order to increase its volume. This increase is limited by the rigid bacterial cell wall. The constriction of the membrane implies a volume reduction in the central region and therefore, unless this reduction is somehow compensated by simultaneous growth along the axial direction, volume work has to be done.

9.2. Area - surface tension

The contribution of the surface tension,

$$F_{sur} = \sigma A, \tag{9.3}$$

with $\sigma > 0$ results in a cost for increasing the membrane area. As before, we neglect the ends of the bacterium and so for a cylindrical membrane, the functional form of the area is:

$$A[R] \quad = \quad 2\pi \int dz R(z) \sqrt{1 + R'(z)^2} \tag{9.4}$$

9.3. Curvature - bending rigidity

The membrane that we describe here as a two-dimensional mathematical surface has two curvature invariants, the total curvature, H, and the Gaussian curvature, K. Within the Helfrich Hamiltonian, the curvature contribution to the membrane free energy is an expansion in terms of these two curvatures,

$$F_{curv} = \int dA \left[\frac{\kappa}{2} (H - H_0)^2 + \kappa_G K \right]. \tag{9.5}$$

H_o is the spontaneous curvature caused by the local asymmetry of the membrane. Due to the Gauss-Bonnet theorem, the integrated Gaussian curvature is topologically invariant. That means

that it does not depend on the shape of the surface and can be neglected during the division process as we will not treat here the final separation into two daughter cells and do not consider the possible formation of inhomogeneities in the composition of the membrane. The curvature contribution reduces to

$$F_{curv} = \frac{\kappa}{2} \int dA (H - H_0)^2. \tag{9.6}$$

The bending rigidity of a phospholipid bilayer, κ, is typically about 20kT. H_o is difficult to quantify, it depends on the asymmetry in the distribution of peripheral and transmembrane proteins. H is the sum of the two principal curvatures and within the axial parametrization, $R(z)$, it can be expressed as

$$H(z) \quad = \quad \frac{1}{R(z)\sqrt{1 + R'(z)^2}} - \frac{R'(z)}{(1 + R''(z)^2)^{3/2}}.$$

The membrane free energy can be summarized like

$$F_{mem} = F_{osm} + F_{sur} + F_{curv}. \tag{9.7}$$

9.4. The force ring

We are interested in membrane deformations that are caused by a constricting ring, made up of polymerized FtsZ proteins. We have discussed the formation and the aspect of the Z-ring in Chp. (5). Here, we will not take into account its internal structure, we will model its contribution to the membrane free energy as a series of line tensions centered at the site of constriction and placed between $z = -\epsilon$ and $z = \epsilon$,

$$F_{ring} = 2\pi \int_{-\epsilon}^{\epsilon} dz \left[\tau(z)\tilde{R}(z)\right]. \tag{9.8}$$

We use the function $\tilde{R}(z)$ to represent the shape of the deformation between $z = -\epsilon$ and $z = \epsilon$. The line tension density $\tau(z)$ may be considered as a Lagrange multiplier which is determined by the membrane shape. In the limit of $\epsilon \ll R_o$, the only relevant parameter should be the depth of the deformation, $\Delta = 1 - \frac{R(0)}{R_o}$. This can also be interpreted the other way around: a given ring force will cause a certain deformation depth, independent of the exact distribution of this force within a range that is small compared to the radius of the tube. Two main questions arise when we analyse the constriction of a membrane by a force ring: which shape will the deformed membrane have, and, for a given constriction force, how deep will the deformation be? These questions can be answered by finding the minimum of the free energy of the system composed of the membrane and the force ring. This free energy is given as a functional of the deformation shape, $R(z)$:

$$F[R(z), R'(z), R''(z)] = F_{mem} + F_{ring} \tag{9.9}$$

We will now analyse two concrete systems, first a free tubular liposome and then a membrane constrained by a rigid wall.

10. Free tubular liposomes with open ends

In this chapter, we will study the deformation of free tubular liposomes with open ends. We call them "free" because they are not surrounded by a limiting rigid wall like the cell wall in bacteria. The membranes have open ends and so no osmotic pressure difference between its inside and the surrounding medium can be built up. The study of the deformation of a free tubular liposome was motivated by a recent experimental study [14]. The authors could observe deformations of cylindrical liposomes under the action of a modified FtsZ protein. In these experiments, a direct connection between the membrane and FtsZ could be achieved. Therefore, the peptide that usually binds FtsA was removed and replaced by an amphipathic helix. This modified FtsZ-mts protein directly attaches to the membrane. On the other hand, large almost spherical multilamellar vesicles where made. These vesicles where brought in contact with FtsZ-mts and the result was the formation of tubular liposomes with FtsZ-mts inside. We assume that the anchoring of FtsZ-mts induces a spontaneous curvature, H_o, on the membrane which brings the initially spherical vesicles to adopt cylindrical form. The addition of the polymerizing agent GTP produced the self-assembly of FtsZ-mts rings attached to the inner side of the lamellar tubes, associated to weak indentations of the membrane. We will come back to this experiment later on in this chapter and compare its results to the theoretical predictions that we will work out now. This system differs from the *in vivo* bacterial system in two main aspects: There is no cell wall that limits the radius of the tube so that, in the undeformed state, it will adopt its equilibrium value. Furthermore, the cylindrical tube is not closed and as a consequence of its open ends, there is no osmotic pressure difference between the liposome interior and the external medium.

We will now first determine the equilibrium radius of the liposome without force ring. Then we will start to analyse small deformations caused by force rings. First, we will consider deformations caused by a single force ring and discuss the range of validity of the linear analysis. We continue with deformations caused by a periodic distribution of force rings. Finally, we will compare the theory to the above mentioned experimental results.

10.1. Liposomes at equilibrium

The equilibrium radius of the tube is related to the parameters σ, κ and H_o. In this case, the area element reduces to $dA = 2\pi R_o dz$ and the curvature to $H = \frac{1}{R_o}$. The energy of a tube of length l is

$$F_{mem}^{eq} = 2\pi R_o l \left[\sigma + \frac{\kappa}{2}\left(\frac{1}{R_o} - H_o\right)^2\right], \tag{10.1}$$

with

$$\frac{1}{R_o^2} = H_o^2 + \frac{2\sigma}{\kappa}, \tag{10.2}$$

as R_o is the radius that minimizes F_{mem}. Now that we know the shape of the liposome at equilibrium, we can add the force ring and begin with the study of small deformations. For a given tube radius, Eq. 10.2 fixes the relation between the surface tension and the spontaneous curvature,

$$\frac{\sigma}{\kappa} = \frac{1}{2}\left(\frac{1}{R_o^2} - H_o^2\right). \tag{10.3}$$

For positive surface tensions, $H_o R_o$ can take values between 0 and 1. $H_o R_o = 0$ means that the tubular shape is completely determined by the effect of surface tension whereas for $H_o R_o = 1$ the surface tension vanishes and the radius of the tube is given by the value of the spontaneous curvature.

10.2. Deformation produced by a single force ring

In the simplest case, a single force ring acts on a long tubular membrane at equilibrium and initiates its deformation. In this section we will do a linear, analytical analysis of the shape of these small deformations and the required ring forces. We will start by the definition of the relative difference between the radius of the tube and the equilibrium radius,

$$U(z) = 1 - \frac{R(z)}{R_o}. \tag{10.4}$$

This new variable, $U(z)$, is small for small deformations and we can approximate the membrane free energy functional by its quadratic form,

$$\Delta F_{mem} = \frac{2\pi\kappa}{R_o}\int dz \left[\frac{U(z)^2}{2} - R_o^2(1 - R_o H_o)U''(z) + R_o^3 H_o U(z)U''(z) + R_o^4\frac{U''(z)^2}{2}\right]. \tag{10.5}$$

We now have to minimize the functional $F[U(z), U'(z), U''(z)] = F_{mem} + F_{ring}$ in order to get the shape of the deformation, $U(z)$, and the line tension density, $\tau(z)$. The condition that the functional derivative of δF must equal zero, leads to a the following linear equations for $U(z)$ and $\tau(z)$:

$$\frac{\partial^4 U(\tilde{z})}{\partial \tilde{z}^4} + 2R_o H_o \frac{\partial^2 U(\tilde{z})}{\partial \tilde{z}^2} + U(\tilde{z}) = 0, \qquad |\tilde{z}| > \tilde{\epsilon} \tag{10.6}$$

$$\tilde{\tau}(\tilde{z}) + \frac{\partial^4 \tilde{U}(\tilde{z})}{\partial \tilde{z}^4} + 2R_o H_o \frac{\partial^2 \tilde{U}(\tilde{z})}{\partial \tilde{z}^2} + \tilde{U}(\tilde{z}) = 0, \qquad |\tilde{z}| < \tilde{\epsilon}. \tag{10.7}$$

Here we have introduced the dimensionless parameters $\tilde{z} = z/R_o$, $\tilde{\epsilon} = \epsilon/R_o$ and $\tilde{\tau} = R_o\tau/\kappa$. The function $\tilde{R}(\tilde{z}) = 1 - \tilde{U}(\tilde{z})$ represents the shape of the deformation between $\tilde{z} = -\tilde{\epsilon}$ and $\tilde{z} = \tilde{\epsilon}$. The linearized matching conditions at the borders of the force ring $\tilde{z} = \pm\tilde{\epsilon}$ are:

$$R_o H_o(\tilde{U}'(\tilde{\epsilon}) - U'(\tilde{\epsilon})) + \tilde{U}'''(\tilde{\epsilon}) - U'''(\tilde{\epsilon}) = 0, \tag{10.8}$$

$$R_o H_o(U(\tilde{\epsilon}) - \tilde{U}(\tilde{\epsilon})) + U''(\tilde{\epsilon}) - \tilde{U}''(\tilde{\epsilon}) = 0, \tag{10.9}$$

with all derivatives taken with respect to the dimensionless variable $\tilde{z}$. The finiteness and the assumption of a smooth distribution of the ring force that goes to 0 as $|z| \to \epsilon$ make all the derivatives continuous. The general solution of the fourth order differential equation, Eq. 10.6, is an exponential function with a fourth order polynomial equation that has to be solved for the exponent. We get four solutions and therewith four parameters that we determine by choosing the appropriate boundary conditions. The general solution is

$$U(z) = Ce^{\zeta z}, \tag{10.10}$$

with

$$\zeta = \pm\zeta^- \pm I\zeta^+, \tag{10.11}$$

and

$$\zeta^{\pm} = \sqrt{\frac{1 \pm R_o H_o}{2}}. \tag{10.12}$$

This can be interpreted as a linear combination of an exponentially growing and an exponentially decaying part, each modulated by a cosine with a certain phase. Far from the force ring, the membrane will adopt its equilibrium shape and the deformation vanishes. So, the exponentially growing part of the solution must also vanish and the deformation becomes

$$U(\tilde{z}) = Ce^{-\zeta^-|\tilde{z}|}\cos(\zeta^+|\tilde{z}| + \varphi_o). \tag{10.13}$$

Now, we will show that the two remaining parameters, C and φ_o, are fixed by the value of U and its first derivative at $z = 0$. Therefore, we will take the limit of vanishing force ring width. Before we can do that, we will use equations 10.7, 10.8 and 10.9 to determine the total force done by the Z-ring which is equal to the integrated line tension density, $\tau(\tilde{z})$, between $\tilde{z} = -\tilde{\epsilon}$ and $\tilde{z} = \tilde{\epsilon}$:

$$\begin{aligned} f_r = 2\pi\tau_L &= 2\pi\int_{-\epsilon}^{\epsilon} dz\tau(z) \\ &= -\frac{2\pi\kappa}{R_o}\int_{-\epsilon}^{\epsilon} dz\left[\tilde{U}(\tilde{z}) + 2R_o H_o\tilde{U}''(\tilde{z}) + \tilde{U}''''(\tilde{z})\right] \\ &= -\frac{4\pi\kappa}{R_o}\left[2R_o H_o\tilde{U}'(\tilde{\epsilon}) + \tilde{U}'''(\tilde{\epsilon})\right]. \end{aligned} \tag{10.14}$$

$\tilde{U}(\tilde{z})$ has to satisfy the matching conditions, Eqs. 10.8 and 10.9, which imply the equality of $\tilde{U}$ and U at $|\tilde{z}| = \epsilon$ up to the third derivative:

$$\begin{aligned}\tilde{U}(\tilde{\epsilon}) &= U(\tilde{\epsilon}),\\ \tilde{U}'(\tilde{\epsilon}) &= U'(\tilde{\epsilon}),\\ \tilde{U}''(\tilde{\epsilon}) &= U''(\tilde{\epsilon}),\\ \tilde{U}'''(\tilde{\epsilon}) &= U'''(\tilde{\epsilon}).\end{aligned} \tag{10.15}$$

Furthermore, for given $U(\tilde{z})$ and $U'(\tilde{z})$, the subsequent derivatives are fixed. This can be easily seen by factorizing the fourth order differential operator, Eq. 10.6, $\partial_z^4 + (2R_oH_o)\partial_z^2 + 1$ into two second order differential operators, $(\partial_z^2 + 2\xi^-\partial_z + 1)(\partial_z^2 - 2\xi^-\partial_z + 1)$. The solution of the second-order differential operator with the minus sign grows exponentially so the only physical solution is the exponentially decaying solution of the second-order differential operator with the plus sign. This operator is associated to the second order differential equation,

$$\frac{\partial^2 U(\tilde{z})}{\partial \tilde{z}^2} \pm 2\zeta^- \frac{\partial U(\tilde{z})}{\partial \tilde{z}} + U(\tilde{z}) = 0. \tag{10.16}$$

Together with Eq. 10.15, we get for the ring force:

$$f_r = \frac{4\pi\kappa}{R_o}\left[U'(\tilde{\epsilon}) + 2\zeta^- U(\tilde{\epsilon})\right]. \tag{10.17}$$

We can take the limit of vanishing ring width, $\epsilon \to 0$, so that the whole effect of the force ring is set by the depth of the deformation, $\Delta := U(0)$, and we have $U'(0) = 0$ in order to guarantee a finite value of $U'''(0)$ which is proportional to the ring force. The matching conditions at $z = 0$ are reduced to

$$2U'''(=) = \tilde{\tau}_L = \frac{\tau_L R_o}{\kappa}, \tag{10.18}$$

in terms of the total line tension, τ_L. The shape of the deformation, Eq. 10.13 becomes

$$U(\tilde{z}) = -\frac{\Delta}{\cos(\varphi_o)} \exp\left(-\zeta^- |\tilde{z}|\right) \cos(\zeta^+ |\tilde{z}| - \varphi_o), \tag{10.19}$$

with $\tan(\varphi_o) = \frac{\zeta^-}{\zeta^+}$. The generic shape of the deformation is that of a damped oscillation, ζ^- takes values between $\sqrt{2}/2$ and 0 depending on the relative importance of surface tension and spontaneous curvature. For $H_o = 0$ the membrane shape equation becomes

$$U(\tilde{z}) = -\sqrt{2}\Delta \exp\left(-\frac{\tilde{z}}{\sqrt{2}}\right) \cos\left(\frac{\pi}{4} - \frac{\tilde{z}}{\sqrt{2}}\right). \tag{10.20}$$

Here, the period of the cosine is $2\sqrt{2}\pi$. For increasing spontaneous curvature, the period becomes shorter and the decay of the deformation slower. In the limit of vanishing surface tension, $\sigma = 0$ ($R_oH_o = 1$), the oscillations in $U(z)$ become undamped as a pearling instability of the cylindrical

shape. Now, the exponential decay vanishes completely and the solution is purely periodic with a period of 2π:

$$U(\tilde{z}) \quad = \quad -\Delta \cos(\tilde{z}). \tag{10.21}$$

The shape of the deformed membrane is illustrated in Fig. 10.1.

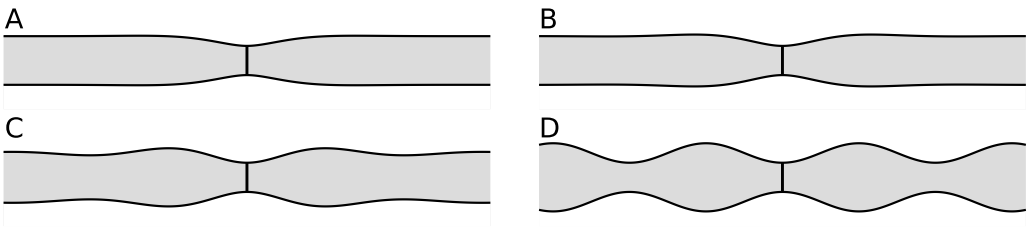

Figure 10.1.: Illustration of a liposome tube deformed by a force ring. The relative deformation depth is $\Delta = 0.4$ and the spontaneous curvature increases from A to D: A) $R_o H_o = 0$, B) $R_o H_o = 0.5$, C) $R_o H_o = 0.9$ and D) $R_o H_o = 1$.

Another consequence of taking the limit of vanishing ring width is that the contribution of the Z-ring to the free energy can be expressed as

$$F_{ring} = \oint dl\tau. \tag{10.22}$$

We can define an effective bending rigidity, κ_{eff}, so that the ring force becomes

$$f_r = \kappa_{\text{eff}} \frac{\Delta}{R_o}, \tag{10.23}$$

with

$$\kappa_{\text{eff}} = 4\pi\kappa\sqrt{2(1 - R_o H_o)}. \tag{10.24}$$

Beyond the linear analysis

The solutions that we have found for the shape of a liposome deformed by a force ring and for the deformation depth that is attained for a certain force, are valid for small relative deformations. The result of the minimization of the membrane free energy functional is a highly nonlinear fourth order differential equation that has to be solved in order to obtain the membrane shape, $R(z)$. This might be done numerically using shooting methods but we have restricted our analysis to the linearized equation which could be solved analytically. In order to get an idea of the validity of this approach, we can calculate an upper limit of the actual required force by its numerical calculation using the shape $R(z)$ determined in the linear analysis,

$$f_{r,nl} = -\frac{\partial F_{mem}}{\partial \Delta}. \tag{10.25}$$

The ring force depends on two parameters, Δ and R_oH_o. For fixed R_oH_o, of course, the error grows for increasing Δ. Fig. 10.2a shows $f_{r,nl}$ as an upper bound of the ring force as a function of Δ compared to the result of the linear approximation for $R_oH_o = 0.5$. In 10.2b, Δ is fixed to 0.28 and the force is shown as a function of R_oH_o. For small values of R_oH_o the possible non-linear effects do not change significantly the estimated force. The relative error becomes important for $R_oH_o \lesssim 1$, close to the pearling instability of the cylindrical shape. Here, the force vanishes completely in the linear estimation whereas the nonlinear upper bound remains finite.

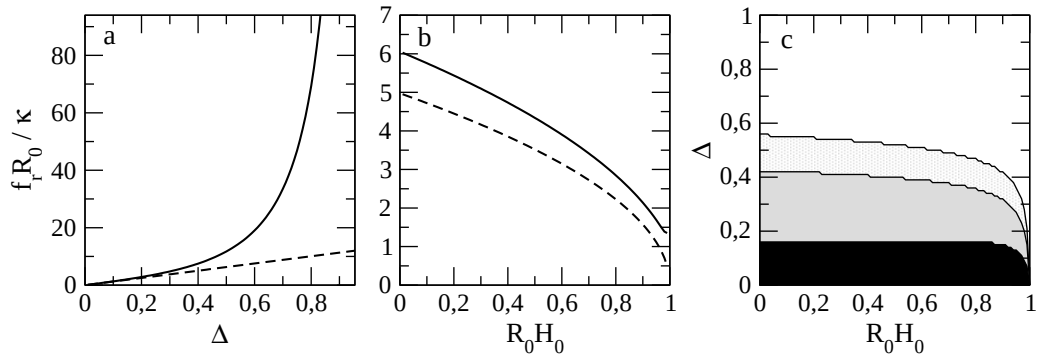

Figure 10.2.: Force required for a) a relative deformation Δ of a liposome with spontaneous curvature $R_oH_o = 0.5$ and b) a relative deformation $\Delta = 0.28$ of a liposome with spontaneous curvature R_oH_o. The dashed line is the result of the linear approximation and the continuous line gives an upper bound with non-linear effects. c) Relative maximal error in the linear estimation for different values of R_oH_o and Δ. For parameter pairs within the black (grey, light grey) region, the maximal error is 0.1 (0.5, 1).

Fig. 10.2c reflects the degree of validity of the linear approximation as a function of the spontaneous curvature and the deformation depth. The different levels of grey represent sections with growing maximal error. In summary, the linear analysis gives a reasonable estimation of the deformation force and shape for small deformations up to about 25% and spontaneous curvatures up to about $0.8R_o$.

10.3. Deformation produced by a periodic distribution of force rings

So far, we have analysed the effect of a single force ring on a cylindrical membrane. In a next step, we will study a periodic distribution of force rings along a tube, also motivated by experimental results [14] and possible future experiments. As before, we will first concentrate on theoretical predictions. Within the linear approximation, the deformation caused by a distribution of force rings is a superposition of the shifted damped oscillations produced by a single force ring. For constant ring force, the effective bending rigidity of the membrane and therewith the membrane free energy depends on the distance between rings. The rings interact with each other via the deformation that they produce on the membrane. For small distances, this interaction is attractive and individual rings, initially formed very close to each other, will collapse into a single but

stronger ring. In contrast, Z-rings that self-assemble at a large relative distance are stable keeping similar distances between neighbours along the row.

We will now have a more detailed look on the membrane shape and the effective interaction potential between Z-rings. Compared to the above system, we have to change the boundary conditions. Instead of having one force ring at $z = 0$, we set up a periodic distribution of force rings, separated by a distance $z_s R_o$ and located at $z = \frac{kz_s}{2}$ with $k = \pm 1, 2, 3, ...$ So, the new boundary conditions are

$$\begin{aligned} U\left(\pm\frac{kz_s}{2}\right) &= \Delta, \\ U'\left(\pm\frac{kz_s}{2}\right) &= 0, \end{aligned} \tag{10.26}$$

taking again the limit of vanishing ring width. Now, the exponentially growing part of the solution of Eq. 10.6 will also contribute to the shape of the membrane. We will distinguish between the general case of a membrane with finite surface tension and the limit $\sigma = 0$. For $R_o H_o < 1$, the membrane shape for $|\tilde{z}| < \frac{z_s}{2}$ can be expressed as

$$U(\tilde{z}) = 2\Delta[C^+ \cos(\zeta^+\tilde{z}) \cosh(\zeta^-\tilde{z}) + C^- \sin(\zeta^+\tilde{z}) \sinh(\zeta^-\tilde{z})], \tag{10.27}$$

with

$$C^\pm = \frac{\mp\zeta^\pm \sinh\left(\frac{\zeta^- z_s}{2}\right) \cos\left(\frac{\zeta^+ z_s}{2}\right) - \zeta^\mp \cosh\left(\frac{\zeta^- z_s}{2}\right) \sin\left(\frac{\zeta^+ z_s}{2}\right)}{\zeta^+ \sinh\left(\zeta^- z_s\right) + \zeta^- \sin(\zeta^+ z_s)}. \tag{10.28}$$

In the limit $R_o H_o = 1$, $U(\tilde{z})$ becomes

$$U(\tilde{z}) = -\frac{\Delta}{z_s + \sin(zs)} \left[\left(z_s \cos\left(\frac{z_s}{2}\right) + 2\sin\left(\frac{z_s}{2}\right)\right)\cos(z) + 2\sin\left(\frac{z_s}{2}\right) z \sin(z)\right]. \tag{10.29}$$

As before, the effective bending rigidity of the membrane is related to the third derivative of U at the location of the force ring:

$$\begin{aligned} \kappa_{\text{eff}}(z_s) &= 4\pi\kappa \frac{U'''\left(\frac{z_s}{2}\right)}{\Delta} \\ &= \begin{cases} \frac{4\pi\kappa}{R_o}\sqrt{2(1-R_o H_o)}\,\frac{\cosh(\zeta^- z_s) - \cos(\zeta^+ z_s)}{\sinh(\zeta^- z_s) + \tan(\varphi_0)\sin(\zeta^+ z_s)} & \text{for} R_o H_o < 1 \\ \frac{16\pi\kappa}{R_o}\,\frac{\sin^2\left(\frac{z_s}{2}\right)}{z_s + \sin(z_s)} & \text{for} R_o H_o = 1. \end{cases} \end{aligned} \tag{10.30}$$

As we have mentioned above, κ_{eff} is a function of the distance between the force rings, z_s. For constant ring force it is related to the membrane free energy through

$$\Delta F_{\text{mem}} = \frac{R_o^2 f_r^2}{2\kappa_{\text{eff}}}. \tag{10.31}$$

For vanishing ring separation, κ_{eff} approaches zero as it is defined as the effective bending rigidity of the membrane per period. For large values of z_s, the effective bending rigidity reaches the same value as for a single force ring. This is the limit of non interacting rings where the shape of the

membrane adopts the form of Eq. 10.19 centered at the site of each force ring. Between these two extremes, $\kappa_{\text{eff}}(z_s)$ experiences a series of exponentially decaying maxima and minima for $\sin(\zeta^+ z_s) = 0$,

$$z_s = l\pi\sqrt{\frac{2}{1 + R_o H_o}}, \tag{10.32}$$

with $l = 1, 2, ...$ For increasing relative spontaneous curvature the decay becomes less efficient and in the limit $R_o H_o = 1$ it vanishes completely. In this case, κ_{eff} approaches zero for force rings separated by a relative distance of 2π as a consequence of the pearling instability of the cylindrical shape. The membrane free energy change is represented as a function of the ring separation in figure 10.3a for different values of $R_o H_o$.

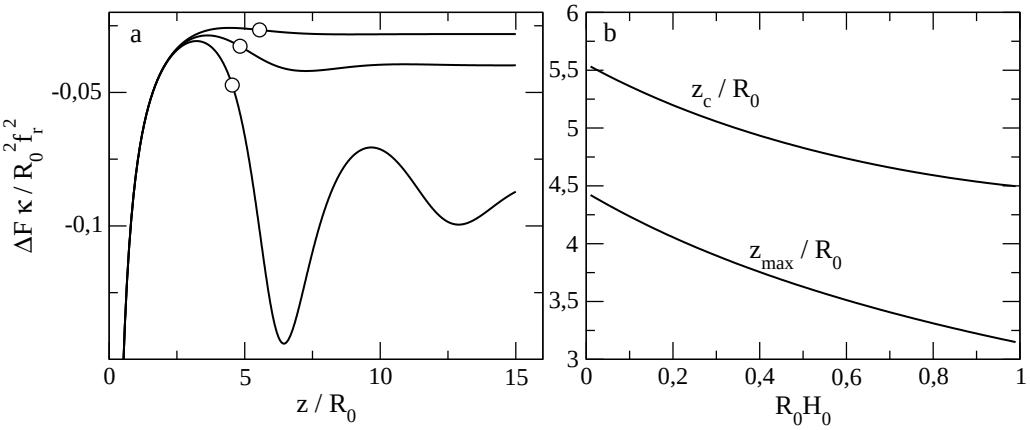

Figure 10.3.: a) Free energy change of a liposome membrane with a periodic distribution of Z-rings as a function of the ring separation for $R_o H_o = 0$ (upper line), $R_o H_o = 0.5$ (middle line) and $R_o H_o = 0.9$ (lower line). b) Distance $z_{\max}$ between periodically distributed force rings where the free energy change of the liposome has its maximum. For ring separations shorter than z_c (circles in a)) the periodic distribution is unstable and neighbour rings collapse.

For $l = 1$, κ_{eff} reaches its maximum. This means that for distances $z_s > z_{\max}$ the separation of the force rings is energetically more favorable than its approach. When we consider a distribution of rings that is limited to a finite tube, the possibility of ring separation is also limited and so the question to ask is whether the periodic distribution is stable. Therefore we imagine two rings at a distance of $z_s - d$ and its neighbour rings at a distance of $z_s + d$. We can calculate an effective bending rigidity, $\kappa_{\text{eff}}(zs, d) = \frac{1}{2}[\kappa_{\text{eff}}(zs - d) + \kappa_{\text{eff}}(zs + d)]$. For $z_s = z_{\max}$, $\kappa_{\text{eff}}(zs, d)$ has a maximum for $d = 0$. That means that the periodic distribution is unstable. For a small fluctuation in the periodicity, two neighbour rings will enter into the attractive part of the effective potential and collapse. We have to search for the critical distance, z_c, where $\kappa_{\text{eff}}(zs, d)$ has a minimum for $d = 0$. We obtain z_c by solving the transcendental equation

$$\tan(\zeta^+ z_c) = \frac{\zeta^- \sinh(\zeta^- z_c)}{\zeta^+ \cosh(\zeta^- z_c)}, \quad z_c > z_{\max}. \tag{10.33}$$

For relative spontaneous curvatures well below one, Eq. 10.33 can be approximated by:

$$z_c = z_{\max}\left(\frac{3}{2} - \frac{\varphi_0}{\pi}\right). \tag{10.34}$$

Fig. 10.3b shows this critical distance as well as $z_{\max}$ as a function of the relative spontaneous curvature. The decreasing values for growing R_oH_o reflect the decreasing period length in the damped harmonic oscillation of the membrane shape produced by a single force ring.

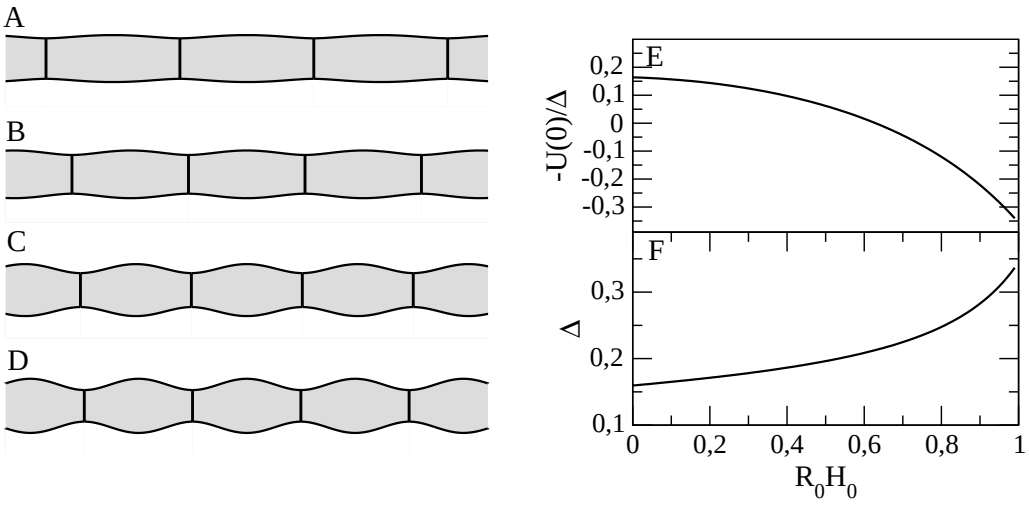

Figure 10.4.: Deformations for a tubular liposome membrane with a periodic distribution of force rings separated by its critical distance z_c for different values of the spontaneous curvature: A) $R_oH_o = 0$, B) $R_oH_o = 0.5$, C) $R_oH_o = 0.9$, D) $R_oH_o = 1$. E) Ratio of the deformation in the center between two force rings and at the site of the force rings as a function of R_oH_o. F) Deformation depth, Δ, as a function of R_oH_o for rings separated by z_c and a ring force of $3\frac{\kappa}{R_o}$

.

In summary we can say that rings, formed at small distances feel an effective attractive potential and collapse until leaving a periodic distribution with distances greater than $\approx 4.5 - 5.5R_o$, depending on R_oH_o. For z_s values between the maximum of the free energy change and the critical distance z_c the effective attraction between the rings results from the instability of the periodic distribution. If the distance between one ring and its right and left neighbours are $z_s + d$ and $z_s - d$, then the free energy change has a minimum for $d = 0$ only for $z_s > z_c$.

Figs. 10.4A-D illustrate the shapes of tubes of different spontaneous curvatures with periodic force rings separated by the critical distance z_c. For increasing R_oH_o, the force rings approach and the deformation for constant ring force becomes deeper (Fig. 10.4F). In Fig. 10.4E, we compare the depth of the deformation, Δ, to the relative difference of the membrane radius at $z = 0$ and its equilibrium radius, R_o, for rings that are separated by its critical distance as a function of the spontaneous curvature. For small values of R_oH_o, the radius of the tube is below its equilibrium value along the whole cylinder whereas for greater spontaneous curvatures, the radius of the tube between two force rings exceeds its equilibrium value. In experimental microscopy images, all these characteristics of the shape that a tubular membrane adopts when one or more force rings exert force on it may be analyzed and used to determine the importance of the spontaneous curvature and finally the ring force. At the moment, there is still a lack of detailed experiments

with controlled boundary conditions but as we have mentioned at the beginning of this chapter, the study of free tubular liposomes was motivated by one concrete experimental study [14] and we can now compare our theoretical predictions to these experimental results.

10.4. Theoretical predictions and experimental results

We will divide the analysis of the experimental data into two parts. We will first focus on a tube region, deformed by an individual force ring and then interpret a longer tube section with a series of indentations.

10.4.1. Deformation produced by a single Z-ring

In principle, the image of a liposome tube deformed by a single force ring contains all the information that we need in order to determine the spontaneous curvature of the tube, and, if we know the bending rigidity of the membrane, the force needed to obtain the constriction. Therefore, we have to measure three quantities: The equilibrium radius of the undeformed tube, R_o, as well as the minimal and the maximal radius of the deformed tube. The deformation that is given by Eq. 10.19 is maximal for $\tilde{z}_{\mathrm{m}} = \frac{\pi}{\zeta^+}$,

$$U(\tilde{z}_{\mathrm{m}}) \quad = \quad \Delta \exp\left(-\pi\sqrt{\frac{1-R_oH_o}{1+R_oH_o}}\right). \tag{10.35}$$

So, the spontaneous curvature of the membrane is:

$$R_oH_o \quad = \quad \frac{1-\left[\frac{1}{\pi}\ln\left(\frac{U(\tilde{z}_{\mathrm{m}})}{\Delta}\right)\right]^2}{1+\left[\frac{1}{\pi}\ln\left(\frac{U(\tilde{z}_{\mathrm{m}})}{\Delta}\right)\right]^2}, \tag{10.36}$$

and the constriction force is given by Eqs. 10.23 and 10.24,

$$f_r = 4\pi\kappa\sqrt{2(1-R_oH_o)}\,\frac{\Delta}{R_o}. \tag{10.37}$$

Fig. 10.6 shows a tubular liposome constricted by a force ring. In this image, it is not possible to measure the equilibrium radius of the tube because within the dimensions of the photo, the liposome remains deformed. However, we can extract R_o from figure 10.7 which shows the same liposome at a later stage where the deformation has vanished due to the continuous reduction of GTP concentration.

There are mainly three reasons that make it difficult to determine the different radii with an accuracy that allows a quantitative estimation of the spontaneous curvature: the multilamellar membrane is about 1000 phospholipid bilayers thick. That means that its thickness is of the same order of magnitude as the tube diameter. The treatment of the membrane as a mathematical surface becomes problematic as well as the determination of R_o. Further, the liposome is not a rigid cylinder, the tube itself is bended. And, at last, the force ring shown in Fig. 10.6 is not really an

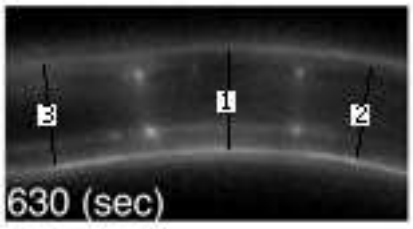

Figure 10.5.: Undeformed liposome tube

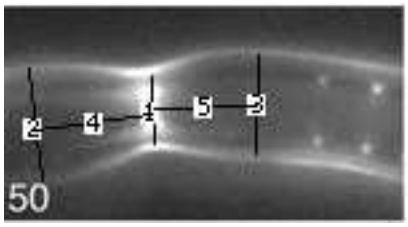

Figure 10.6.: Liposome tube deformed by a force ring

isolated single force ring, on its right further filaments, although apparently less effective, appear. As a conclusion, at least for the moment, we will have to settle for a qualitative comparison of theoretical predictions and experimental results, expecting future experiments to allow more precise calibration. The family of predicted shapes, Fig. 10.1, is in good qualitative agreement with the microscopy image, Fig. 10.6. The multilamellar membrane is built of about 1000 phospholipid bilayers. Assuming a contribution of 20kT from the bending rigidity of each bilayer and a tube radius, R_o, of approximately 1.8μm, the maximum force, required for a relative deformation $\Delta \approx 0.2$, is 180pN in the linear approximation. The possible non-linear effects do not change this estimation since they are relatively important only for $R_o H_o \lesssim 1$ where the predicted force is well below this linear upper bond (Fig. 10.2).

10.4.2. Multiple rings along a tube

Another testable theoretical prediction is the interaction of several force rings along a tube. We have seen above that rings, located at distances shorter than about $4 - 6R_o$ attract each other and finally collapse until leaving a sparser periodic and stable distribution. Fig. 10.7 shows the time evolution of a liposome that contains FtsZ-mts and GTP. In the piece of the tube shown in the photos, initially about 30 rings were built. During about 300 seconds, these rings slide forth and back along the liposome and end up by collapsing into approximately 10 brighter rings. This sparser distribution remains stable over a period of 300 seconds. Hence, the experiment supports, qualitatively the theoretical predictions.

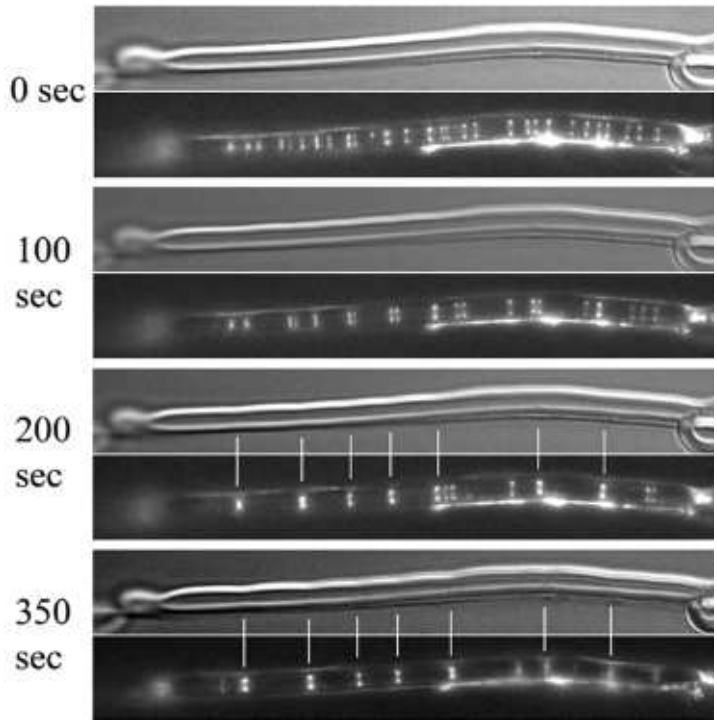

Figure 10.7.

10.4.3. Conclusions

We have seen that the experiments done with liposomal tubes are in good qualitative agreement with our theoretical predictions and that it is possible to estimate the order of magnitude of the applied constriction force. A better characterization of the liposome would be helpful. This could be achieved by the generation of liposomes made up of only a few phospholipid bilayers, so that the different radii can be measured more precisely and by the isolation of single force rings in order to relate cause and effect of the applied force. Further, it would be interesting to study the dependency of the *in vitro* factors controlling the polymerization of FtsZ protein monomers and the generation of force. Of course, the *in vitro* study of membrane constriction caused by Z-rings offers unique possibilities to determine the relevant factors that determine force generation and membrane deformation. However, the actual goal should be to understand the constriction *in vivo*, inside the bacteria. So, we will now have a look on how we have to adapt our theoretical model so as to describe the inner membrane of cylindrical bacteria.

11. Free tubular liposomes with osmotic pressure difference

Although in principle we are interested in the effect of osmotic pressure difference due to its presence in bacteria where the inner radius of the membrane is limited by a rigid cell wall, we will include this chapter where we introduce an osmotic pressure difference in a free tubular membrane. As before, we will start with some considerations about the stability of a free closed tubular membrane with osmotic pressure difference between its interior and the external medium.

11.1. Equilibrium and stability

The equilibrium free energy of the membrane is like in Eq. 10.1 adding the volume term,

$$F_{mem}^{eq} = 2\pi R_o l \left[\sigma + \frac{\kappa}{2} \left(\frac{1}{R_o} - H_o \right)^2 - \frac{1}{2} \Delta p R_o \right]. \tag{11.1}$$

The relation that we find for the equilibrium radius is now

$$\tilde{\sigma} = \frac{1}{2} \left(1 - R_o^2 H_o^2 \right) + \Delta \tilde{p}. \tag{11.2}$$

with $\tilde{\sigma} = \frac{\sigma R_o^2}{\kappa}$ and together with the condition,

$$\Delta \tilde{p} = \frac{\Delta p R_o^3}{\kappa} < 1. \tag{11.3}$$

The membrane radius is fixed by the relation between osmotic pressure difference, spontaneous curvature and surface tension. For $\Delta \tilde{p} > 1$, R_o instead of being the equilibrium radius of the tube is its critical radius. The free energy has then a maximum instead of a minimum for $R(z) = R_o$ and a stable tube can not be formed. Tubes with $R(z) < R_o$ shrink further on as the energy gain due to area reduction exceeds the cost of volume work. Tubes with $R(z) > R_o$ instead keep blowing up because the surface tension is not able to compensate the osmotic pressure. For relative osmotic pressure differences greater than one, free tubes are not stable and can only exist within a limiting rigid wall with $R_w < R_o$. We will restrict our further analysis to positive surface tensions and positive spontaneous curvatures.

11.2. Deformation caused by a force ring

As before for $\Delta\tilde{p} = 0$ we will analyze small deformations and approximate the free energy functional by its quadratic form,

$$\begin{aligned} \Delta F_{mem} &= 2\pi\kappa \int d\tilde{z} \left[(1-\Delta\tilde{p}) \frac{U(\tilde{z})^2}{2} - (1 - R_o H_o) U''(\tilde{z}) + R_o H_o U(\tilde{z}) U''(\tilde{z}) + \right. \\ &\quad \left. \Delta\tilde{p} \frac{U'(\tilde{z})^2}{2} + \frac{U''(\tilde{z})^2}{2} \right]. \end{aligned} \tag{11.4}$$

Here we have used Eq. 11.2 to replace $\tilde{\sigma}$. Including the volume term, the linearized shape equation, Eq. 10.6, is modified to

$$\frac{\partial^4 U(\tilde{z})}{\partial \tilde{z}^4} + \beta \frac{\partial^2 U(\tilde{z})}{\partial \tilde{z}^2} + \alpha U(\tilde{z}) = 0. \tag{11.5}$$

For fixed equilibrium radius, R_o, α and β depend on the choice of the two independent material parameters:

ind. par.	$H_o R_o, \Delta\tilde{p}$	$\sigma, \Delta\tilde{p}$	$H_o R_o, \tilde{\sigma}$
α	$1 - \Delta\tilde{p}$	$1 - \Delta\tilde{p}$	$1 - \tilde{\sigma} + \frac{1}{2}(1 - H_o^2 R_o^2)$
β	$2H_o R_o - \Delta\tilde{p}$	$2\sqrt{1 - 2(\tilde{\sigma} - \Delta\tilde{p})} - \Delta\tilde{p}$	$2H_o R_o - \tilde{\sigma} + \frac{1}{2}(1 - H_o^2 R_o^2)$

The solution is Eq. 10.10 with

$$\zeta = \pm\sqrt{-\frac{\beta}{2} \pm \frac{\sqrt{\beta^2 - 4\alpha}}{2}}. \tag{11.6}$$

The actual form of this solution depends on the relative importance of surface tension, spontaneous curvature and osmotic pressure difference. We now find three different regions. For small values of $R_o H_o$ and relatively high values of $\Delta\tilde{p}$ and $\tilde{\sigma}$, the deformation decays purely exponentially. For relatively low values of the osmotic pressure difference we find, as before for vanishing $\Delta\tilde{p}$, an exponentially decaying oscillation. This exponential decay vanishes for growing values of the spontaneous curvature and close to the limit of stability, $\Delta\tilde{p} = 1$, ending up in the broad region of pearling instability of the cylindrical shape (Fig. 11.1).

11.2.1. Exponentially decaying region

The deformation of the membrane decays purely exponentially for

$$\beta^2 - 4\alpha > 0, \quad \alpha > 0, \quad \beta < 0. \tag{11.7}$$

This corresponds to the black regions in Fig. 11.1. The shape of the membrane is

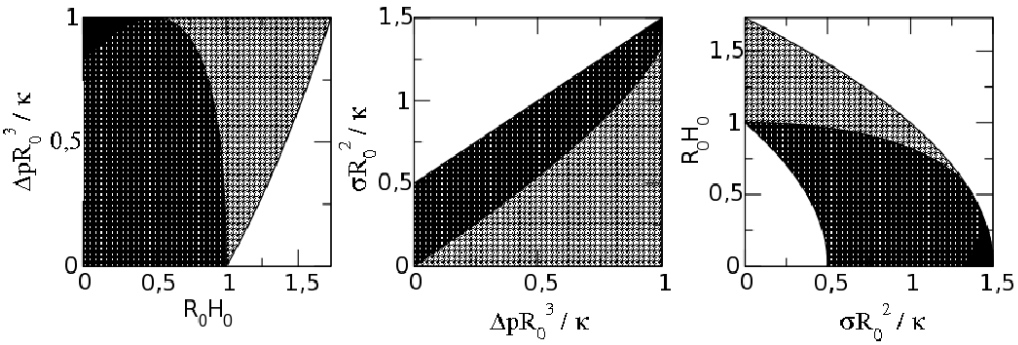

Figure 11.1.: Representation of the different regions of membrane deformation. Black: purely exponential decay, dark grey: exponentially decaying oscillation, grey: pure oscillation, white: parameter regions with A) negative surface tension, B) negative spontaneous curvature and C) $\Delta\tilde{p} < 0$ or $\Delta\tilde{p} > 1$.

$$U(\tilde{z}) = \Delta\left(\frac{\zeta^+}{\zeta^+ - \zeta^-}\exp(-\zeta^-|\tilde{z}|) + \frac{\zeta^-}{\zeta^- - \zeta^+}\exp(-\zeta^+|\tilde{z}|)\right), \tag{11.8}$$

with

$$\zeta^\pm = \sqrt{-\frac{\beta}{2} \pm \frac{\sqrt{\beta^2 - 4\alpha}}{2}}, \tag{11.9}$$

and the ring force, $f_r = \kappa_{\text{eff}}\frac{\Delta}{R_o}$, with effective bending rigidity,

$$\kappa_{\text{eff}} = 4\pi\kappa\zeta^+\zeta^-(\zeta^+ + \zeta^-). \tag{11.10}$$

11.2.2. Region of exponentially decaying oscillation

For

$$\beta^2 - 4\alpha < 0, \quad \alpha > 0, \tag{11.11}$$

the force ring causes an oscillating deformation that decays exponentially. The shape of the deformed membrane is the same as in Eq. 10.19, with generalized $\zeta^\pm$ to include the osmotic pressure difference,

$$\zeta^\pm = \frac{1}{2}\sqrt{2\sqrt{\alpha} \pm \beta}. \tag{11.12}$$

The effective bending rigidity becomes

$$\kappa_{\text{eff}} = 8\pi\kappa\zeta^-\left(\left(\zeta^+\right)^2 + \left(\zeta^-\right)^2\right). \tag{11.13}$$

11.2.3. Region of pearling instability

For vanishing osmotic pressure difference and $H_o R_o = 1$, we found a pearling instability of the cylindrical shape. The exponential decay vanishes completely and a single force ring causes an oscillating deformation along the whole length of the membrane tube. Now, this instability is found for all

$$\beta^2 - 4\alpha > 0, \quad \alpha > 0, \quad \beta > 0. \tag{11.14}$$

In all three cases, we assume positive values for the surface tension, the spontaneous curvature and the osmotic pressure difference. The shape of the deformation is

$$U(\tilde{z}) = \Delta \cos(\zeta^{\pm} \tilde{z}). \tag{11.15}$$

In the linear approximation, the energy cost of the deformation and therewith κ_{eff} is zero and there are two solutions for the period of the oscillation, $\frac{\zeta^{\pm}}{2\pi}$, with

$$\zeta^{\pm} = \sqrt{\frac{\beta}{2} \pm \frac{\sqrt{\beta^2 - 4\alpha}}{2}}. \tag{11.16}$$

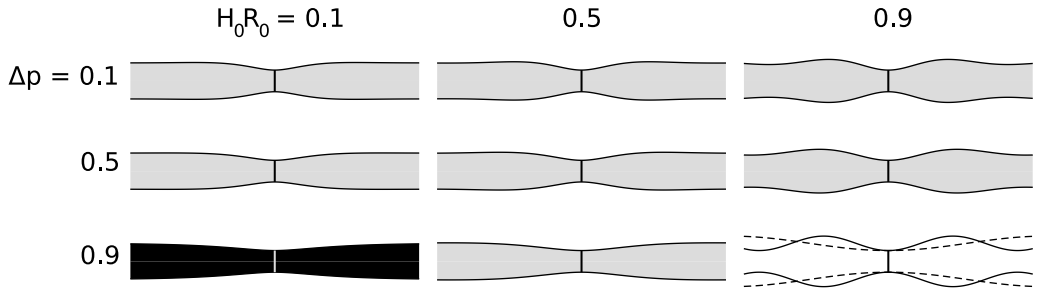

Figure 11.2.: Shape of a membrane with relative deformation $\Delta = 0.4$ for different parameter sets. For $\Delta\tilde{p} = 0.9$ the whole spectrum of qualitatively different deformations is found for $H_o R_o$ growing from 0.1 to 0.9. In the bottom right image, the two different periods of the oscillating deformation are represented (dashed line: $\frac{\zeta^+}{2\pi}$, continuous line: $\frac{\zeta^-}{2\pi}$).

Fig. 11.2 gives an overview of how the shape of the deformation depends on the material parameters. The amplitude of the oscillation grows for growing spontaneous curvature and the exponential decay becomes slower for high osmotic pressure differences, vanishing completely when the limit of pearling instability is reached.

11.2.4. Dependency of the effective bending rigidity of the membrane on $R_o H_o$, $\Delta\tilde{p}$ and $\tilde{\sigma}$

The effective bending rigidity of a membrane with equilibrium radius R_o, depends on the relative importance of the material parameters that are responsible for the formation and stability of the

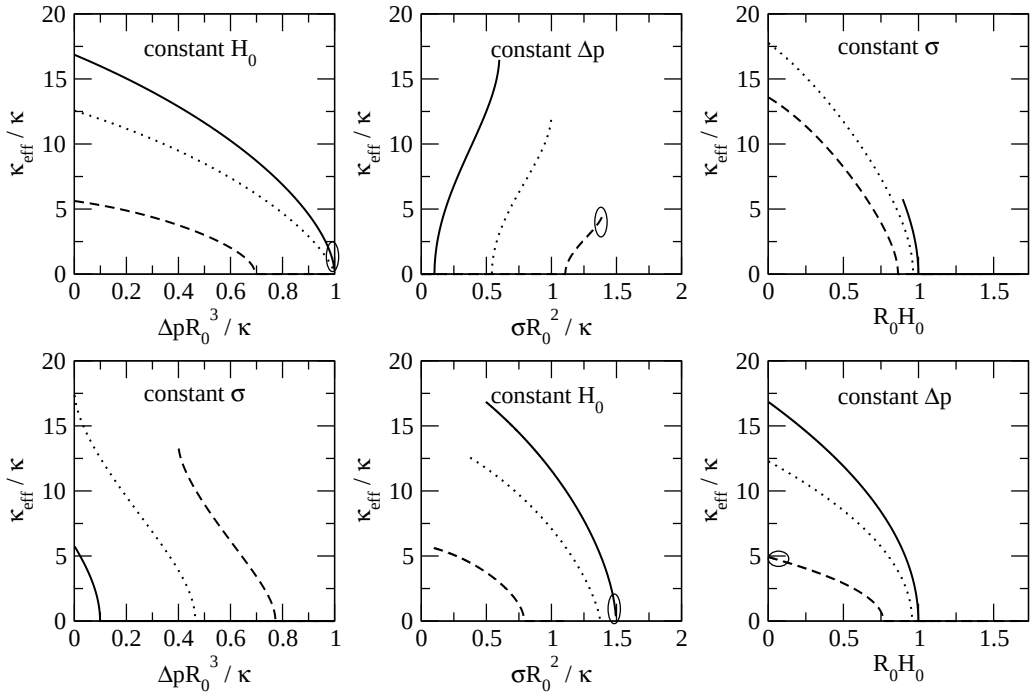

Figure 11.3.: Effective bending rigidity of the membrane as a function of the osmotic pressure difference (left), the surface tension (middle) and the spontaneous curvature (right). The continuous (pointed, dashed) lines correspond to the indicated constant parameter equal 0.1 (0.5, 0.9). Ellipses indicate regions of purely exponentially decaying deformations.

tube. This dependency is represented in Fig. 11.3. In this figure, we fix one of the three parameters and represent the effective bending rigidity as a function of a second parameter which leaves the third one also fixed. For constant spontaneous curvature, the bending rigidity decreases for increasing osmotic pressure difference and surface tension as the membrane is getting closer to instability ($\Delta\tilde{p} \to 1$). For constant osmotic pressure difference, we find the same situation as before for $\Delta\tilde{p} = 0$. Increasing $R_o H_o$ implies lower $\Delta\tilde{\sigma}$ and lower bending rigidity, ending up in a region of pearling instability for high enough values of the spontaneous curvature. This limit decreases for growing $\Delta\tilde{p}$. Finally, for constant surface tension, the membrane becomes softer for increasing values of $\Delta\tilde{p}$ and $R_o H_o$. The non-zero values in Fig. 11.3 correspond to the exponentially decaying oscillating region, except for the marked pieces which indicate purely exponential decay close to the limit of instability of the membrane.

11.3. Conclusions

In this chapter, we explored the effect of an osmotic pressure difference between the interior of a membrane tube and the surrounding medium on its deformation properties. We found that the cylindrical membrane shape is only stable for relative osmotic pressure differences, $\Delta\tilde{p} = \frac{\Delta p R_o^3}{\kappa}$, smaller than one. Within a linear analysis, we distinguish regions with qualitatively different deformations. For low values of the osmotic pressure difference the force ring causes, as before,

an exponentially decaying, oscillating deformation. For increasing values of $\Delta\tilde{p}$ together with high surface tension and low spontaneous curvature, the oscillation vanishes and the decay of the deformation becomes purely exponentially. The region of pearling instability of the cylindrical shape is no longer reduced to the strict condition $H_o R_o = 1$, the deformation of the membrane is now purely oscillatory in a wide region of high spontaneous curvature, high osmotic pressure difference and low surface tension. The effective rigidity of the membrane is determined by the relative importance of $\Delta\tilde{p}, \Delta\tilde{\sigma}$ and $H_o R_o$. Tubes with fixed radius R_o become less rigid for increasing spontaneous curvature and osmotic pressure difference. Now that we have studied the deformation of a free membrane with osmotic pressure difference, we will include the effect of a surrounding rigid wall.

12. Membrane deformations within a rigid wall

In this chapter, we will study the deformation that a single force ring produces on a cylindrical membrane limited by a rigid wall, reflecting the inner bacterial membrane surrounded by the cell wall. This introduces the new boundary condition $R(z) < R_w$ that we assume to be the only effect of the wall.

12.1. Stability

The equilibrium radius of the membrane is still given by Eq. 11.2. So, the radius of a limiting wall must be smaller than R_o, $R_w = R_o$ representing the case of a membrane at equilibrium, limited by a rigid wall. We will introduce a new parameter, ξ, which is a measure of the difference between R_o and R_w,

$$\xi = \frac{1}{2} - R_w^2 \frac{\sigma}{\kappa} - \frac{1}{2} R_w^2 H_o^2 + \Delta\tilde{p}.$$

The criterion $R_w \leq R_o$ becomes $\xi \geq 0$. Before, we have seen that a cylindrical membrane with $\Delta\tilde{p} \geq 1$ can not exist. Now, this is no longer true as the limiting rigid wall impedes its expansion.

We will go on with the general solution of the modified shape equation. We will then continue by a more detailed study of two specific cases: vanishing osmotic pressure difference, $\Delta p = 0$, and very large osmotic pressure differences, $\Delta p \gg 0$. Finally, we will make some assumptions about the relevant parameters *in vivo* and the forces needed to constrict the inner bacterial cell membrane.

12.2. General linear analysis of the membrane shape equation

As in general (for $\xi > 0$) the membrane is no longer at equilibrium before the deformation process starts, we have to include the stability parameter ξ into the quadratic form of the membrane free energy,

$$\begin{aligned} \Delta F_{mem} &= 2\pi\kappa \int d\tilde{z} \left[\xi U(\tilde{z}) + (1 - \Delta\tilde{p}) \frac{U(\tilde{z})^2}{2} - (1 - R_w H_o) U''(\tilde{z}) + \right. \\ &\quad \left. R_w H_o U(\tilde{z}) U''(\tilde{z}) + (\xi + \Delta\tilde{p}) \frac{U'(\tilde{z})^2}{2} + \frac{U''(\tilde{z})^2}{2} \right]. \end{aligned} \tag{12.1}$$

The linearized shape equation becomes

$$\frac{\partial^4 U(\tilde{z})}{\partial \tilde{z}^4} + \beta \frac{\partial^2 U(\tilde{z})}{\partial \tilde{z}^2} + \alpha U(\tilde{z}) = \xi. \tag{12.2}$$

And in this general case α and β also depend on ξ:

ind. par.	$H_o R_o, \Delta\tilde{p}$	$\sigma, \Delta\tilde{p}$	$H_o R_o, \tilde{\sigma}$
α	$1 - \Delta\tilde{p}$	$1 - \Delta\tilde{p}$	$1 - \tilde{\sigma} + \frac{1}{2}(1 - H_o^2 R_o^2) - \xi$
β	$\xi + 2H_o R_o - \Delta\tilde{p}$	$\xi + 2\sqrt{1 - 2(\tilde{\sigma} - \Delta\tilde{p} + \xi)} - \Delta\tilde{p}$	$2H_o R_o - \tilde{\sigma} + \frac{1}{2}(1 - H_o^2 R_o^2)$

The deformed radius, $R(z)$, can not exceed R_w at any point along the cylinder. This implies a change in the boundary conditions that limits the deformation to a finite range, $|\tilde{z}| < z_\mathrm{m}$:

$$\begin{aligned} U(0) &= \Delta, \\ U'(0) &= U(\pm z_\mathrm{m}) = U'(\pm z_\mathrm{m}) = 0. \end{aligned} \tag{12.3}$$

As before, we assume an infinitesimal force ring width. At $|\tilde{z}| = z_\mathrm{m}$ the membrane exerts a force proportional to $U'''(\pm z_\mathrm{m})$ that is counter-parted by the cell wall. Due to the constraint $U'(\pm z_\mathrm{m}) = 0$ this force remains finite. The general solution of Eq. **??** for $\Delta\tilde{p} \neq 1$ and $\beta^2 \neq 4(1 - \Delta\tilde{p})$ is

$$U(\tilde{z}) = \frac{\xi}{\alpha} + C \exp\left(\pm \sqrt{-\frac{\beta}{2} \pm \frac{1}{2}\sqrt{\beta^2 - 4\alpha}\tilde{z}} \right). \tag{12.4}$$

The four coefficients C are determined by the boundary conditions, Eq. 12.3. The shape function still contains the unknown parameter z_m. Minimization of the membrane free energy with respect to z_m gives the relation between the deformation lateral extent, z_m, and its depth, Δ. The mechanical properties of the membrane (the relation between σ, κ, H_o) and Δp determine how Eq. 12.4 splits up in a linear combination of trigonometric and hyperbolic terms. We will find the same regions as before for the free membranes and an additional region for $\alpha < 0$, unstable without the existence of a limiting wall. We will continue with a more detailed analysis of Eq. 12.4 in the case $\Delta p = 0$.

12.3. Open tubular structures

As we have mentioned above, there is a large osmotic pressure difference between the bacterial cytoplasm and the external medium so that the assumption, $\Delta p = 0$, in principle is not valid for the *in vivo* cell division process. On the other hand, we will see later that the force that is required to deform the membrane against this huge Δp difference is enormous so that we can suppose that bacteria have a mechanism that regulates this osmotic pressure difference during cell growth and division and reduces the actual needed volume work. The amount of this reduction is not known, so we will first study the limit of vanishing volume work. Within this limit, we will start with the simplest case, a membrane at equilibrium, surrounded by a rigid wall.

12.3.1. Deformation of a membrane at equilibrium, limited by a rigid wall

In this case, the only difference to a free membrane is that the radius of the deformed membrane can not exceed the wall radius at any time. We will now see the influence of this constraint on the membrane shape and the ring force. The shape of the deformation becomes:

$$U(\tilde{z}) = \begin{cases} -\Delta\cos(\zeta^+|\tilde{z}|)\cosh(\zeta^-|\tilde{z}|) + C_1\sin(\zeta^+|\tilde{z}|)\sinh(\zeta^-|\tilde{z}|) + \\ \quad C_2\left[\sin(\zeta^+|\tilde{z}|)\cosh(\zeta^-|\tilde{z}|) - \frac{\zeta^+}{\zeta^-}\cos(\zeta^+|\tilde{z}|)\sinh(\zeta^-|\tilde{z}|)\right] & \text{for} ||\tilde{z}|| < z_{\mathrm{m}}, \\ 0 & \text{for} ||\tilde{z}|| > z_{\mathrm{m}}. \end{cases}$$

with

$$\zeta^{\pm} = \sqrt{\frac{1 \pm R_w H_o}{2}}, \tag{12.5}$$

and

$$\begin{aligned} C_1 &= \Delta\frac{\zeta^+\zeta^-}{\lambda}\left(\cos(2\zeta^+ z_m) - \cosh(2\zeta^- z_m)\right), \\ C_2 &= \frac{\Delta\zeta^-}{\lambda}\left(\zeta^-\sin(2\zeta^+ z_m) + \zeta^+\sinh(2\zeta^- z_m)\right), \\ \lambda &= 1 - (\zeta^-)^2\cos(2\zeta^+ z_m) - (\zeta^+)^2\cosh(2\zeta^- z_m). \end{aligned} \tag{12.6}$$

In this case, the easiest way to calculate z_{m} is by setting $\tilde{U}''(z_{\mathrm{m}}) = 0$,

$$\tilde{U}''(z_{\mathrm{m}}) = 4\frac{\Delta}{\lambda}\zeta^-\zeta^+\sin(\zeta^+ z_{\mathrm{m}})\sinh(\zeta^- z_{\mathrm{m}}). \tag{12.7}$$

We get $z_{\mathrm{m}} = \frac{\pi}{\zeta^+}$, independent of the depth of the deformation, Δ. Notice, that this distance is just half of the distance between two rings in a periodic ring distribution on a free tubular liposome that minimizes the membrane free energy. The constriction force is now

$$f_r = 8\pi\kappa\frac{\Delta}{R_w}\frac{\zeta^-\sinh\left[\frac{2\pi\zeta^-}{\zeta^+}\right]}{\cosh\left[\frac{2\pi\zeta^-}{\zeta^+}\right] - 1}. \tag{12.8}$$

In the limit $H_o = 0$, the force becomes

$$f_{r,H_o=0} = 8\pi\kappa\frac{\Delta}{R_w}\sqrt{2}\coth(\pi). \tag{12.9}$$

For liposomes with no spontaneous curvature, the cell wall causes the constriction force to increase by a factor $\coth(\pi) \simeq 1.004$. This factor grows for growing values of $R_w H_o$. In the limit of vanishing surface tension ($\sigma = 0, R_o H_o = 1$), the force for a free liposome in the linear approximation was zero. This is no longer true when the liposome is surrounded by a rigid wall. The shape equation for this case becomes:

$$\tilde{U}(\tilde{z}) = \begin{cases} -\Delta\left(\cos(\tilde{z}) + \frac{1}{\pi}\left[\sin(\tilde{z}) - \tilde{z}\cos(\tilde{z})\right]\right) & \text{for} |\tilde{z}| < \pi, \\ 0 & \text{for} |\tilde{z}| > \pi. \end{cases} \tag{12.10}$$

And in this limit, the constriction force is

$$f_{r,\sigma=0} = 8\kappa\frac{\Delta}{R_w}. \tag{12.11}$$

Fig. 12.1 summarizes the differences in shape and ring force caused by a rigid wall.

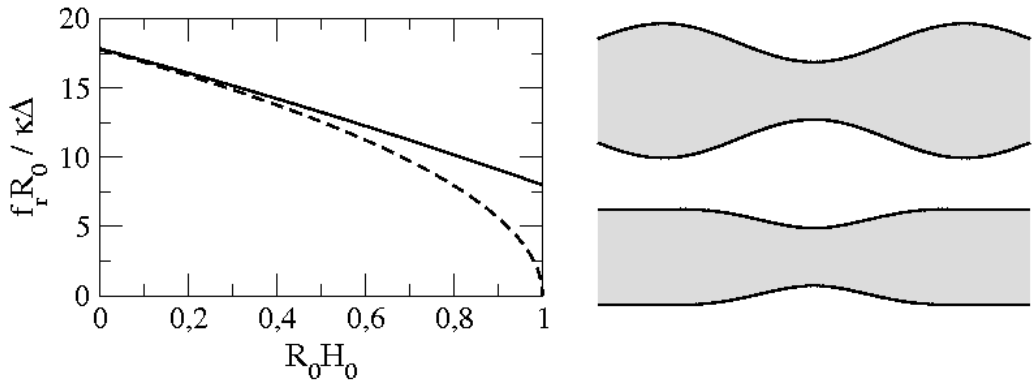

Figure 12.1.: Linear approximation of the force required for the deformation of a membrane as a function of its spontaneous curvature. In both cases, the undeformed membrane adopts its equilibrium radius, the straight line gives the deformation force for a membrane surrounded by a rigid wall, the dashed line for a free tubular liposome. On the right, membranes with $R_o H_o = 1$ and a relative deformation depth, $\Delta = 0.4$ without (above) and inside (below) a rigid wall.

12.3.2. Deformation of a membrane with radius constrained to the wall radius

The next step will be a reduction of the limiting wall radius with respect to the equilibrium radius of the membrane. For $\Delta\tilde{p} = 0$ and $R_o > R_w$ we find that $\beta^2 - 4 < 0$ for all possible values of $R_w H_o$ and $\frac{\sigma}{\kappa}$ and so, the shape of the deformation can be written as:

$$U(\tilde{z}) = \begin{cases} \xi - (\Delta + \xi)\cos(\zeta^+\tilde{z})\cosh(\zeta^-\tilde{z}) + C_1\sin(\zeta^+\tilde{z})\sinh(\zeta^-\tilde{z}) + \\ \quad C_2\left[\sin(\zeta^+\tilde{z})\cosh(\zeta^-\tilde{z}) - \frac{\zeta^+}{\zeta^-}\cos(\zeta^+\tilde{z})\sinh(\zeta^-\tilde{z})\right] & \text{for} |\tilde{z}| < z_\mathrm{m}, \\ 0 & \text{for} |\tilde{z}| > z_\mathrm{m}, \end{cases}$$

with

$$\zeta^\pm = \sqrt{\frac{1}{2} \pm \frac{\beta}{4}}, \tag{12.12}$$

and

$$
\begin{aligned}
C_1 &= (\Delta+\xi)\frac{\zeta^+\zeta^-}{\lambda}\left(\cos(2\zeta^+ z_m)-\cosh(2\zeta^- z_m)\right)+\frac{2\xi}{\lambda}\left(\sin(\zeta^+ z_m)\sinh(\zeta^- z_m)\right),\\
C_2 &= \frac{(\Delta+\xi)\zeta^-}{\lambda}\left(\zeta^-\sin(2\zeta^+ z_m)+\zeta^+\sinh(2\zeta^- z_m)\right)+\\
&\quad \frac{2\xi\zeta^-}{\lambda}\left(\zeta^-\cosh(\zeta^- z_m)\sin(\zeta^+ z_m)+\zeta^+\cos(\zeta^+ z_m)\sinh(\zeta^- z_m)\right),\\
\lambda &= 1-(\zeta^-)^2\cos(2\zeta^+ z_m)-(\zeta^+)^2\cosh(2\zeta^- z_m). \qquad (12.13)
\end{aligned}
$$

The coefficients C_1 and C_2 still contain Δ and z_m. In principle, their relation is given by fixing Δ and searching for the minimum of the membrane free energy with respect to z_m. But actually, the membrane free energy has no local minimum for z_m, the minimum is of global nature as z_m is found to be just at the limit between deformations that fulfill the condition $R(z) < R_w$ and solutions, where the radius of the membrane exceeds the cell wall. In the latter case, an extra energy term must be added, accounting for the infinitely high cost for penetrating the rigid cell wall. The relation between Δ and z_m can be obtained by calculating the minimum of the constriction force for a fixed deformation depth with respect to z_m. We have to solve $\frac{\partial}{\partial z_\mathrm{m}}\tilde{U}'''(z_\mathrm{m}) = 0$ and that leads to:

$$
\Delta = \xi\frac{\left[\zeta^-\sin(\zeta^+ z_\mathrm{m})-\zeta^+\sinh(\zeta^- z_\mathrm{m})\right]^2}{2\zeta^+\zeta^-\sin(\zeta^+ z_\mathrm{m})\sinh(\zeta^- z_\mathrm{m})}. \qquad (12.14)
$$

This relation is equal to $\tilde{U}''(z_\mathrm{m}) = 0$. Although it is quite easy to get Δ as a function of z_m, the physically more intuitive relation, z_m as a function of Δ, can not be calculated analytically as it would imply the solution of a transcendental equation. The ring force as a function of z_m becomes

$$
\begin{aligned}
f_r &= \frac{4\pi\kappa}{R_w}\tilde{U}'''(0)\\
&= \frac{4\pi\kappa\xi}{R_w}\left[\zeta^+\frac{\cosh(\zeta^- z_\mathrm{m})}{\sin(\zeta^+ z_\mathrm{m})}-\zeta^-\frac{\cos(\zeta^+ z_\mathrm{m})}{\sinh(\zeta^- z_\mathrm{m})}\right]. \qquad (12.15)
\end{aligned}
$$

We can now summarize the dependency of the deformation extent and the constriction force with the mechanical properties of the membrane and the relation between its equilibrium radius and the radius of the cell wall.

The deformation extent

The deformation of a membrane limited by a rigid wall can not exceed the cell wall at any point and so, contrary to a free liposome, its extent is finite. At the limit of a membrane that adopts its equilibrium radius inside this rigid wall, the extent of the deformation is independent of the deformation depth and decreases with increasing spontaneous curvature. For a slight reduction of R_w, z_m becomes dependent on Δ but it increases rapidly and saturates for very small deformations. For further growing ξ values, the dependency between Δ and z_m becomes stronger and z_m remains well below its saturation value at any time. In this case, for small deformations, Eq. 12.14 can be solved for z_m, giving a $\Delta^{\frac{1}{4}}$ dependency,

$$z_{\mathrm{m}} = \sqrt{6}\left[\frac{2\Delta}{\xi}\right]^{\frac{1}{4}}. \tag{12.16}$$

Fig. 12.2 shows the dependency of z_{m} with Δ for two extreme values of ξ and vanishing spontaneous curvature. It also shows the shape of the deformed membrane for different values of Δ in the two cases. Increasing spontaneous curvature values generally reduce the deformation extent but do not qualitatively change its dependency with Δ.

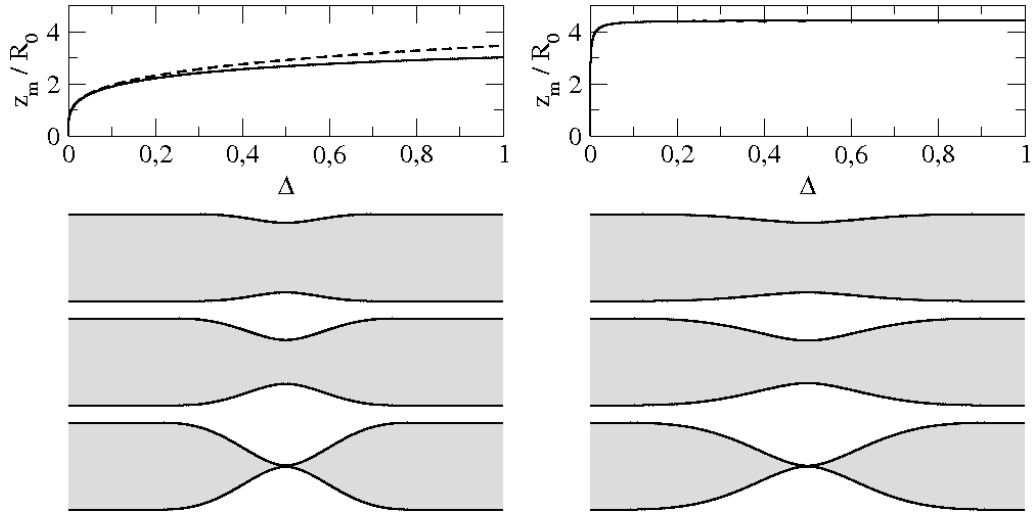

Figure 12.2.: Deformation extent z_{m} as a function of the deformation depth Δ for $\xi = 0.5, R_o H_o = 0$ (left, here the dashed line represents the $\Delta^{\frac{1}{4}}$ approximation) and $\xi = 0.001, R_o H_o = 0$ (right). Deformed membranes for $\Delta = 0.2, \Delta = 0.5$ and $\Delta = 0.99$ and the same parameters as above.

The deformation force

We have seen before that the force, required for the deformation of a free tubular membrane, decreases with increasing relative spontaneous curvature. This is still true when the membrane is surrounded by a rigid wall. Additionally, the force increases with increasing ξ which can take values between 0 and 0.5 and is a measure for the relative difference between the equilibrium radius of the membrane and the limiting wall radius. For small deformations, the ring force was linear in Δ in the case of a free membrane. This is still true for a tubular membrane at equilibrium ($\xi = 0$) surrounded by a rigid wall, where we found that the deformation extent was independent of the deformation depth. For $\xi > 0$, there is a qualitative change in the behaviour of the force which now shows a $\Delta^{\frac{1}{4}}$ dependency, just like the deformation extent, z_{m}. For small deformations, the force can be expressed as a function of Δ,

$$f_r = \frac{8\pi\kappa}{R_w}\frac{(2\xi)^{\frac{3}{4}}}{\sqrt{3}}\Delta^{\frac{1}{4}}. \tag{12.17}$$

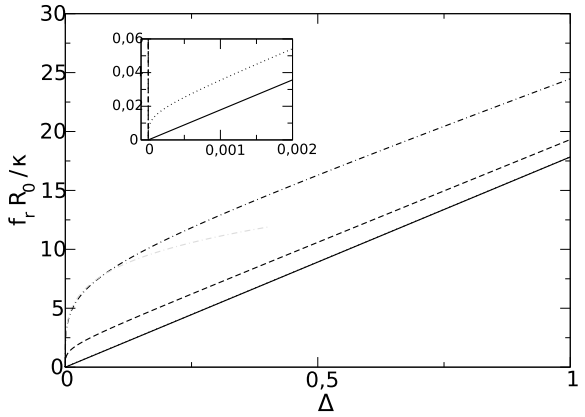

Figure 12.3: Ring force f_r as a function of the deformation depth Δ for $\xi = 0$, $\xi = 0.001$, $\xi = 0.1$ and $\xi = 0.5$. The force increases for increasing ξ. The grey line shows the $\Delta^{\frac{1}{4}}$ approximation for $\xi = 0.5$. The curves for $\xi = 0$ and $\xi = 0.001$ can only be distinguished making a zoom at very small deformations: the inset shows the qualitative difference between the force necessary to deform a membrane at equilibrium ($\xi = 0$) and a membrane whose radius is limited by a rigid wall ($\xi > 0$).

Fig. 12.3 shows the required ring force as a function of the deformation depth for different values of ξ.

12.4. Membrane tubes with osmotic pressure difference

Finally we have come to the section, where we treat the situation found inside the bacteria. A membrane tube with closed ends and positive osmotic pressure difference, surrounded by a rigid wall. Again, we find different regions with different shapes of deformations. Now, instead of two independent membrane properties which lead to the same equilibrium radius, we have three independent parameters which describe the membrane that is formed inside a wall with radius R_w. In two dimensions, we can represent slices of a phase diagram as a function of two of the parameters, fixing the third one. We will do this, fixing the stability parameter ξ. Fig. 12.4 shows the diagram for $\xi = 0$, a membrane at equilibrium, surrounded by a rigid wall. The only change to Fig. 11.1 is found for $\alpha < 0$, a region forbidden for free membranes. In this region, the deformation is a sum of pure hyperbolic functions and pure oscillations. We will define some variables in order to generalize the further equations:

$$r_\alpha = \sqrt{|\alpha|}, \tag{12.18}$$

$$r_\beta = \sqrt{\beta^2 - 4\alpha}, \tag{12.19}$$

$$r^\pm = \frac{\beta \pm r_\beta}{2}, \tag{12.20}$$

$$\zeta^\pm = \frac{\sqrt{\beta \pm 2\alpha}}{2}. \tag{12.21}$$

We will define the hyperbolic and trigonometric terms as follows:

region	oscillation (o)	hyperbolic (h)	combination of h and o (hpo)	hyperbolic oscillation (ho)
c_m^+	$\cos(\sqrt{r^+}z_m)$	$\cosh(\sqrt{-r^+}z_m)$	$\cos(\sqrt{r^+}z_m)$	$\cos(\zeta^+ z_m)$
c_m^-	$\cos(\sqrt{r^-}z_m)$	$\cosh(\sqrt{-r^-}z_m)$	$\cosh(\sqrt{-r^-}z_m)$	$\cosh(\zeta^- z_m)$
s_m^+	$\sin(\sqrt{r^+}z_m)$	$\sinh(\sqrt{-r^+}z_m)$	$\sin(\sqrt{r^+}z_m)$	$\sin(\zeta^+ z_m)$
s_m^-	$\sin(\sqrt{r^-}z_m)$	$\sinh(\sqrt{-r^-}z_m)$	$\sinh(\sqrt{-r^-}z_m)$	$\sinh(\zeta^- z_m)$
c^+	$\cos(\sqrt{r^+}\lvert\tilde{z}\rvert)$	$\cosh(\sqrt{-r^+}\lvert\tilde{z}\rvert)$	$\cos(\sqrt{r^+}\lvert\tilde{z}\rvert)$	$\cos(\zeta^+\lvert\tilde{z}\rvert)$
c^-	$\cos(\sqrt{r^-}\lvert\tilde{z}\rvert)$	$\cosh(\sqrt{-r^-}\lvert\tilde{z}\rvert)$	$\cosh(\sqrt{-r^-}\lvert\tilde{z}\rvert)$	$\cosh(\zeta^-\lvert\tilde{z}\rvert)$
s^+	$\sin(\sqrt{r^+}\lvert\tilde{z}\rvert)$	$\sinh(\sqrt{-r^+}\lvert\tilde{z}\rvert)$	$\sin(\sqrt{r^+}\lvert\tilde{z}\rvert)$	$\sin(\zeta^+\lvert\tilde{z}\rvert$
s^-	$\sin(\sqrt{r^-}\lvert\tilde{z}\rvert)$	$\sinh(\sqrt{-r^-}\lvert\tilde{z}\rvert)$	$\sinh(\sqrt{-r^-}\lvert\tilde{z}\rvert)$	$\sinh(\zeta^-\lvert\tilde{z}\rvert)$

and

$$\lambda_{o,h,hpo} = 2r_\alpha(1 - c_m^+ c_m^-) - \beta s_m^+ s_m^-, \tag{12.22}$$

$$\lambda_{ho} = (\zeta^-)^2\left[(c_m^+)^2 - 1\right] + (\zeta^+)^2\left[(c_m^-)^2 - 1\right]. \tag{12.23}$$

Now, we can analyze the special case $\xi = 0$.

12.4.1. Deformation of a membrane at equilibrium surrounded by a rigid wall

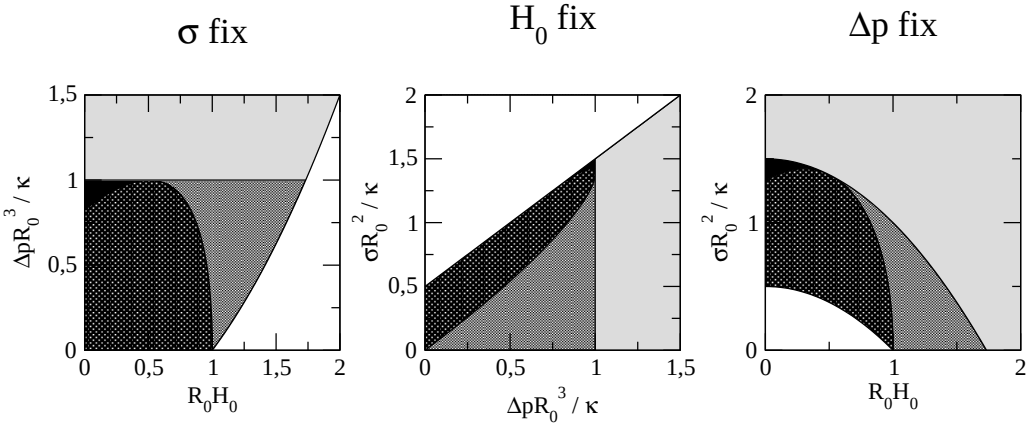

Figure 12.4.: Representation of the different regions of membrane deformation for $\xi = 0$. Black: purely hyperbolic, dark grey: product of hyperbolic functions and oscillation, grey: pure oscillation, light grey: sum of hyperbolic functions and oscillation, white: parameter region with A) negative surface tension, B) negative spontaneous curvature and C) $\Delta\tilde{p} < 0$.

For $\xi = 0$ the shape of the deformation is:

$$U_{(o)}^{\xi=0}(\tilde{z}) = C_1^+ c^+ + C_1^- c^- + C_2\left(s^+ - \frac{r_\alpha}{r^-}s^-\right), \tag{12.24}$$

$$U_{(h,hpo)}^{\xi=0}(\tilde{z}) = C_1^+ c^+ + C_1^- c^- + C_2\left(s^+ + \frac{r_\alpha}{r^-}s^-\right), \tag{12.25}$$

$$U_{(ho)}^{\xi=0}(\tilde{z}) = \Delta c^- c^+ + C_1\left(s^+ c^- - \frac{\zeta^+}{\zeta^-}c^+ s^-\right) + C_2 s^+ s^-, \tag{12.26}$$

with

$$C_{1(o,h,hpo)}^{\pm(\xi=0)} = \frac{\Delta}{\lambda}\left[r_\alpha(1 - c_\mathrm{m}^- c_\mathrm{m}^+) - r^\mp s_\mathrm{m}^+ s_\mathrm{m}^-\right], \tag{12.27}$$

$$C_{2(o,hpo)}^{(\xi=0)} = \frac{\Delta}{\lambda}\left[-r_\alpha c_\mathrm{m}^- s_\mathrm{m}^+ + r^- c_\mathrm{m}^+ s_\mathrm{m}^-\right], \tag{12.28}$$

$$C_{2(h)}^{(\xi=0)} = \frac{\Delta}{\lambda}\left[r_\alpha c_\mathrm{m}^- s_\mathrm{m}^+ + r^- c_\mathrm{m}^+ s_\mathrm{m}^-\right], \tag{12.29}$$

$$C_{1(ho)}^{(\xi=0)} = \frac{\Delta}{\lambda}\zeta^-\left[\zeta^- s_\mathrm{m}^+ c_\mathrm{m}^+ + \zeta^+ s_\mathrm{m}^- c_\mathrm{m}^-\right], \tag{12.30}$$

$$C_{2(ho)}^{(\xi=0)} = \frac{\Delta}{\lambda}\zeta^+\zeta^-\left[\left(c_\mathrm{m}^+\right)^2 - \left(c_\mathrm{m}^-\right)^2\right]. \tag{12.31}$$

The rigid wall imposes an upper limit of the membrane radius which, in this case, is equal to its equilibrium radius. Actually, for this strict $\xi = 0$ case, the light grey region (hpo) in Fig. 12.4 remains unstable and a membrane tube with the corresponding parameters would collapse inside the rigid wall. The shape of the deformation in the region with before purely exponential decay will remain the same as the radius stays below the wall radius along the whole tube. The deformation extent of the two remaining regions (o and ho) can be calculated be setting $\tilde{U}''(z_\mathrm{m}) = 0$,

$$\tilde{U}_{(o)}''(z_\mathrm{m}) = \frac{\Delta}{\lambda}r_\alpha r_\beta(c_\mathrm{m}^- - c_\mathrm{m}^+), \tag{12.32}$$

$$\tilde{U}_{(ho)}''(z_\mathrm{m}) = 2\frac{\Delta}{\lambda}\zeta^-\zeta^+\alpha s_\mathrm{m}^+ s_\mathrm{m}^-. \tag{12.33}$$

For the *ho* region we get, as before, $z_\mathrm{m} = \frac{\pi}{\zeta^+}$ and for the *o* region we get $z_\mathrm{m} = \frac{2\pi}{\sqrt{r^+}+\sqrt{r^-}}$. In both cases, z_m is independent of the deformation depth, Δ.

$$f_{r(o)} = \frac{4\pi\kappa\Delta}{R_o}\frac{r_\alpha r_\beta\left(\sqrt{r^-}+\sqrt{r^+}\right)}{2r_\alpha+\beta}\cot\left(\frac{2\pi\sqrt{r^+}}{\sqrt{r^+}+\sqrt{r^-}}\right), \tag{12.34}$$

$$f_{r(ho)} = \frac{8\pi\kappa\Delta}{R_o}\zeta^-\beta\coth\left(\frac{\pi\zeta^-}{\zeta^+}\right). \tag{12.35}$$

12.4.2. Deformation of a membrane with radius constrained to the wall radius

Now, we have come to the situation that we will typically find inside bacteria. A closed membrane tube with a radius that is limited by the rigid bacterial cell wall. We will start this section by having a look at how the phase diagram changes for growing values of ξ, equal to a growing difference between the wall radius and the equilibrium radius of the membrane.

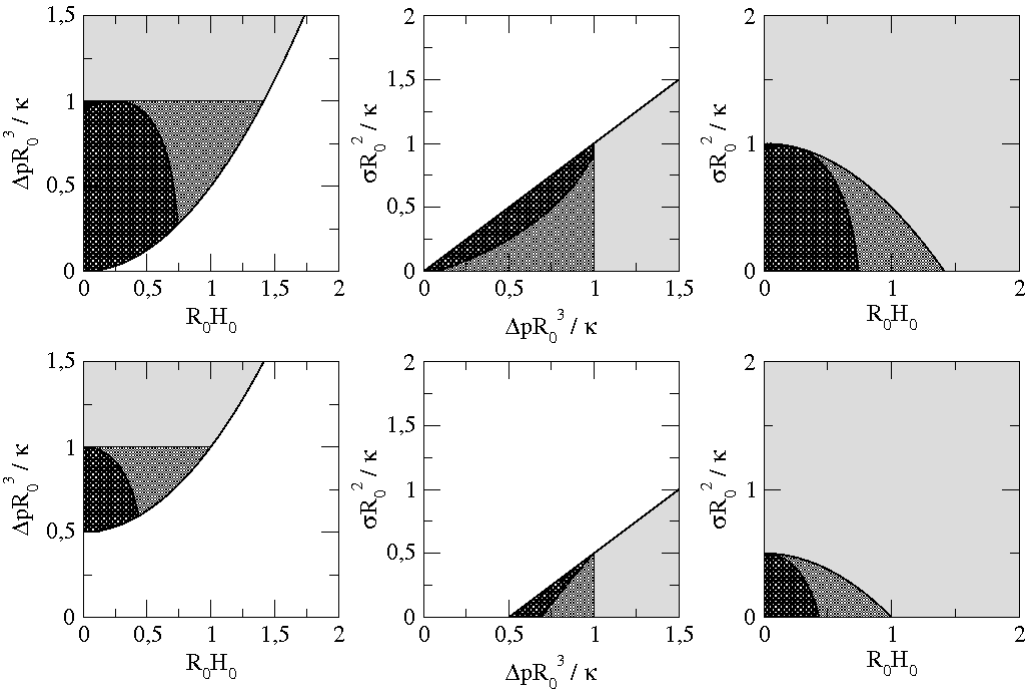

Figure 12.5.: Representation of the different regions of membrane deformation for $\tilde{\xi} = 0.5$ (above) and $\tilde{\xi} = 1$ (below). Black: *h*, dark grey: *ho*, grey: *o*, light grey: *hpo*, white: parameter region with A) negative surface tension and B) negative spontaneous curvature.

In Fig. 12.5 we can see that for growing $\tilde{\xi}$ the *o*, *h* and *ho* regions become smaller and the *hpo* region dominates more and more the phase diagram. For $\tilde{\xi} = 1$ the purely hyperbolic region vanishes completely and for $\tilde{\xi} = 1.5$ the only surviving region is the combination of hyperbolic and oscillating deformation. The shape of the membrane in the different parameter regions is now:

$$U(\tilde{z}) = -\frac{\tilde{\xi}}{\alpha} + U^{(\tilde{\xi}=0)}(\tilde{z}), \tag{12.36}$$

and

$$C^{\pm}_{1(o,h,hpo)} = C^{\pm(\tilde{\xi}=0)}_{1(o,h,hpo)} + \frac{\tilde{\xi}}{\alpha\lambda}\left[r_\alpha(1 - c^-_m c^+_m \mp c^-_m \pm c^+_m) - r^{\mp} s^+_m s^-_m\right], \tag{12.37}$$

$$C_{2(o,hpo)} = C^{(\tilde{\xi}=0)}_{2(o,hpo)} + \frac{\Delta}{\lambda}\left[-r_\alpha s^+_m(c^-_m - 1) + r^- s^-_m(c^+_m - 1)\right], \tag{12.38}$$

$$C_{2(h)} = C^{(\tilde{\xi}=0)}_{2(h)} + \frac{\Delta}{\lambda}\left[r_\alpha s^+_m(c^-_m - 1) + r^- s^-_m(c^+_m - 1)\right], \tag{12.39}$$

$$C_{1(ho)} = C^{(\tilde{\xi}=0)}_{1(ho)} + \frac{\tilde{\xi}}{\alpha\lambda}\zeta^-(c^+_m - c^-_m)\left[\zeta^- s^+_m - \zeta^+ s^-_m\right], \tag{12.40}$$

$$C_{2(ho)} = C^{(\tilde{\xi}=0)}_{2(ho)} + \frac{\tilde{\xi}}{\alpha\lambda}\zeta^+\zeta^-\left[\left(c^+_m\right)^2 - \left(c^-_m\right)^2 + r_\alpha s^+_m s^-_m\right]. \tag{12.41}$$

z_m is no longer constant, it depends on the depth of the deformation, Δ. We find the following relation:

$$\Delta_{(o)} = \frac{\xi}{\alpha}\left(\frac{\beta(1-c_{\rm m}^{+}c_{\rm m}^{-})-2r_\alpha s_{\rm m}^{+}s_{\rm m}^{-}}{r_\beta(c_{\rm m}^{-}-c_{\rm m}^{+})}-1\right), \tag{12.42}$$

$$\Delta_{(h)} = \frac{\xi}{\alpha}\left(\frac{-\beta(1-c_{\rm m}^{+}c_{\rm m}^{-})+2r_\alpha s_{\rm m}^{+}s_{\rm m}^{-}}{r_\beta(c_{\rm m}^{-}-c_{\rm m}^{+})}-1\right), \tag{12.43}$$

$$\Delta_{(hpo)} = \frac{\xi}{\alpha}\left(\frac{\beta(1-c_{\rm m}^{+}c_{\rm m}^{-})+2r_\alpha s_{\rm m}^{+}s_{\rm m}^{-}}{r_\beta(c_{\rm m}^{-}-c_{\rm m}^{+})}-1\right), \tag{12.44}$$

$$\Delta_{(ho)} = \frac{\xi}{\alpha}\frac{(\zeta^{-}s_{\rm m}^{+}-\zeta^{+}s_{\rm m}^{-})^2}{2\zeta^{+}\zeta^{-}s_{\rm m}^{+}s_{\rm m}^{-}}. \tag{12.45}$$

And the forces are:

$$f_{r(o)} = \frac{4\pi\kappa\xi}{R_w r_\alpha}\frac{\sqrt{r^{+}}c_{\rm m}^{+}s_{\rm m}^{-}-\sqrt{r^{-}}c_{\rm m}^{-}s_{\rm m}^{+}}{c_{\rm m}^{+}-c_{\rm m}^{-}}, \tag{12.46}$$

$$f_{r(h)} = \frac{4\pi\kappa\xi}{R_w r_\alpha}\frac{\sqrt{-r^{+}}c_{\rm m}^{+}s_{\rm m}^{-}-\sqrt{-r^{-}}c_{\rm m}^{-}s_{\rm m}^{+}}{c_{\rm m}^{+}-c_{\rm m}^{-}}, \tag{12.47}$$

$$f_{r(hpo)} = \frac{4\pi\kappa\xi}{R_w r_\alpha}\frac{\sqrt{r^{+}}c_{\rm m}^{+}s_{\rm m}^{-}-\sqrt{-r^{-}}c_{\rm m}^{-}s_{\rm m}^{+}}{c_{\rm m}^{+}-c_{\rm m}^{-}}, \tag{12.48}$$

$$f_{r(ho)} = \frac{4\pi\kappa\xi}{R_w r_\alpha}\frac{\beta(\zeta^{-}c_{\rm m}^{+}s_{\rm m}^{+}-\zeta^{+}s_{\rm m}^{-}c_{\rm m}^{-})}{s_{\rm m}^{+}s_{\rm m}^{-}}. \tag{12.49}$$

We will now analyze the two extremes, membranes constrained by a wall with radius close to the equilibrium radius, and very high osmotic pressure differences like in bacteria which imply high values of ξ.

Deformations close to equilibrium

As soon as R_w is below the equilibrium radius of the membrane, we find two qualitative changes, one in the stability and the other one in the deformation of a membrane. First, membranes with $\alpha < 0$ (hpo- region) are stable in this case, although we will see that the deformation force in this case has a maximum and vanishes at a certain depth of the deformation. This is also the case for the purely oscillating deformations. And second, the extent of the deformation now depends on Δ and goes from zero up to a certain value, staying always below the limit for $\xi = 0$. This is the case for all of the four different regions. Fig. 12.6 shows the deformation extent as a function of Δ.

$z_{\rm m}$ is smallest in the region of pure oscillation and maximum in the region of purely hyperbolic deformation. For $R_w H_o = 1$ and for $\alpha < 0$, the deformation extent is drawn only until the limit where the deformation force vanishes. Compared to the forces that a required to deform a membrane tube with vanishing osmotic pressure difference, close to equilibrium due to the balance between surface tension and spontaneous curvature, the forces needed here (Fig. 12.7) are much lower. This can be easily understood by the fact that a membrane which is close to equilibrium with $\Delta\tilde{p} \simeq 1$ is also close to instability. Further, the forces for deformations with a purely oscillating part show a maximum at a certain deformation depth. From there on the deformation force decreases and may even vanish.

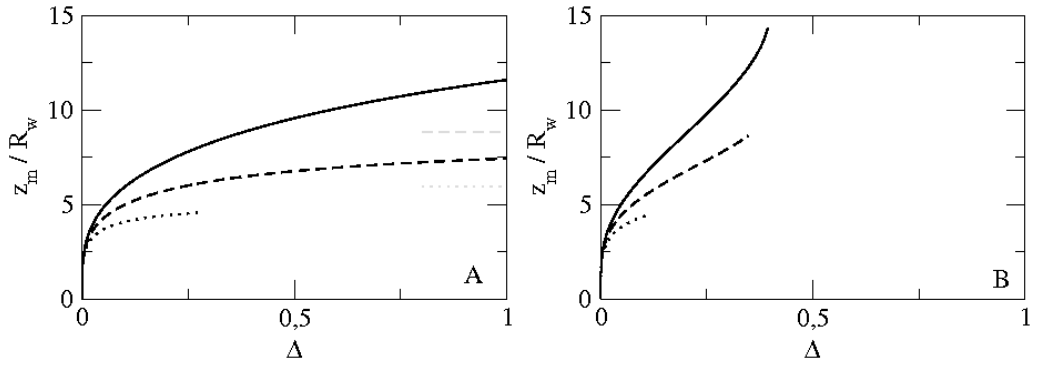

Figure 12.6.: Deformation extent z_m as a function of the deformation depth Δ for $\xi = 0.01$. A) $\Delta\tilde{p} = 0.95$ and $R_w H_o = 0.1$ (continuous line, (*h*)), $R_w H_o = 0.5$ (dashed line, (*ho*)), $R_w H_o = 1$ (pointed line, (*o*)) The grey lines show constant limits for $\xi = 0$. B) $\Delta\tilde{p} = 1.05$ (*hpo*) and $R_w H_o$ like in A). Here, z_m is drawn until the limit of vanishing deformation force.

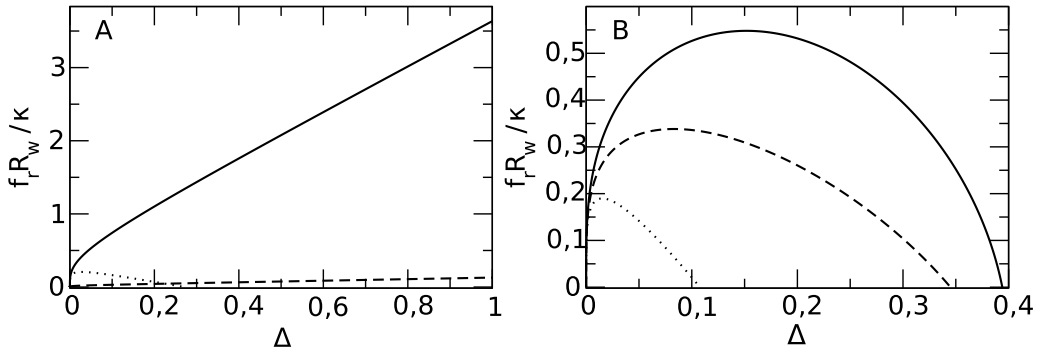

Figure 12.7.: Deformation force f_r as a function of the deformation depth Δ for $\xi = 0.01$. A) $\Delta\tilde{p} = 0.95$ and $R_w H_o = 0.1$ (continuous line, (*h*)), $R_w H_o = 0.5$ (dashed line, (*ho*)), $R_w H_o = 1$ (pointed line, (*o*)) B) $\Delta\tilde{p} = 1.05$ (*hpo*) and $R_w H_o$ like in A).

Deformations far from equilibrium

In principle, we now come to the situation that we find *in vivo*. The membrane tube is surrounded by a rigid wall that works against the enormous osmotic pressure difference between the inside of the bacteria and the external medium and restricts the equilibrium radius of the membrane tube to the wall radius. We will see that the force, necessary to overcome the whole osmotic pressure difference of $\simeq 3 - 4$atm, is orders of magnitude larger than the forces typically produced by biomechanical cell mechanisms. For $\Delta\tilde{p} \gg 1$, the shape of the deformed membrane is a combination of hyperbolic and oscillatory terms. For small deformations, the deformation extent, Eq. 12.44 and the deformation force, Eq. 12.48, can be approximated by

$$z_m = \sqrt{6}\left[\frac{2\Delta}{\Delta\tilde{p}}\right]^{\frac{1}{4}}, \tag{12.50}$$

and

$$f_r = \frac{8\pi\kappa}{R_w}\frac{(2\Delta\tilde{p})^{\frac{3}{4}}}{\sqrt{3}}\Delta^{\frac{1}{4}}. \tag{12.51}$$

The cell wall radius of *E. Coli* is about $0.5\mu m$ and a typical value for the bending rigidity of a lipid membrane is $\kappa \approx 20kT$. With these values, the ring force becomes

$$f_r \approx 4(\Delta\tilde{p})^{\frac{3}{4}}\Delta^{\frac{1}{4}}pN. \tag{12.52}$$

For $\Delta p = 4$atm we get $\Delta\tilde{p} \approx 0.6 * 10^6$. A relative deformation of $\Delta = 0.1$ in this case requires a ring force of $f_r \approx 50nN$. Typical forces are between two and three orders of magnitude smaller. Such a ring force, $f_r = 100pN$, produces a relative deformation of only 10^{-12}. On the other hand, this ring force can produce the full constriction of a membrane with an osmotic pressure difference of $\Delta p \simeq 0.001atm$ ($\Delta\tilde{p} = 150$). Fig. 12.8 shows the deformation extent and the ring force as a function of Δ for this case.

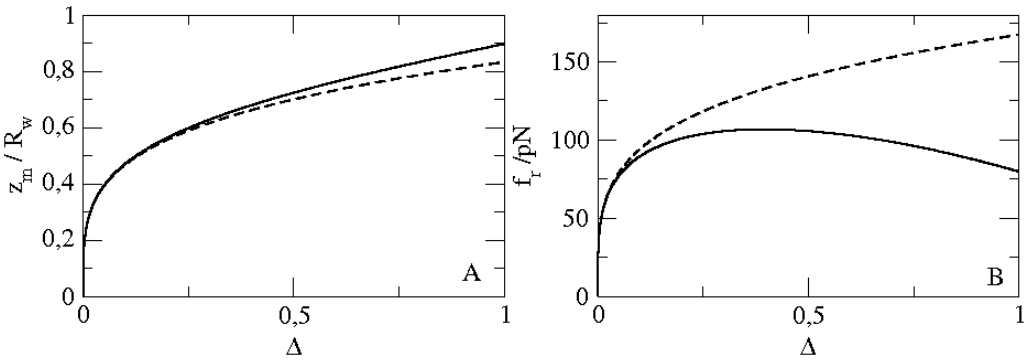

Figure 12.8.: Deformation of a membrane surrounded by a rigid wall with $R_w = 0.5\mu m$, bending rigidity $\kappa = 20kT$ and osmotic pressure difference $\Delta p = 0.001atm$. A) Deformation extent z_m and B) Required ring force f_r as a function of the relative deformation Δ. The dashed lines show the approximations for small deformations (Eqs. 12.50 and 12.51).

The extent of the deformed segment in this case becomes much shorter and stays below the radius of the cell wall. In general, it decreases like $\Delta\tilde{p}^{-\frac{1}{4}}$. The ring force increases like $\Delta\tilde{p}^{\frac{3}{4}}$. For small deformations, f_r is proportional to $\Delta^{\frac{1}{4}}$, further on, the force shows a maximum for $\Delta \approx 0.4$. Fig. 12.9 illustrates the shape of the membrane at different stages of the deformation. For membranes close to instability, the extent of the deformed segment is very large and the forces are low while for large osmotic pressure differences, the deformation is limited to a short region and the required ring force is high.

12.5. Conclusions

Membrane deformations within a limiting, rigid wall are qualitatively different from deformations without constraints as the radius of the tube must stay below the wall radius at every point

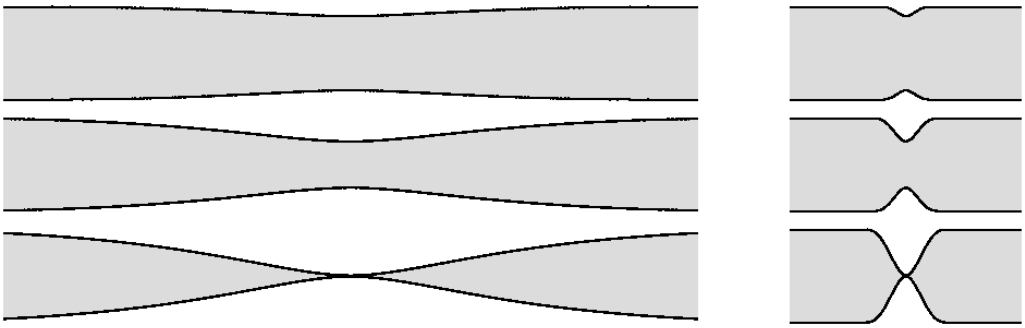

Figure 12.9.: Deformed membranes for $\Delta = 0.2, \Delta = 0.5, \Delta = 0.99$. Left: $\xi = 0.01, \Delta\tilde{p} = 0.95, R_w H_o = 0.1$, right: $\Delta\tilde{p} = 150$.

and the deformation of the membrane is limited to a region $|z| < z_{\mathrm{m}}$. Within these boundaries, the shape of the deformation is a linear combination of hyperbolic and oscillating terms, depending on spontaneous curvature, surface tension and osmotic pressure difference between the inside of the tube and the surrounding medium. The cylindrical radius is no longer determined by a balance between these three material properties, as long as the resulting equilibrium radius exceeds the cell wall radius. For growing values of the osmotic pressure difference, $\Delta\tilde{p} \gg 1$, the difference between R_o and R_w becomes each time more important and the deformation extent decreases while the required radial forces become very large. A small deformation of a bacterial cell membrane against a typical osmotic pressure difference, $\Delta p \approx 3 - 4\mathrm{atm}$, would require forces around three orders of magnitude larger than the forces generated by conventional biological motors. At present, little is known about how bacteria regulate and maintain their osmotic pressure difference between the cytoplasm and the surrounding medium during cell growth and division. Together with deeper insights into the role of the outer cell layers this question is fundamental for a detailed understanding of the bacterial cell division process.

13. General conclusions

This thesis was divided into two parts, highlighting the two complementary parts of the bacterial cell division process, the force generating Z-ring and the resulting deformation of the inner bacterial cell membrane.

In the first part of our work, we introduced a minimal model for filaments formed by FtsZ, the major cell division protein. The model was inspired by recent AFM images of FtsZ filaments on mica that allowed, for the first time, their observation in dynamic equilibrium conditions. The first images that we analysed showed individual, curved filaments as well as chains forming coiled structures with apparent lateral attraction. In our model, based on monomer-monomer interactions, we expressed these observations in terms of a strong bond between adjacent monomers, a spontaneous bond curvature θ_o with associated bending rigidity κ_c and a lateral interaction potential that we included in form of a Lennard-Jones potential with potential depth ϵ between any pair of monomers. Starting the analysis of the experimental data with short filaments, formed in presence of the non-hydrolyzable GTP-analogue GDP-AlF_3 and without lateral contacts, we estimated the bending parameters, $\beta\kappa_c \approx 80$ and $\theta_o \approx 2.5°$, directly from the AFM images. In Langevin dynamics simulations, we simulated the growth of the chains and the formation of coiled structures. We also estimated the strength of the lateral attraction ($\beta\epsilon \approx 0.2$) comparing the shapes obtained in LD simulations and experiments. Within this minimal chain model for FtsZ filaments, we were able to explain and reproduce the global shapes observed in AFM images of FtsZ with GDP-AlF_3. The persistence length of FtsZ polymers, $L_p = \approx 400nm$, is about one thousand times smaller than for microtubules [26, 27, 35] and still about 50 times smaller than that of actin filaments [26, 36]. They are half way between perfectly stiff chains and random polymers with typical lengths in the order of the persistence length, $N \approx \beta\kappa$. FtsZ filaments have a hierarchical structure, lateral interactions are important but significantly weaker than the strong covalent bonds between adjacent monomers. The final shape of the polymer is a fine balance between the optimization of lateral contacts and the cost for bending the filament away from its spontaneous curvature. This sensitivity might be of crucial biological importance as small changes in the environmental conditions may take influence on the chain configuration along the cell cycle.

In the most recent AFM images [29] of FtsZ filaments an apparent polymorphism in chain configurations - extremely straight filaments, coexisting with the typical curved polymers - required an extension of the chain model, including an interaction protein - mica together with a spontaneous filament roll curvature. In that case, straight filaments optimize their anchorage to the substrate being bound at their specific binding sites and curved filaments adopt their preferential roll curvature along the chain. Depending on the spontaneous roll curvature and the strength of

protein -mica interaction, compared to the cost for bending the filament away from this preferential curvature, a complicated energy landscape with several local minima arises. These local minima correspond to growing numbers of complete filament turns with eventually small energetic differences so that for certain filament lengths chains with different mean curvatures may coexist. We estimated the preferential roll curvature, $\psi_o \approx \frac{2\pi}{20} - \frac{2\pi}{15}$, of the filaments observed in the above mentioned experiments and found good agreement with direct experimental measures.

A series of AFM videos, showing predominantly stable ring structures of FtsZ filaments in depolymerization conditions, allows the analysis of the influence of the type of nucleotide and the pH value on different aspects of filament structure and dynamics. Up to present, we have calculated the bending rigidities of rings in different experimental conditions and found that decreasing pH value and non-hydrolyzable nucleotides seem to make the filaments stiffer. This might be a consequence of the experimentally observed tendency of slower bond dynamics. The global shape fluctuations of rings in subsequent AFM images show slow dynamics and permitted a rough calibration of the time scale in the simulations. We further explored in simulations the influence of the polymerization velocity on the formation of either rings or spirals and their size distributions. Future tasks include a detailed analysis of the depolymerization process of FtsZ filaments in different environmental conditions. Rings seem to be very stable structures. Bonds along the ring constantly break and reform, from time to time loosing one monomer and, in that way the rings decrease in size. Compared to open filaments, these ring structures survive much longer times indicating that diffusion processes play an important role for the reformation of once broken bonds. The theoretical description of the whole process of ring dynamics until its complete depolymerization is complicated and still in progress.

Approaching the bacterial *in vivo* conditions, we simulated filaments in cylindrical geometry. A simple transfer of the model parameters estimated for polymers in two dimensions favors the formation of coiled structures on the cylindrical surface instead of a Z-ring perpendicular to its axis, but several mechanisms are able to switch this balance towards the predominant formation of ring structures. We applied one of these mechanisms, the turning-off of the on-plane spontaneous curvature in our simulations, and that way all of the initially short and steadily growing chains started to form a ring around the cylinder. In contrast to the two dimensional spiral structures, the radius of this ring is fixed by its support and not the result of a balance between lateral attraction and bending. Here, the effect of the lateral attraction is the generation of a radial constriction force. With the above estimated parameters, we calculated this force in the simulations and obtained $f_r \approx 4pN$, independent of the size of the cylinder and the filament length. The force is small but it might constitute at least part of the required force for membrane constriction. Actually, the biological role of lateral attraction between filaments is not limited to force generation, in the first place, it is essential for the formation of the Z-ring. An analysis of the shapes adopted by filaments confined to a cylindrical surface, taking into account its mechanical properties, showed that without this condensing effect, helical shapes instead of rings around the cylinder would be the predominant structures [40].

In the second part of this thesis, we investigated the effect of a radial constriction force on

the inner bacterial cell membrane [56]. The description of the membrane in terms of the Helfrich Hamiltonian includes three energetic contributions. Volume work, associated to an osmotic pressure difference between the cytoplasm and the external medium, a cost for augmenting the membrane area, associated to a surface tension and a cost for bending the membrane away from its spontaneous curvature. We further included the force ring as a line tension at the site of constriction. At present, no detailed experimental data are available for the *in vivo* division process but recent experiments showed the *in vitro* invagination of a tubular liposome caused by a Z-ring directly anchored to the membrane. We started our analysis with this simplified system of a free and open tubular liposome where deformations are not constrained by a limiting rigid wall and no volume work has to be done. We calculated the shape of the deformation caused by one force ring and by a series of periodically distributed force rings and found good agreement with the experimentally observed deformations. A rough estimation of the necessary constriction force shows that it is in the range of forces typically generated by biological machines. For a more detailed analysis, a better characterization of the liposome and the exact shape of the deformations would be helpful.

In vivo, the membrane is limited by a rigid wall and so are its deformations. For large osmotic pressure differences, the extent of the deformation is limited to a narrow region around the force ring and the required ring forces become orders of magnitude higher than forces typically generated by biological motors. At present, little is known about how bacteria regulate and maintain their osmotic pressure difference between the cytoplasm and the surrounding medium during cell growth and division. Together with deeper insights into the role of the outer cell layers this question is fundamental for a detailed understanding of the bacterial cell division process.

In this thesis, we have developed different theoretical models for biological processes involved in bacterial cell division. All models are based on experimental observations and have evolved along the time period of the thesis in parallel with the experiments.

Conclusiones generales

Con el objetivo de remarcar los dos estudios que hemos realizado el presente trabajo ha sido dividido en dos partes complementarias: la fuerza generada por el anillo-Z y la deformación que la aplicación de dicha fuerza produce en la parte interior de la membrana bacteriana.

En la primera parte del trabajo hemos analizado un modelo que contiene los componentes mínimos necesarios para estudiar filamentos formados por FtsZ, la proteína más relevante en el proceso de división celular. El modelo se ha inspirado en recientes imágenes obtenidas por AFM de filamentos de FtsZ sobre mica, que han permitido por primera vez la observación de estructuras de FtsZ bajo condiciones de equilibrio dinámico. Las primeras imágenes analizadas mostraron filamentos individuales o curvados así como cadenas formando espirales con una aparente interacción lateral. En nuestro modelo, basado en la interacción monómero-monómero, introducimos esas observaciones experimentales en términos de un enlace fuerte entre monómeros adyacentes junto con una curvatura espontánea, θ_o, del filamento (que tiene asociada un rigidez de bending κ_c) y por último una interacción lateral que incluimos mediante un potencial de Lennard-Jones de intensidad ϵ entre cualquier par de monómeros. Analizando los resultados experimentales para filamentos cortos formados en presencia de GDP-AlF_3 (análogo no hidrolizable a GTP) y sin contactos laterales, hemos sido capaces de estimar los parámetros de bending ($\beta\kappa_c \approx 80$ y $\theta_o \approx 2.5^\circ$) directamente de las imágenes de AFM. Mediante simulaciones de dinámica de Langevin hemos estudiado el crecimiento de las cadenas y la formación de estructuras en espiral. También hemos estimado la intensidad de la atracción lateral ($\beta\epsilon \approx 0.2$) mediante la comparación directa entre las estructuras obtenidas por simulación y las experimentales. Usando este modelo mínimo para filamentos de FtsZ hemos sido capaces de explicar y reproducir de manera satisfactoria la totalidad de las estructuras observadas por AFM en un sistema de FtsZ en presencia de GDP-AlF_3. La longitud de persistencia en polímeros de FtsZ, $L_p \approx 400nm$, es aproximadamente mil veces más pequeña que en microtúbulos [26, 27, 35] y todavía unas cincuenta veces más pequeña que en filamentos de actina [26, 36]. Se encuentran a mitad de camino entre cadenas rígidas y "random polymers" con longitudes típicas del orden de la longitud de persistencia: $N \approx \beta\kappa$. Los filamentos de FtsZ tienen una estructura jerárquica siendo las interacciones laterales importantes pero significativamente más débiles que los enlaces covalentes fuertes entre monómeros contiguos. La forma final que adquiere el polímero es el resultado del balance fino entre la optimización de los contactos laterales y el coste energético que soporta el filamento cuando su curvatura se aleja más allá de la curvatura espontánea. En nuestra opinión esto puede tener una importancia crucial desde un punta de vista biológico ya que pequeños cambios en las condiciones físico-químicas del entorno podrían dar lugar a un gran cambio sobre las configuraciones que las cadenas de FtsZ adoptan dependiendo de las distintas etapas del ciclo celular.

En las imágenes más recientes de AFM [29] se observa un aparente polimorfismo de los filamentos de FtsZ formando cadenas, en concreto parece que filamentos extremadamente rígidos coexisten con polímeros curvados. Para dar cuenta de esta observación ha sido necesario extender el modelo teórico inicial incluyendo una interacción entre la proteína y el substrato de mica junto con una curvatura espontánea de los filamentos. En este caso los filamentos rígidos optimizan la energía de anchoring con el substrato, ya que se enlazan a este en los sitios de enlace especificados, mientras que los filamentos curvados minimizan la energía elástica adoptando su curvatura natural. El balance energético entre los dos mecanismos es complejo y da lugar a la aparición de varios mínimos locales en la energía del sistema. Estos mínimos locales corresponden a filamentos que completan un número de vueltas distinto y con diferencias energéticas muy pequeñas. Para ciertas longitudes del filamento es posible la coexistencia de cadenas con diferentes curvaturas medias.

También hemos estimado la curvatura preferente, $\psi_o \approx \frac{2\pi}{20} - \frac{2\pi}{15}$, de los filamentos observados en los experimentos anteriormente mencionados.

Otra parte importante de este trabajo ha sido analizar qué efecto tiene sobre la estructura y la dinámica de los filamentos la variación del tipo de nucleótido y el valor de pH. Esto ha sido posible mediante el análisis de una serie de vídeos tomados con AFM en los que se observan, en condiciones de despolimerización, anillos estables de FtsZ. Hasta el momento hemos analizado la rigidez de anillos para diferentes condiciones del entorno. Hemos encontrado que tanto la disminución del valor de pH como de nucleótidos no hidrolizables parece aumentar la rigidez de los filamentos. Esto podría ser una consecuencia de la observación experimental de que la dinámica del enlace se ralentiza.

Las fluctuaciones en la forma global de los anillos observadas en imágenes seguidas de AFM tienen una dinámica lenta, de esta forma hemos podido estimar (aunque no de forma muy precisa) la escala de tiempo de nuestras simulaciones. De esta forma ha sido posible estudiar en las simulaciones la influencia de la velocidad de polimerización sobre la formación de anillos o espirales así como sobre la distribución de tamaños. En un futuro analizaremos mas detalladamente el proceso de despolimerización de filamentos de FtsZ en función de las condiciones del entorno. Los anillos de FtsZ son estructuras muy estables. Los enlaces entre monómeros de un anillo están constantemente rompiéndose y volviéndose a formar. En ocasiones, durante el proceso de ruptura y formación de enlaces se pierde un monómero de forma que el anillo disminuye de tamaño. Comparado con estructuras de filamentos abiertos, los anillos sobreviven mucho más tiempo, una clara indicación de que los procesos de difusión juegan un papel importante en la regeneración de enlaces rotos. La descripción, desde un punto de vista teórico, de la dinámica de un anillo hasta que se produce su despolimerización completa es una tarea compleja que se encuentra actualmente en desarrollo.

Otra parte importante del presente trabajo ha sido analizar el comportamiento de filamentos de FtsZ en geometría cilíndrica para intentar reproducir las condiciones que se dan en bacterias *in vivo*. Al aplicar los parámetros obtenidos en dos dimensiones a filamentos de FtsZ en dicha geometría se favorece la formación de espirales enrolladas sobre la superficie del cilindro en lugar de un anillo-Z perpendicular al eje del cilindro. No obstante existen diversos mecanismos

por los que es posible modificar este comportamiento y hacer posible la formación de estructuras con forma de anillo. Nosotros hemos aplicado uno de esos mecanismos, en concreto hemos eliminado en las simulaciones la curvatura espontánea de los filamentos sobre plano. De esta forma se consigue iniciar el mecanismo de crecimiento de filamentos que terminan formando un anillo alrededor del cilindro. En este caso, a diferencia de las estructuras en espiral que aparecen en dos dimensiones, el radio del anillo está determinado por el cilindro en lugar de ser el resultado del balance entre la atracción lateral y la energía elástica de bending. La atracción lateral da lugar a la generación de una fuerza de constricción radial sobre la superficie del cilindro. Usando los parámetros que habíamos estimado previamente y los datos de las simulaciones hemos estimado dicha fuerza, $f_r \approx 4pN$, independientemente del radio del cilindro y, para filamentos largos, de la longitud del filamento. La fuerza es pequeña pero podría constituir por lo menos parte de la fuerza necesaria para el proceso de constricción de la membrana. Además, el papel biológico de la atracción lateral entre filamentos no está limitado a la generación de esta fuerza ya que juega un papel esencial en la formación inicial del anillo-Z. El análisis de las formas que adoptan los filamentos sobre una superficie cilíndrica, teniendo en cuenta sus propiedades mecánicas, muestra que, sin efectos de condensación, las formas helicoidales en lugar de anillos alrededor del cilindro son las estructuras predominantes [40].

En la segunda parte de esta Tesis hemos investigado el efecto de una fuerza radial constrictora sobre la membrana bacteriana interna [56]. La descripción de la membrana en términos del Hamiltoniano de Helfrich incluye tres contribuciones energéticas: el trabajo de volumen, asociado a una diferencia en la presión osmótica entre el citoplasma y el medio externo, un coste por aumentar el área de la membrana, asociado a su tensión superficial, y un coste de "bending" si la curvatura de la membrana se aleja de su curvatura espontánea. Además hemos incluido el anillo de fuerza en forma de una tensión de línea en el lugar de la constricción. Hasta el momento no hay información experimental detallada sobre el proceso de división *in vivo*, pero experimentos recientes mostraron la invaginación *in vitro* de un liposoma tubular provocada por un anillo-Z directamente anclado a la membrana. Hemos comenzado nuestro análisis con este sistema simplificado de un liposoma tubular, libre y abierto, en el que las deformaciones no están limitadas por una pared rígida y no hay diferencia en la presión osmótica. Hemos calculado la forma de la deformación causada por un anillo individual y por una serie de anillos distribuidos de manera periódica a lo largo del tubo y hemos encontrado que están en buen acuerdo con las deformaciones observadas experimentalmente. La estimación de la fuerza de constricción muestra que está en el rango de fuerzas típicamente generadas por motores biomecánicos. Para un análisis más detallado sería de gran utilidad una caracterización más exacta del liposoma y de la forma de las deformaciones.

In vivo, la membrana, igual que sus deformaciones, está limitada por una pared rígida. Para diferencias grandes en la presión osmótica la extensión de la deformación está limitada a una región estrecha alrededor del anillo de fuerza y las fuerzas requeridas superan en órdenes de magnitud a las fuerzas típicamente generadas por motores biomoleculares. Hasta ahora se sabe poco sobre cómo las bacterias regulan y mantienen su diferencia en la presión osmótica entre el citoplasma y el medio externo durante el crecimiento de la célula y su división. Esto, unido

a una mejor comprensión del papel de las capas celulares exteriores, resulta fundamental para entender de forma detallada el proceso de división celular bacteriana.

En esta Tesis hemos desarrollado diferentes modelos teóricos para la descripción de procesos biológicos involucrados en la división celular bacteriana. Todos los modelos están basados en observaciones experimentales y han evolucionado a lo largo del trabajo de Tesis en paralelo con los experimentos.

Bibliography

[1] E. Callaway. Bacteria's new bones. *Nature*, 451:124–126, 2008.

[2] J. Löwe and L.A. Amos. Crystal structure of the bacterial cell-division protein ftsz. *Nature*, 391:203, 1998.

[3] H.P. Erickson. Modeling the physics of FtsZ assembly and force generation. *PNAS*, 106(23):9238, 2009.

[4] S. Rueda, M. Vicente, and J. Mingorance. Concentration and assembly of the division ring proteins ftsz, ftsa, and zipa during the escherichia coli cell cycle. *J. Bacteriol.*, 185(11):3344, 2003.

[5] W. Adams and J. Errington. Bacterial cell division: assembly, maintenance and disassembly of the z ring. *Nat. Rev. Microbiol.*, 7:642, 2009.

[6] C. Lu, J. Stricker, and H.P. Erickson. FtsZ from escherichia coli, azotobacter vinelandii and thermotoga maritima, quantitation, GTP hydrolysis and assembly. *Cell Motil. Cytoskeleton*, 40(1):71, 1998.

[7] A. Feucht, I. Lucet, M.D. Yudkin, and J. Errington. Cytological and biochemical characterization of the FtsA cell division protein of bacillus subtilis. *Mol. Microbiol.*, 40(1):115, 2001.

[8] Y. Chen and H.P. Erickson. Rapid in vitro assembly dynamics and subunit turnover of FtsZ demonstrated by fluorescence resonance energy transfer. *J. Biol. Chem.*, 280(23):22549, 2005.

[9] L. Romberg, M. Simon, and H.P. Erickson. Polymerization of FtsZ, a bacterial homolog of tubulin: is assembly cooperative? *J. Biol. Chem.*, 276(15):11743, 2001.

[10] D.E. Anderson, F.J. Gueiros-Filho, and H.P. Erickson. Assembly dynamics of FtsZ rings in bacillus subtilis and escherichia coli and effects of FtsZ-regulating proteins. *J. Bacteriol.*, 186(17):5775, 2004.

[11] J. Stricker, P. Maddox, E.D. Salmon, and H.P. Erickson. Rapid assembly dynamics of the Escherichia coli FtsZ-ring demonstrated by fluorescence recovery after photobleaching. *PNAS*, 99(5):3171, 2002.

[12] H.P. Erickson, D.W. Taylor, K.A. Taylor, and D. Bramhill. Bacterial cell division protein FtsZ assembles into protofilament sheets and minirings, structural homologs of tubulin polymers. *PNAS*, 93(1):519, 1996.

[13] C. Lu, M. Reedy, and H.P. Erickson. Straight and curved conformations of FtsZ are regulated by GTP hydrolysis. *J. Bacteriol.*, 182(1):164, 2000.

[14] M. Osawa, D.E. Anderson, and H.P. Erickson. Reconstitution of contractile FtsZ rings in liposomes. *Science*, 320(5877):792, 2008.

[15] R.L. Lock and E.J. Harry. Cell-division inhibitors: new insights for future antibiotics. *Nat. Rev. Drug Discovery*, 7:324, 2008.

[16] A. Desai and T.J. Mitchinson. Microtubule polymerization dynamics. *Annu. Rev. Cell Dev. Biol.*, 13:83, 1997.

[17] H.P. Erickson and E.T. O'Brien. Microtubule dynamic instability and gtp hydrolysis. *Annu. Rev. Biophys. Biomol. Struct.*

[18] F.J. Ndelec, T. Surrey, A.C. Maggs, and S. Leibler. Self-organization of microtubules and motors. *Nature (London)*, 389:305, 1997.

[19] M. Dogterom and S. Leibler. Physical aspects of the growth and regulation of microtubule structures. *Phys. Rev. Lett.*, 70:1347, 1993.

[20] H. Flyvbjerg, T.E. Holy, and S. Leibler. Stochastic dynamics of microtubules: a model for caps and catastrophes. *Phys. Rev. Lett.*, 73:2372, 1994.

[21] D. Bramhill and C.M. Thompson. GTP-dependent polymerization of Escherichia coli FtsZ protein to form tubules. *PNAS*, 91(13):5813, 1994.

[22] M.A. Oliva, S. Huecas, J.M. Palacios, J. Martín-Benito, J.M. Valpuesta, and J.M. Andreu. Assembly of archaeal cell division protein FtsZ and a GTPase-inactive mutant into double-stranded filaments. *J. Biol. Chem.*, 278(35):33562, 2003.

[23] J. Mingorance, M. Tadros, M. Vicente, J.M. González, G. Rivas, and M. Vélez. Visualization of single Escherichia coli FtsZ filament dynamics with atomic force microscopy. *J. Biol. Chem.*, 280(21):20909, 2005.

[24] J.M. González, M. Jiménez, J. Mingorance M. Vélez, J.M. Andreu, M. Vicente, and G. Rivas. Essential cell division protein ftsz assembles into one monomer-thick ribbons under conditions resembling the crowded intracellular environment. *J. Biol. Chem.*, 278:37664, 2003.

[25] S. Huecas and J.M. Andreu. Energetics of the cooperative assembly of cell division protein ftsz and the nucleotide hydrolysis switch. *J. Biol. Chem.*, 278:46146, 2003.

[26] F. Gittes, B. Mickey, J. Nettleton, and J. Howard. Flexural rigidity of microtubules and actin filaments measured from thermal fluctuations in shape. *J. Cell Biol.*, 120:923, 1993.

[27] P. Venier, A.C. Maggs, M.F. Carlier, and D. Pantolini. Analysis of microtubule rigidity using hydrodynamic flow and thermal fluctuations. *J. Biol. Chem.*, 269:13353, 1994.

[28] A. Ott, M. Magnasco, A. Simon, and A. Libchaber. Measurement of the persistence length of polymerized actin using fluorescence microscopy. *Phys. Rev. E*, 48:R1642, 1993.

[29] L. Hamon, D. Panda, P. Savarin, V. Joshi, J. Bernhard, E. Mucher, A. Mechulam, P.A. Curmi, and D. Pastr. Mica surface promotes the assembly of cytoskeletal proteins. *Langmuir*, 25:3331, 2009.

[30] P. Mateos-Gil, A. Paez, I. Hörger, P. Tarazona, J. Mingorance, G. Rivas, and M. Vélez. Escherichia coli single ftsz dynamic rings: growing, cyclization, opening, reannealing and depolimerization. *Biophys. J.*, 98:556a, 2010.

[31] R.D. Chaudhuri and J.T. Park. A point mutation converts Escherichia coli FtsZ septation GTPase to an ATPase. *J. Biol. Chem.*, 269(37):22941, 1994.

[32] P.L. Freddolino, A.S. Arkhipov, S.B. Larson, A. McPherson, and K. Schulten. Molcular dynamics simulations of the complete satellite tobacco mosaic virus. *Structure*, 14:437, 2006.

[33] U.M.B. Marconi and P. Tarazona. Nonequilibrium inertial dynamics of colloidal systems. *J. Chem. Phys.*, 124:164901, 2006.

[34] I. Hörger, E. Velasco, J. Mingorance, G. Rivas, P. Tarazona, and M. Vélez. Langevin computer simulations of bacterial protein filaments and the force-generating mechansim during cell division. *Phys. Rev. E*, 77:011902, 2008.

[35] B. Mickey and J. Howard. Rigidity of microtubules is increased by stabilizing agents. *J. Cell Biol.*, 130:909, 1995.

[36] R. Yasuda, H. Miyata, and K. Kinosita. Direct measurement of the torsional rigidity of single actin filaments. *J. Mol. Biol.*, 263:227, 1996.

[37] B. Ghosh and A. Sain. Origin of contractile force during cell division of bacteria. *Phys. Rev. Lett.*, 101(17):178101, 2008.

[38] J.F. Allrad and E.N. Cytrynbaum. Force generation by a dynamic z-ring in escherichia coli cell division. *PNAS*, 106:145–150, 2009.

[39] Z. Li, M.J. Trimble, Y.V. Brun, and G.J. Jensen. The structure of ftsz filaments in vivo suggests a force-generating role in cell division. *EMBO J.*, 26:4694, 2007.

[40] S.S. Andrews and A.P. Arkin. A mechanical explanation for cytoskeletal rings and helices in bacteria. *Biophys. J.*, 93(6):1872, 2007.

[41] I. Hörger, E. Velasco, G. Rivas, M. Vélez, and P. Tarazona. Ftsz bacterial cytoskeletal polymers on curved surfaces: the importance of lateral interactions. *Biophys. J.*, 94:L81, 2008.

[42] W. Margolin. Ftsz and the division of prokaryotic cells and organelles. *Nat. Rev. Mol. Cell Biol.*, 6:862, 2005.

[43] A. Paez, P. Tarazona, P. Mateos-Gil, and M. Vélez. Self-organization of curved living polymers: Ftsz protein filaments. *Soft Matter*, 5:2625, 2009.

[44] A. Paez, P. Mateos-Gil, I. Hörger, J. Mingorance, M. Vicente G. Rivas, M. Vélez, and P. Tarazona. Simple modeling of ftsz polymers on flat and curved surfaces: correlation with experimental in vitro observations. *PMC Biophys.*, 2(1):8, 2009.

[45] C.A. Hale, A.C. Rhee, and P.A.J. de Boer. ZipA-induced bundling of FtsZ polymers mediated by an interaction between C-terminal domains. *J. Bacteriol.*, 182(18):5153.

[46] H.H. Low, M.C. Moncrieffe, and J. Löwe. The crystal structure of zapa and its modulation of ftsz polymerisation. *J. Mol. Biol.*, 341(3):839, 2004.

[47] P. Navajas, G. Rivas, J. Mingorance, P. Mateos-Gil, I. Hörger, E. Velasco, P. Tarazona, and M. Vélez. In vitro reconstitution of the initial stages of the bacterial cell division machinery. *Journal of Biological Physics*, 34:237–247, 2008.

[48] A. Dajkovic, G. Lan, S.X. Sun, D. Wirtz, and J. Lutkenhaus. Minc spatially controls bacterial cytokinesis by antagonizing the scaffolding function of ftsz. *Curr. Biol.*, 18:235, 2008.

[49] S. Thanedar and W. Margolin. Ftsz ehibits rapid movement and oscillation waves in helix-like patterns in escherichia coli. *Curr. Biol.*, 14:1167, 2004.

[50] K.A. Michie, L.G. Monahan, P.L. Beech, and E.J. Harry. Trapping of a spiral-like intermediate of the bacterial cytokinetic protein ftsz. *J. Bacteriol.*, 188:1680, 2006.

[51] K. Kinbara and T. Aida. Toward intelligent molecular machines: directed motions of biological and artificial molecules and assemblies. *Chem. Rev.*, 105.

[52] G. Lan, B.R. Daniels, T.M. Dobrowsky, D. Wirtz, and S.X. Sun. Condensation of ftsz filaments can drive bacterial cell division. *PNAS*, 106:121–126, 2009.

[53] G. Lan, A. Dajkovic, D. Wirtz, and S.X. Sun. Polymerization and bundling kinetics of ftsz filaments.

[54] Ch. Lu, J. Stricker, and H.P. Erickson. Site-specific mutations of ftsz - effects on gtpase and in vitro assembly. *BMC Microbiol.*, 1:1471, 2001.

[55] W. Helfrich. Elastic properties of lipid bilayers: theory and possible experiments. *Z. Naturforsch.*, 28:693, 1973.

[56] I. Hörger, F. Campelo, A. Hernández-Machado, and P. Tarazona. Constricting force of filamentary protein rings evaluated from experimental results. *Phys. Rev. E*, 81:031922, 2010.